SAPIENZA
UNIVERSITÀ DI ROMA

Photonic high dimensional systems and their applications in fundamental quantum mechanics, quantum information and quantum communication

Scuola di Dottorato in Scienze Astronomiche,
Chimiche, Fisiche e Matematiche “Vito Volterra”

Dottorato di Ricerca in Fisica – XXVI Ciclo

Candidate

Vincenzo D’Ambrosio
ID number 1386625

Thesis Advisor

Dr. Fabio Sciarrino

A thesis submitted in partial fulfillment of the requirements
for the degree of Doctor of Philosophy in Physics

December 2013

Thesis defended on 3 February 2014
in front of a Board of Examiners composed by:

Vincenzo D'Ambrosio. *Photonic high dimensional systems and their applications in fundamental quantum mechanics, quantum information and quantum communication.*
Ph.D. thesis. Sapienza – University of Rome

VERSION: December 2013
EMAIL ADDRESS: dambrosiovincenzo@gmail.com

Contents

Introduction

The qubit, the basic unit of quantum information, is a two level quantum system [155] which plays a central role in several field from fundamental quantum mechanics to quantum communication. In general, qubits are experimentally implemented by exploiting different physical systems like atoms, semiconductor quantum dots or photons. Each one of these systems is characterized by some useful properties and some drawbacks. For instance energy levels in a trapped atom are an optimal system for qubits storing [192] but they are not suitable for the communication between different partners. On the other hand photons are difficult to store but they provide a natural system for quantum communication where they are known as "flying qubits" due to their speed and their resilience to decoherence. Another good reason to choose photons for information encoding is that they are easy to produce, manipulate and detect with standard quantum optics techniques. Photonic qubits are usually encoded by exploiting the polarization degree of freedom of photons. These qubits are easily encoded, manipulated and decoded by using standard optical devices like birefringent waveplates and polarizers which give a complete control on the polarization bidimensional space.

In the last decades many efforts have been spent in the investigation of the multidimensional extension of the qubit, quantum d-dimensional systems known as qudits. Such a resource has opened new perspectives in many fields, from fundamental quantum mechanics [114, 202, 68, 120] to quantum cryptography [58, 50] and quantum computation [86, 126]. To give some examples, high dimensional quantum systems assure higher security in quantum key distribution protocols [58], higher information density coding due to a larger alphabet [147], stronger violations in Bell-like tests[114, 63]. Moreover, only Hilbert spaces with dimension $d > 2$ allow to study fundamental quantum correlations known as contextual correlations [120, 68].

In order to enlarge the dimension of the system two approaches are possible. One way is to exploit states of N photons and encode a multiqubit state in a 2^N dimensional Hilbert space. However the experimental preparation of states with large N is extremely challenging, and to date only states with $N = 3$, $N = 4$, and $N = 5$ have been experimentally realized [146, 204, 153, 3]. Moreover, as N grows, N-photon entangled states become increasingly sensitive to losses, as the loss of a single photon is enough to destroy all the phase information [76].

An alternative route is to encode qudits in single photon states.

Being defined in a two dimensional space, polarization is not suitable for this task, however, in order to realize multidimensional quantum systems, it is possible to exploit other degrees of freedom of single photons such as path or orbital angular momentum (OAM). This last degree of freedom is related to the photon's transverse-mode spatial structure [5] and has been recognized as a new promising resource, allowing the implementation of a qudit encoded in a single photon [147, 87]. Related to its higher dimensionality, the OAM

can provide an elevated degree of security and higher information-density coding, with a major channel capacity in the field of quantum communication [44, 88]. Furthermore, it can be exploited in quantum imaging, free-space communication and other fields distant from quantum physics like micromechanics, astronomy and biophysics [87, 199]. A qudit can be encoded in a d-dimensional orbital angular momentum subspace alone, or, as alternative approach, it is possible to employ OAM in combination with polarization or path. Such approach is known as *Hybrid encoding*.

The goal of this thesis has been the experimental investigation of the properties of single photon qudits encoded in orbital angular momentum and polarization as well as their applications in fundamental quantum mechanics, quantum information and quantum communication.

One of the first goals of this research has been the development of a novel device (a transferrer) for the manipulation of hybrid ququarts encoded by exploiting polarization and OAM of single photons [69]. Indeed, although it has been proposed as a new degree of freedom more than twenty years ago [5], the orbital angular momentum of light is still lacking of a complete set of tools which allows to manipulate and detect it as simply as it is done with polarization.

This transferrer has been then exploited as a measurement device of hybrid ququarts in two different experiments on fundamental quantum mechanics focused on the study of contextual correlations in four dimensional systems. In the first experiment we realized a task in which quantum mechanics gives an advantage respect to classical mechanics and there exist no post quantum theory which can do it better [149]. The second experiment has been realized in collaboration with the quantum optics group of Stockholm University and reports the first experimental implementation of a Kochen-Specker set of quantum tests[68]. Kochen-Specker sets are a keystone in fundamental quantum mechanics.

Concerning application of qudits in quantum communication, we identified a bidimensional subspace of hybrid ququart space whose states are invariant under rotations along the propagation axis [70]. This property allows to overcome the alignment problem between reference frames of distant users and could find application in satellite based quantum communication.

Starting from the rotational invariant qubits working principle we then identified a class of hybrid ququart subspaces which, giving rise to a "super resolved" Malus law, greatly enhance the precision in roll angles measurements and can find applications in metrology [71].

High dimensional quantum systems are also a resource in quantum cryptography. In [50] we analyzed the extra security provided by ququarts against a class of possible attacks to a BB84-like protocol and proposed a possible experimental realization based on hybrid ququarts.

Finally, we exploited qudits to experimentally investigate the concept of mutually unbiased bases (MUBs) in dimension $d = 6$ (qusix) which is the lowest dimension for which, the maximal number of MUBs that can be simultaneously defined, is not known yet [67] . Mutually unbiased bases are directly correlated to the concept of complementarity in quantum mechanics and play a crucial role in quantum state tomography and quantum cryptography.

The high fidelity needed for the generation of a good quality set of MUBs has led to develop a novel holographic technique that allow to generate qudits of high dimension with high fidelity in the OAM Hilbert space. Such achievement can be the starting point for further investigations of high dimensional quantum systems.

The thesis is organized as follows:

- Chapter one is divided in two parts. The first one presents some preliminary remarks on fundamental concepts like quantum entanglement and quantum cryptography. The second part is devoted to some of the possibilities opened by the introduction of qudits. In particular how high dimensional systems allow a deeper understanding of quantum theory through quantum contextuality.

- Chapter two focuses on the photonic implementation of qudits by single photon states. In particular some details are given on the orbital angular momentum of light and the most common tools for its manipulation. In the last part of the chapter the quantum transferrer that have been developed in this thesis is described.

- In chapter three we will introduce two particular photon states which can be used to perform alignment-free quantum communication. Although these are qubits, they are obtained as a decoherence free subspace of a four dimensional hybrid space (ququarts). Hence their properties are related to high dimensional Hilbert space and the joint action of polarization and OAM.

- Chapter four focuses on the photonic gear concept. Here a particular subspace of four dimensional hybrid spaces is exploited to perform super-resolved measurement of roll angles.

- Chapter five is dedicated to quantum contextuality, a fundamental property of systems of dimension $d > 3$. Here two experiments are reported: the realization of the simplest task with impossible to beat quantum advantage and the first experimental realization of the famous Kochen-Specker theorem. In the last section of the chapter is also proposed a hybrid ququart implementation of QKD cryptographic protocol in which extra security is provided by contextuality.

- Chapter six deals with six dimensional quantum states and their use for the investigation in the field of mutually unbiased bases.

- A discussion of the results and some considerations on the perspectives of future research on high dimensional quantum systems is reported in the last section of the thesis.

Chapter 1

Fundamental Quantum Mechanics and Quantum Information

A *qubit* is a two-dimensional quantum system (a vector in a two dimensional Hilbert space) which can be defined as:

$$|\phi\rangle = \alpha|0\rangle + \beta|1\rangle \tag{1.1}$$

where α and β are complex numbers, $|\alpha|^2 + |\beta|^2 = 1$ and $|0\rangle$ and $|1\rangle$ are two orthogonal quantum states which consitute the so called *logical basis*. Being the simplest quantum system, the qubit is also a basic tool for quantum mechanics foundations investigations and the constitutive brick of quantum information.

Indeed, being a coherent superposition of $|0\rangle$ and $|1\rangle$, qubits can be seen as the quantum extension of a bit of classical information allowing a new class of tasks which are not possible with classical bits and that constitute the field of quantum information. Two qubits are also the simplest system to show properties like quantum entanglement which puzzled (and still puzzle) scientists for years. Although the fundamental nature of entanglement is still a subject of studies, this quantum property is already exploited as a resource for computational tasks as well as for security in communication.

When we extend the concept of qubit to d-dimensional Hilbert spaces (H) we obtain a *qudit*:

$$|\phi\rangle = \sum_{i=1}^{d} \alpha_i |i\rangle \tag{1.2}$$

where α_i are complex number such that $\sum_{i=1}^{d} |\alpha_i|^2 = 1$ and vectors $|i\rangle$ form an orthonormal basis in H. The introduction of high dimensional Hilbert spaces open new perspectives in every field in which qubit gives contributions. For instance qudits allow the extension of the alphabet for quantum communication, the simplification of quantum logic in quantum computation [126], stronger violations of Bell-like inequalities [114] and the study of contextuality [122], a particular kind of quantum correlation in systems with dimension $d > 3$ which is a fundamental keystone in quantum mechanics.

1.1 Entanglement and non-locality

Entanglement [110] is one of the most famous features of quantum mechanics (QM) and is a central notion for quantum information. Being considered to be the most nonclassical

manifestation of quantum formalism, entanglement was first used in 1935 by Einstein Podolsky and Rosen in their attempt to prove that Copenhagen interpretation of quantum theory is not complete [79]. It was only in 1964 that entanglement evolved from a subject of philosophical debates to a property that could be tested in an experiment thanks to the work of Bell [25] who showed that the probabilities for the outcomes obtained when some entangled quantum state is suitably measured violate the Bell inequality.

To define entanglement, let us consider a multipartite system consisting of n subsystems. According to the quantum formalism, the total Hilbert space is a tensor product of the subsystems spaces:

$$H = \otimes_{i=1}^{n} H_i \tag{1.3}$$

and the total state of the system is in the form:

$$|\psi\rangle = \sum_{i_1,\ldots,i_n} c_{i_1,\ldots,i_n} |i_1\rangle \otimes |i_2\rangle \otimes \cdots |i_n\rangle, \tag{1.4}$$

which cannot in general be described as a product of states of individual subsystems

$$|\psi\rangle \neq |\psi_1\rangle \otimes |\psi_2\rangle \cdots \otimes |\psi_n\rangle, \tag{1.5}$$

If a state can be written as a product state of individual subsystems, it is called *separable state*, otherwise it is an *entangled state*. In the general case when we consider mixed states instead of pure states, it can be proven [208] that a system is entangled if it cannot be written as a convex combination of product states:

$$\rho \neq \sum_i p_i \rho_1^i \otimes \rho_2^i \otimes \cdots \otimes \rho_n^i \tag{1.6}$$

For the sake of simplicity hereafter we will omit the tensor product symbol between states of different subsystems. The simplest example of entangled states is given by the four Bell-states which are defined for bipartite systems of qubits:

$$|\psi^{\pm}\rangle = \tfrac{1}{\sqrt{2}} (|0\rangle|1\rangle \pm |1\rangle|0\rangle) \tag{1.7}$$

$$|\phi^{\pm}\rangle = \tfrac{1}{\sqrt{2}} (|0\rangle|0\rangle \pm |1\rangle|1\rangle) \tag{1.8}$$

and which are a basis in the total four dimensional space. Such states are maximally entangled and unitary operation applied to only one of the two subsystems allows to transform from any Bell state to any other one of the three. Indeed, by defining Pauli operators as:

$$\sigma_x = \begin{pmatrix} 0 & 1 \\ 1 & 0 \end{pmatrix}, \sigma_y = \begin{pmatrix} 0 & -i \\ i & 0 \end{pmatrix}, \sigma_z = \begin{pmatrix} 1 & 0 \\ 0 & -1 \end{pmatrix} \tag{1.9}$$

it is easy to check that, given a Bell state, the other three can be obtained by applying respectively σ_x, σ_y and σ_z to one of the two subsystems.

In the case of two-qudits systems, the general bipartite entangled state is given by:

$$|\psi\rangle = U_A \otimes U_B |\Phi^+\rangle_{AB}, \tag{1.10}$$

where U_A and U_B are unitary transformations and

$$|\Phi^+\rangle_{AB} = \frac{1}{\sqrt{d}} \sum_{i=1}^{d} |i\rangle_A |i\rangle_B \tag{1.11}$$

is the "canonical" maximally entangled state.

The physical consequences of the existence of entanglement are closely related to the concept of locality.

In their though experiment, Einstein Podolsky and Rosen showed that quantum theory leads to a contradiction (due to existence of entanglement) if we accept the following two assumptions:

- *Reality principle: If we can predict with certainty the value of an observable, then this value has physical reality, independtly of our observation.*
- *Locality principle: If two systems are casually disconnected, the result of any measurement performed on one system cannot influence the result of a measurement performed on the second system.*

In particular if we consider a system in the maximally entangled singlet state

$$|\psi^-\rangle = \frac{1}{\sqrt{2}}\left(|0\rangle_A|1\rangle_B \pm |1\rangle_A|0\rangle_B\right) \tag{1.12}$$

where the two subsystems A and B are casually disconnected (i.e. space-like separated), the EPR paradox rises from the fact that, if an observer measures $\sigma_z = +1$ on system A, the system B results to be in the state $|1\rangle$. If instead the observer in A measures $\sigma_x = +1$ the system B results to be in the state $|+\rangle = \frac{1}{\sqrt{2}}(|0\rangle + |1\rangle)$ that is different from state $|1\rangle$. This means that, a measurement performed on system A has an effect on system B, even if they are casually disconnected. This property is in contrast with locality principle and, since such assumption seems more than reasonable, Einstein and co workers concluded that quantum theory was not *complete* which means that there could exist other theories based on quantities (hidden variables) which are not accesible to us and that allow to describe all the experimental results without being in contrast with the two principles reported above. These theories are called "local hidden variables" (LHV) theories. The EPR work was the starting point of a deep philosophical debate, which was brought on a experimentally testable ground only in 1964 with Bell's work.

Bell indeed showed that there are quantum mechanical prediction which can not be described by any theory of local hidden variables [25], hence that there exist experiments based on correlations that allows us to test if nature can be described by hidden variable theories. There exist several versions of Bell inequalities. The most widely used for experimental verification is probably the one due to Claus Horne Shimony and Holt known as CHSH inequality [62].

CHSH inequality derivation

Let us assume that there exist a hidden variable λ such that, for any value of λ, a well defined result $O(\lambda)$ is obtained from the measurement of a physical observable O. The average value for the observables have to be the same that we would obtain in the quantum mechanics framework. Hence the probability distribution $\rho(\lambda)$ must be such that:

$$\langle O\rangle = \int O(\lambda)\rho(\lambda)d\lambda \tag{1.13}$$

Let us define $A(\mathbf{a},\lambda)$ and $B(\mathbf{b},\lambda)$ as the result of the measurements of the (casually disconnected) observables $\sigma_A\cdot\mathbf{a}$ and $\sigma_B\cdot\mathbf{b}$ along the directions $\mathbf{a}$ and $\mathbf{b}$ performed by Alice

and Bob, respectively. As already observed, assuming the locality principle, the outcome of Alice's measurement cannot depend on the outcome of Bob's measurement and vice versa. Therefore, the mean value of the correlations between their polarization measurements is given by:

$$E(\mathbf{a},\mathbf{b}) = \int A(\mathbf{a},\lambda)B(\mathbf{b},\lambda)\rho(\lambda)d\lambda. \tag{1.14}$$

while in the quantum mechanics formalism it is defined as:

$$E(\mathbf{a},\mathbf{b}) = \langle \sigma_A \cdot \mathbf{a} \otimes \sigma_B \cdot \mathbf{b} \rangle \tag{1.15}$$

Let us compute:

$$E(\mathbf{a},\mathbf{b}) - E(\mathbf{a},\mathbf{b}') = \int [A(\mathbf{a},\lambda)B(\mathbf{b},\lambda) - A(\mathbf{a},\lambda)B(\mathbf{b}',\lambda)]\rho(\lambda)d\lambda \tag{1.16}$$

$$= \int A(\mathbf{a},\lambda)B(\mathbf{b},\lambda)[1 \pm A(\mathbf{a}',\lambda)B(\mathbf{b}',\lambda)]\rho(\lambda)d\lambda \tag{1.17}$$

$$- \int A(\mathbf{a},\lambda)B(\mathbf{b}',\lambda)[1 \pm A(\mathbf{a}',\lambda)B(\mathbf{b},\lambda)]\rho(\lambda)d\lambda. \tag{1.18}$$

From the triangular inequality follows that:

$$|E(\mathbf{a},\mathbf{b}) - E(\mathbf{a},\mathbf{b}')| \leq \int [1 \pm A(\mathbf{a}',\lambda)B(\mathbf{b}',\lambda)]\rho(\lambda)d\lambda \tag{1.19}$$

$$+ \int [1 \pm A(\mathbf{a}',\lambda)B(\mathbf{b},\lambda)]\rho(\lambda)d\lambda \tag{1.20}$$

which implies that

$$|E(\mathbf{a},\mathbf{b}) - E(\mathbf{a},\mathbf{b}')| \leq -|E(\mathbf{a}',\mathbf{b}') - E(\mathbf{a}',\mathbf{b})| + 2\int \rho(\lambda)d\lambda. \tag{1.21}$$

since the probability distribution is normalized to one we finally obtain the CHSH inequality:

$$S = |E(\mathbf{a},\mathbf{b}) - E(\mathbf{a},\mathbf{b}')| + |E(\mathbf{a}',\mathbf{b}') + E(\mathbf{a}',\mathbf{b})| \leq 2 \tag{1.22}$$

The main point of this inequality is that exist some observables $(\mathbf{a},\mathbf{a}',\mathbf{b},\mathbf{b}')$ and some states such that quantum mechanics violates the inequality. In the maximum violation conditions, quantum mechanics gives $S = 2\sqrt{2}$ which is known as Cirel'son bound [61]. The most famous experimental violation of Bell inequalities was performed by Aspect and co -workers in 1982 [13]. By exploiting an entangled photon pair in the polarization state $|\psi^-\rangle = 2^{-1/2}(|H\rangle_A|V\rangle_B - |V\rangle_A|H\rangle_B)$ where $|H\rangle$ and $|V\rangle$ are respectively horizontal and vertical linear polarization they violated CHSH inequality by five standard deviations.

After these pioneering works, many efforts have been developed to better understanding the nature of entanglement and in general of quantum correlations. For instance, entanglement is only a necessary and not sufficient condition for a state to be non-local so one can ask which quantum states do not admit LHV model. Indeed, although any entangled pure state violates a Bell inequality, for mixed states it turns out that the relation between entanglement and nonlocality is much more subtle, and in fact not fully understood yet [208][96][43]. Another issue, for istance, is related to the quantification of entanglement itself, a problem that has given rise to several entanglement measures and the concept of entanglement witness [109]. More in general, entanglement is not the only possible kind of quantum correlation, indeed there exist states which are quantum correlated but are also separable, this introduces the concept of *quantum discord*[156].

To conclude this section let us stress that, although the study of entanglement itself (and quantum correlations in general) is still a very active and interesting field (a detailed review can be found in [110] and in [43]), the availability of this resources has opened the way to the development of fields like quantum information and quantum communication.

1.2 Quantum Communication and Quantum Cryptography

Quantum communication (QC) plays a fundamental role in the modern view of quantum physics and opens the possibility of a variety of technological applications. Current implementations of QC use photons as the carriers of qubits. This is due to the fact that photons, known as so-called “flying qubits", are easy to transport from one location to another. In a typical bipartite scenario the emitter and receiver, conventionally called Alice and Bob, chose to encode qubits in the polarization of single photons so that the linear horizontal and vertical polarization states (respectively $|H\rangle$ and $|V\rangle$) correspond to logical basis qubits (respectively $|0\rangle$ and $|1\rangle$). The main advantage of quantum communication respect to classical one is that a qubit could also be a coherent superposition of states $|0\rangle$ and $|1\rangle$, this means that Alice and Bob can freely choose a different basis to encode and measure their qubits and, as a consequence, they can perform secure communication protected by laws of quantum mechanics [97].

In order to communicate in a secret way, two users can indeed exploit quantum cryptography to share a secret key which can be used to encrypt and decrypt the message. Sharing a quantum key is much more convenient than directly sending the message because in this way Alice and Bob can detect an attack during their key distribution and eventually decide to stop the communication before sending any part of the secret message. A very famuos protocol for quantum key distribution is the Bennet-Brassard 84 [29] (BB84). This protocol uses four quantum states that consitute two mutually unbiased bases (see Chapter 6): for instance the logical basis $\{|0\rangle,|1\rangle\}$ and the diagonal one $\{|+\rangle,|-\rangle\}$ where

$$|+\rangle = \frac{1}{\sqrt{2}}\left(|0\rangle + |1\rangle\right), \quad |-\rangle = \frac{1}{\sqrt{2}}\left(|0\rangle - |1\rangle\right) \tag{1.23}$$

In the first step of BB84 protocol Alice sends a qubit to Bob in a polarization state chosen at random among the four states. Next Bob measures the polarization of the incoming photon in one of the two bases chosen at random. At this point they get correlated (uncorrelated) results depending on if they chose the same (different) basis to encode and measure the qubits. Hence Bob obtains a string of bits with 25% of errors, called the “raw key”. In the next step of the protocol Bob announces publicly in which basis he measured every qubit and Alice tells whether or not the state in which she encoded that qubit is compatible with the basis chosen by Bob. If they are compatible they keep the bit, otherwise they disregard it. The new key is called “sifted key”.

This protocol is secure against attacks because, when an eavesdropper (usually called Eve) tries to catch some information performing a measurement on the system she modifies the system itself it and Alice and Bob can notice her eavesdropping. Eve could plan to make a copy of the qubit in order to send one to Bob and store the other one. Unfortunately for her, the “No cloning theorem” [210] assures that perfect copying is impossible in quantum word so she will be only able to keep an imperfect copy for herself. This constitutes the starting point for a series of attacks and corresponding security enhancement strategies which are one of the main topic of quantum cryptography. A complete discussion about

these strategies, although interesting both from fundamental and practical point of view, is out of the topic for this thesis and an extensive review can be found in ref [97]. As a conclusion of this section, let us mention that an ultimate security proof for BB84 protocol has been given in [187] showing that communication is secure if the quantum bit error rate is less than 11% which is known as Shor-Preskill security treshold.

A possible attack to BB84 can be performed if the adversary replaces the quantum system with a classical one for which all the outcomes of measurements can be preassigned [195] (see also Section 5.3). This attack works because, although the BB84 protocol is based on a quantum system (a qubit), there is no way for Alice and Bob to check if their communication is classical or quantum as it would be possible for instance by exploiting entangled particles.

The first protocol based on entanglement was proposed in 1991 by Ekert [80]. In this protocol Alice and Bob share an entangled system in the state $|\psi^-\rangle$. They independently and randomly choose the basis in which measure the qubit among the same four bases of the BB84 protocol. Again they get correlated (uncorrelated) results depending on if they chose the same (different) basis to measure the qubits. The main difference between Ekert91 and BB84 is that in the former Alice and Bob share an EPR state so they can always check the quantumnes (and so the security) of the communication by checking the violation of a Bell inequality. Hence, if Eve tries to substitute the EPR couple with a classical system the two users are immediately aware of her presence.

1.3 Quantum metrology

The precise estimation of a physical quantity is a relevant problem in many research areas. A key aim in metrology is to find new physical methods for enhancing measurement precision. Classical estimation theory asserts that by repeating an experiment N times, the precision of a measurement, defined by the inverse statistical error of its outcome, can be increased at most by a factor of $\sqrt{N}$. In quantum physics, this scaling is known as the standard quantum or shot-noise limit, and it holds for all measurement procedures that do not exploit quantum effects such as entanglement. Remarkably, using certain N-particle entangled states it could be possible to attain a precision that scales as N. This is known as the Heisenberg limit, and is the ultimate bound set by the laws of quantum mechanics [93]. Proof-of-principle demonstrations of these quantum-metrology concepts have been given in recent experiments of optical-phase estimation, magnetic-field sensing and frequency spectroscopy [146, 204, 153, 3, 191, 133, 179, 112]. In photonic approaches, the optimal measurement strategy typically relies on the preparation of “NOON" states [132]

$$|NOON\rangle = \frac{1}{\sqrt{2}}\left(|N\rangle_a|0\rangle_b + |0\rangle_a|N\rangle_b\right) \tag{1.24}$$

in which all N photons propagate in one arm (a) or the other (b) of an interferometer. However, the experimental preparation of NOON states with large N is extremely challenging, and to date only $N = 3$, $N = 4$, and $N = 5$ photonic NOON states have been reported [146, 204, 153, 3]. Moreover, as N grows, N-photon entangled states become increasingly sensitive to losses, as the loss of a single photon is enough to destroy all the phase information [76]. It has been proven that, in the presence of losses or other types of noise, no two-mode quantum state can beat the standard limit by more than just a constant factor in the limit of large N [124, 82, 121, 74]. For these reasons, although quantum metrology bears a great promise for parameters estimation, it is unlikely to become practical in the near future.

1.4 Beyond the qubit: The qudit

Most of the concepts and techniques described in the previous sections, although general, are based on qubit or a couple of qubits. All the non-locality considerations, for instance, have been based on a bipartite scenario of two qubits. The same holds for quantum communication and cryptography. In this paragraph we will see how the increasing of the dimensions of the Hilbert space can be exploited as a resource in fundamental quantum mechanics as well as in quantum information.

1.4.1 Violation of Bell inequalities

Bell inequalities have been violated in numerous experiments however, experimental imperfections open various loopholes that could be in principle exploited by a locally casual model to reproduce the experimental data [43]. In particular one of the main loopholes for experiments involving photons is called "Detection Loophole" since it is due either to losses between the source of particles and the detectors or to the fact that the detectors themselves have non-unit efficiency. As a result we need to consider three outcomes instead of two (+1 , -1, "no-click") for a measurement apparatus used to test Bell inequalities. If the detection efficiency is below a certain threshold it is possible to design a local model which can completely reproduce the observed data. For the CHSH Bell inequality using a two-qubit maximally entangled state it is possible to show that this threshold efficiency is $\eta^* = 82.8\%$ which can be lowered to $\eta^* = 2/3$ by considering partially entangled states [78]. Recently a new kind of superconducting high efficiency detectors has been developed[137, 89] however they need the photon to be coupled to a fiber ending in the detector in a cryostat operating at low temperature, hence the overall photodetection efficiency is still in many cases insufficient for a detection loophole-free Bell test [209, 190]. Only very recently it has been reported a Bell-violation using entangled photons which closes the detection loophole [98]. However in this framework high dimensional systems can be exploited as an alternative resource for closing the detection efficiency loophole. Indeed if we consider entangled ququarts and four (binary) measurements settings, the threshold efficiency results to be as low as $\eta^* = 61.8\%$ while, in an asymmetric scenario (in which we consider atom-photon entanglment) in Bell tests with d measurement settings and d-dimensional systems, an efficiency as low as $1/d$ can be tolerated [202].

It is also possible to show that violations of local realism by two entangled qudits are stronger than the ones obtained with two qubits [114]. We can indeed consider a system in the state:

$$\rho_N(F_N) = F_N \rho_{noise} + (1 - F_N)|\psi^N_{max}\rangle\langle\psi^N_{max}| \tag{1.25}$$

where the positive parameter $F_N \leq 1$ determines the noise fraction within the full state, $\rho_{noise} = \frac{1}{N^2}\mathbb{1}$ and $|\psi^N_{max}\rangle$ is the maximal entangled state 1.11 for a qudit with $d = N$. The threshold maximal F_N^{max} for which the state $\rho_N(F_N)$ still does not allow a local realistic model can be considered as a value of the strength of violation of local realism. In can be shown that the value of F_N^{max} increases with the dimension N of the system. Figure 1.1 reports the numerical calculation of F_N^{max} for qudits with q up to 9 as performed in Ref. [114].

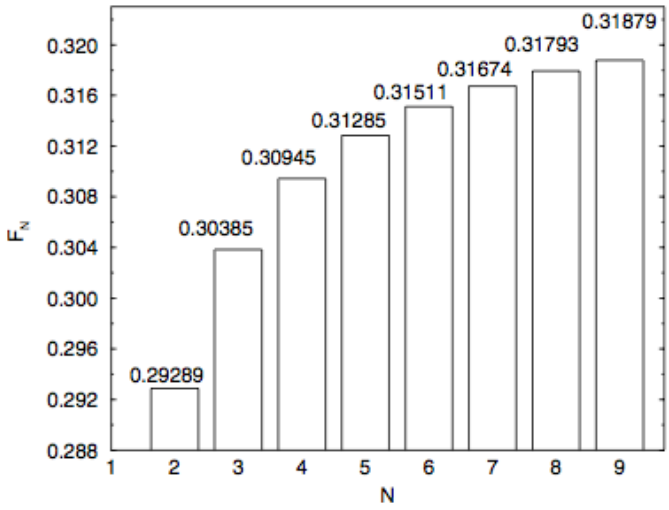

Figure 1.1. Violations of local realism by two entangled qudits are stronger than for two qubits: numerical calculation of F_N^{max} for qudits with d up to 9. [114]

1.4.2 Contextuality

One of the most important features of high dimensional quantum systems in fundamental quantum mechanics is that, for $d \geq 3$, different bases in the Hilbert space may have some vectors in common. Such simple mathematical property has deep physical implications. Indeed, the classical description of nature is based on the assumption that all physical systems possess properties, such as position and velocity, that can be revealed by the act of observation and whose objective existence is independent of whether or not the observation does actually take place. A consequence of this assumption is that there should exist a joint probability distribution for the results of any set of joint measurements revealing these properties [84]. However, for $d \geq 3$ there is a fundamental theorem (Kochen and Specker (KS) theorem [122]) that states that, if quantum mechanics is correct, then nature cannot be described in classical terms [193, 26, 122]. This theorem highlighs quantum correlations, called contextual correlations, which are more general than non-local correlations considered for the violation of Bell's inequalities. Contextuality arguments are based on the concept of *compatible measurements* and *context* which we will now briefly recall.

Compatible measurements and context

If a matrix A is not degenerate, there is only one basis in which A is diagonal. That basis corresponds to a maximal quantum test which is equivalent to a measurement of the physical observable represented by the matrix A. More precisely, let N be the maximum number of different outcomes obtainable in a test of a given quantum system; then, any test that has exactly N different outcomes is called *maximal* [165]. If, on the other hand, A is degenerate, there are different bases in which A is diagonal. Given a matrix B which commutes with A it is possible to find a basis in which both matrices are diagonal. Such a basis corresponds to a maximal test, which provides a measurement of both A and B. It follows that two commuting operators correspond to *compatible* measurements (i.e they can be measured simultaneously). If, on the other hand, A and B do not commute, there is no basis in which both are diagonal hence the measurements of A and B are mutually incompatible. The

generalization to a larger number of operators is straightforward: A set of commuting operators is called *complete* if there is a single basis in which all these operators are diagonal. Therefore, the simultaneous measurement of a complete set of commuting operators is equivalent to the measurement of a single nondegenerate operator, by means of a maximal - or complete - *quantum test* [165]. In other words, two tests are compatible when, for any preparation, each measurement will always yelds identical results, no matter how many times the tests are performed or in which order.

Let us now assume that A is compatible with B and C. A *non-contextual* theory is one for which the result of a measurement of A does not depend on its *context*, namely on whether we measure A alone or A and B, or A and C. In the next paragraph we show that quantum mechanics cannot be explained by non-contextual hidden variable theories.

KS theorem

KS proved that, for any quantum system of dimension $d \geq 3$, there are sets of yes-no tests (represented in QM by projectors $\Pi_i = |v_i\rangle\langle v_i|$ onto unit vectors $|v_i\rangle$) for which it is impossible to assign results 1 (yes) or 0 (no) in agreement with two predictions of QM:

- (i) If two exclusive tests (represented by orthogonal projectors) are performed on the same system, both cannot give the result 1.

- (ii) If d pairwise exclusive tests (i.e., satisfying $\sum_{i=1}^{d} \Pi_i = \mathbb{1}$) are performed on the same system, then one of the tests gives 1.

For a given d, these sets, called KS sets, are universal in the sense that assigning results is impossible for any quantum state. The existence of KS sets demonstrates quantum contextuality, namely the fact that, for any quantum state, it is impossible to reproduce the predictions of QM with theories in which the measurement results are independent of other compatible measurements. These theories are called non-contextual hidden variable (NCHV) theories. Quantum contextuality, can be experimentally detected though the violation of inequalities satisfied by NCHV models, called noncontextuality inequalities. While violation of Bell inequalities described in section1.1 applies only to a statistical measurement procedure, the paradoxes arising from contextuality arguments results from counterfactual logic, are valid for systems in any quantum state and therefore do not require the system to be prepared in specific quantum states, as is the case for the violation of Bell inequalities. However, as already said, Bell inequalities can be regarded as a restricted form of non contextual inequalities, where compatibility of measurement is replaced by a more stringent requirement of spatial separation [182].

The original KS set had 117 yes-no tests in $d = 3$ [122]. In $d = 3$, the simplest known KS set has 31 tests [165] and it has been proven that a KS set with less than 19 tests does not exist [163, 46, 11]. Indeed, numerical evidence suggests there is no KS set with less than 22 tests in $d = 3$ [163]. However, in $d = 4$, there is a KS set with 18 yes-no tests [53], and it has been proven that there is no KS set with a smaller number of yes-no tests [163, 46]. Moreover, there is numerical evidence that the same holds for any dimension [163], suggesting that, as conjectured by Peres [166], the 18-test KS set is the simplest one in any dimension. In the next section a demonstration of such 18-test KS set is given.

1000	1111	1111	1000	1001	1001	111-1	111-1	100-1
0100	11-1-1	1-11-1	0010	0100	1-11-1	1-100	0101	0110
0011	1-100	10-10	0101	0010	11-1-1	0011	10-10	11-11
001-1	001-1	010-1	010-1	100-1	0110	11-11	1-111	1-111

Figure 1.2. KS demonstration: The projectors in Table1.1 can be arranged in 9 different bases (columns). For any NCHV theory, in each column there is only one "yes" answer so the total number of "yes" is an odd number. The contradiction comes from the fact that every projectors appears two times in the table (different colors indicate different projectors) hence the total number of "yes" has to be an even number.

KS set - a proof with 18 tests

Let us consider the set of 18 projectors over ququarts represented in Table 1.1. There, each vector represents the projection operator onto the corresponding normalized state. The states of table 1.1 can be arranged in 9 sets of four mutually orthogonal vectors so that the corresponding projectors sum the identity (see fig 1.2 where each column groups four mutually orthogonal states). The contradiction follows from the fact that, respect to figure 1.2, for any NCHV theory, each column must have assigned the answer "yes" to one and one only vector. However each vector appears in two columns, so the total number of "yes" answers must be an even number while the number of column is an odd number.

State Projectors	
$(1,0,0,0)$	$(0,0,1,0)$
$(0,1,0,0)$	$(0,1,0,1)$
$(0,0,1,1)$	$(1,0,0,1)$
$(0,0,1,-1)$	$(1,0,0,-1)$
$(1,1,1,1)$	$(1,-1,1,1)$
$(1,1,-1,-1)$	$(1,1,-1,-1)$
$(1,-1,0,0)$	$(0,1,1,0)$
$(1,0,-1,0)$	$(1,1,1,-1)$
$(0,1,0,-1)$	$(1,-1,1,1)$

Table 1.1. A KS of 18 projectors in dimension d=4.

Exclusivity graph of a NC inequality

In order to experimentally test contextuality we need to define some inequalities which hold for NCHV theories but are violated with a quantum system. A useful way to represent NC inequalities is based on the graph representation. Two different graphs can be associated to any given NC inequality: a compatibility graph and an exclusivity graph. In a compatibility graph, each vertex corresponds to a test and adjacent vertices represent compatible tests [51]. Let us consider for example the CHSH inequality in the following form:

$$S = \langle A_0 B_0 \rangle + \langle A_0 B_1 \rangle + \langle A_1 B_0 \rangle - \langle A_1 B_1 \rangle \leq 2 \tag{1.26}$$

where the four observables A_0, A_1, B_0, B_1 can assume the values +1 or -1. All possible pairs of observables are compatible except for the pairs (A_0, A_1) and (B_0, B_1) . The corresponding compatibility graph is represented in Fig1.3 a.

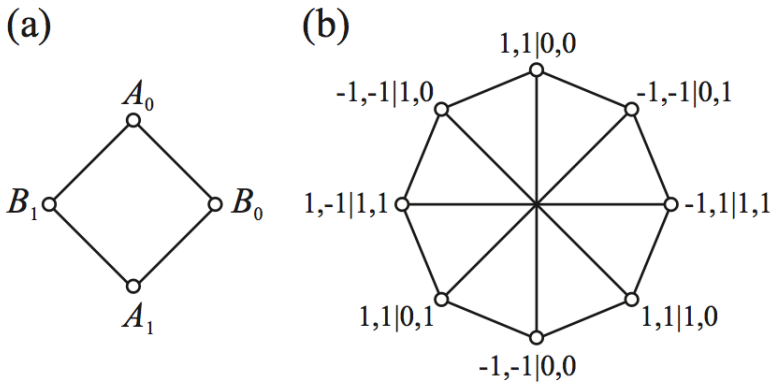

Figure 1.3. (a) The compatibility graph of the CHSH experiment. (b) The exclusivity graph of the CHSH inequality [51]

In order to deduce its exclusivity graph, let us rewrite the CHSH inequality taking into account that:

$$\pm \langle A_i B_j \rangle = 2[P(1, \pm 1|i, j) + P(-1, \mp 1|i, j)] - 1 \tag{1.27}$$

where $P(a, b|i, j)$ is the probability of the event "the result a has been obtained when measuring A_i and the result b has been obtained when measuring B_j". We can then rewrite the inequality as:

$$\begin{aligned} \Sigma = \frac{S}{2} + 2 = P(1,1|0,0) + P(-1,-1|0,0) + P(1,1|0,1) + \\ + P(-1,-1|0,1) + P(1,1|1,0) + P(-1,-1|1,0) \\ + P(1,-1|1,1) + P(-1,1|1,1) \leq 3 \end{aligned} \tag{1.28}$$

where the left-hand side is now a convex sum of probabilities of all the events. In the corresponding exclusivity graph fig1.3 b, each vertex is one of the eight events involved in the inequality while adjacent vertices represent events that cannot occur simultaneously.

The exclusivity graph (G) is a fundamental tool for studying NC inequalities and all the experiments reported in Chapter 5 are designed starting from such kind of graph. Indeed, the most interesting property of an exclusivity graph is that the maximum value of Σ for NCHV theories and for quantum mechanics is exactly given by two numbers related to the graph. For a NCHV theory, the upper bound for Σ is given by the maximum number of pairwise nonadjacent vertices in G, which is known as the independence number of the graph $\alpha(G)$.

$$\Sigma \leq \alpha(G) \qquad \text{(NCHV theories)} \tag{1.29}$$

The upper bound for Σ for quantum mechanics is instead given by a number called Lovász number $\vartheta(G)$[54] which is defined as:

$$\vartheta(G) = \max \sum_{i \in V(G)} |\langle \psi | v_i \rangle|^2, \tag{1.30}$$

where the maximum is taken over all unit vectors $|\psi\rangle$ and $|v_i\rangle$ and all dimensions, where each $|v_i\rangle$ corresponds to a vertex of G, and two vertices are adjacent if and only if the corresponding vectors are orthogonal. Hence for quantum mechanics:

$$\Sigma \leq \vartheta(G) \qquad \text{(QM)} \tag{1.31}$$

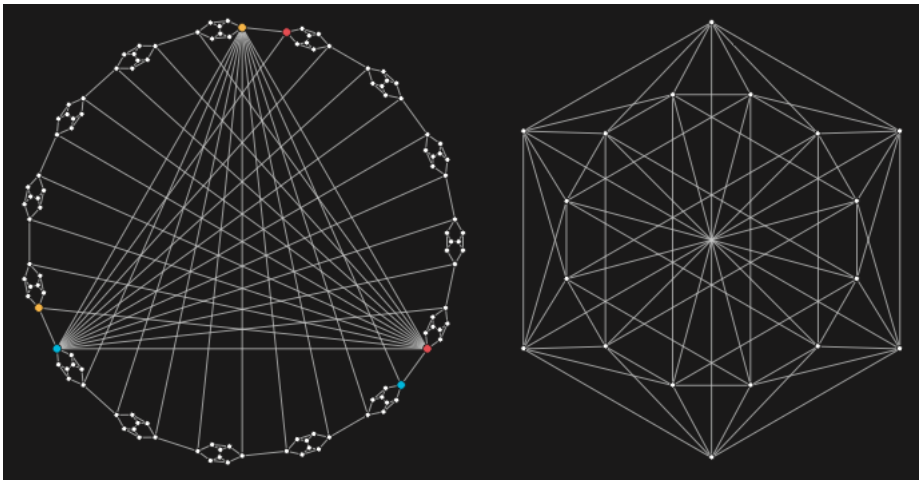

Figure 1.4. Exclusivity graph for the original 117 contextual questions in the Kochen-Specker theorem (left) and the simplest equivalent set with 18 questions in dimension 4 (right). Colours indicate duplicated questions. [178]

By exploiting this formalism, any experiment producing quantum contextual correlations can be associated to an exclusivity graph for which $\alpha(G) < \vartheta(G)$.

Of course an exclusivity graph can be associated also to any KS set [122]. The fundamental feature of KS graphs is that for these sets, the violation of the NC inequality holds for any tested state. Fig. 1.4 shows the graph corresponding to the original 117-test (left) compared to the 18-test KS set (right) which is the simplest possible KS set. This last representation will be analyzed in detail in Chapter 5 together with the report of the first experimental verification of the KS theorem.

Indeed, while Bell inequalities [25] revealing quantum nonlocality have stimulated a large number of experiments (e.g., [13, 198, 207, 181]) and have a number of applications (e.g., [80, 41, 170]), the awareness that quantum contextuality and, specifically, state-independent quantum contextuality can also be observed in actual experiments is relatively recent [47] and a complete KS set of yes-no tests, in the original form defined by KS, has never been experimentally implemented before.

Post quantum theories

We have seen how to represent in a graph form a series of experiments to be performed on a physical system in order to discriminate what kind of correlations are present in the system itself. Since there are graphs for which $\alpha(G) < \vartheta(G)$ we deduce that, if our measurements violates the NC inequality :

$$\alpha(G) < \Sigma \leq \vartheta(G) \tag{1.32}$$

our system shows quantum correlation which cannot be explained by preassigning the value to the outcomes of the tests of the graph.

However in general quantum mechanics does not give the maximum possible value for Σ allowed by laws of probability. Indeed, it is possible to design post-quantum theories in which $\vartheta(G) < \Sigma$. The only requirement defining these post-quantum theories is that they cannot assign a value larger than 1 to the sum of probabilities of mutually exclusive possibilities. In this case the upper bound for Σ is given by $\alpha^*(G)$, the fractional packing

number of G, which is defined as

$$\alpha^*(G) = \max \sum_{i \in V(G)} w_i, \tag{1.33}$$

where $V(G)$ is the set of vertices of G, and the maximum is taken for all $0 \leq w_i \leq 1$ and for all subsets of pairwise adjacent vertices c_j of G, under the restriction $\sum_{i \in c_j} w_i \leq 1$ [55].

Since for any graph:

$$\alpha(G) \leq \vartheta(G) \leq \alpha^*(G) \tag{1.34}$$

the existence of these post quantum theories open a fundamental question on quantum mechanics. Indeed experimental values of Σ are always bounded by the Lovátz number hence there have never been observed post quantum correlations that violate quantum mechanics. Nevertheless the physical principle that prevents quantum mechanics from being more contextual has not been found yet. However, recently an interesting conjecture has tried to explain the existence of quantum correlation by mean of a fundamental principle: the exclusivity principle (E) which states that "the sum of probabilities of pairwise exclusive events cannot exceed 1" [49][212].

It is however possible to find some experiments in which the Lovátz number is equal to the fractional packing number. In this case the quantum advantage is impossible to beat by any post-quantum theory.

Chapter 5 reports the experimental verification of the simplest task with this property.

1.4.3 Quantum Communication and Cryptography

Quantum cryptographic protocols based on complementarity (for instance BB84) are nonsecure against attacks in which complementarity is imitated with classical resources [195]. As we will show in Chapter 5, the Kochen-Specker theorem provides protection against these attacks, without requiring entanglement or spatially separated composite systems.

Qudits are a resource also for secure quantum communication, indeed new quantum key distribution protocols have been conceived in which a larger error rate can be tolerated while preserving security [58, 57]. Moreover a different protocol extending Ekert91 [80] by using entangled qutrits has been experimentally realized [103].

As a last remark let us stress that usually, all the free space communication protocols are based on photon polarization. It is implicitly assumed that the reference frames of Alice and Bob are perfectly aligned, i.e. when Alice sends a polarization state $|H\rangle$ Bob has 100% of probability of measure $|H\rangle$. This is not taking into account experimental imperfections and the fact that Alice and Bob can be in a situation in which their relative orientation is completely unknown. Even here, high dimensional systems can be exploited as a resource. Indeed in Chapter 3 we present a method that, based on qudits in dimension four, allows to perform quantum communication in alignment-free settings.

Chapter 2

Qudits and Photonics

In the previous chapter we have seen how high dimensional systems can find applications in fundamental quantum mechanics and in quantum information. Here we will describe a convenient physical system to implement qudits in order to perform experiments. Among the systems usually exploited to encode information, photons are with no doubt a very convenient choice as information carriers. Indeed photons are easy to transmit, to generate, to manipulate and to detect with technologies which are available today in many quantum optics labs. As we have seen in Chapter 1, in a typical quantum communication scenario, Alice and Bob exploit photon polarization in order to encode their qubits. This is a natural choice since polarization qubits are easily written, manipulated and decoded by using standard optical elements like birefringent waveplates and polarizing beam splitters.

However, if we want to encode a qudit in a photon, polarization is not enough anymore. We could decide to exploit more photons (like for instance in a NOON state) but this approach presents some drawbacks related to demanding experimental resources and extreme sensitivity to photon losses. Fortunately a single photon presents, apart polarization, several degrees of freedom (DOF) that are suitable for information encoding like path or orbital angular momentum (OAM) that are both defined in an infinite dimensional Hilbert space. Hence it is possible in principle to encode a qudit of arbitrary dimension in a single photon state avoiding all the problems of multiparticle states encoding. It is also possible to exploit two DOF at the same time, in this case we will refer to *hybrid encoding*. This last encoding presents some advantages that will be described in the following chapters.

In this thesis we will focus mainly on orbital angular momentum of light as a degree of freedom for information encoding, alone or in combination with polarization. OAM is related to the spatial modes of the electromagnetic field [1] and allows to manipulate qudits without the need of cascade interferometers which are a fundamental tool when we work with qudits encoded in path. The study of properties of optical orbital angular momentum is relatively a new field since the sistematic study of this degree of freedom has started only in the early 90s after a seminar paper by Allen and co workers [5]. Starting from this paper the OAM of light has attracted more and more attention not only in the quantum information community [147, 139, 4] but also for instance in microscopy [90, 30], optical tweezing [160], biophysics [102] and astronomy[197]. Despite this success, there is still a lack of a complete and efficient instrumentation for orbital angular momentum manipulation which would make this DOF as easy to manipulate as polarization. One of the goals of this thesis has been the development of a new tool for OAM manipulation that will be presented

[1] There are also other ways to encode information in spatial modes like for instance in [85, 154, 159, 1]

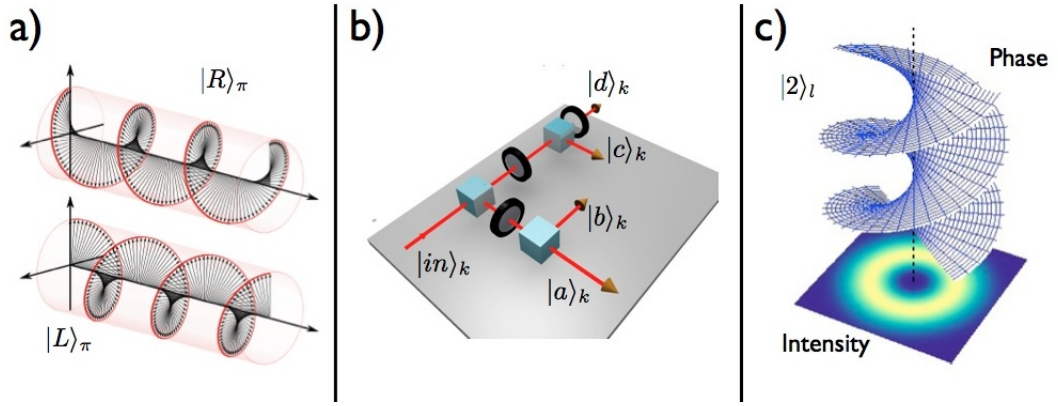

Figure 2.1. In order to encode quantum information it is possible to exploit several degrees of freedom of a single photon like polarization (a), path (b) and orbital angular momentum (c)

in section 2.14 and which has been a fundamental resource in some of the experiments presented in the following chapters.

2.1 Polarization and path encoding

A polarization qubit can be defined as:

$$|\phi\rangle = \alpha|0\rangle + \beta|1\rangle = \alpha|H\rangle_\pi + \beta|V\rangle_\pi \tag{2.1}$$

where $|H\rangle_\pi$ and $|V\rangle_\pi$ are the linear horizontal and vertical polarization states and correspond to the logical basis states $|0\rangle$ and $|1\rangle$ respectively. Qubits $\{|+\rangle, |-\rangle\}$ that are needed for the BB84 protocol are immediately obtained as superposition of $|H\rangle_\pi$ and $|V\rangle_\pi$ and correspond to diagonal and antidiagonal linear polarizations:

$$|+\rangle = |A\rangle_\pi = \frac{1}{\sqrt{2}}(|H\rangle_\pi + |V\rangle_\pi) \tag{2.2}$$

$$|-\rangle = |D\rangle_\pi = \frac{1}{\sqrt{2}}(|H\rangle_\pi - |V\rangle_\pi) \tag{2.3}$$

These two sets of states, togheter with circular polarization states:

$$|L\rangle_\pi = \frac{1}{\sqrt{2}}(|H\rangle_\pi + i|V\rangle_\pi) \tag{2.4}$$

$$|R\rangle_\pi = \frac{1}{\sqrt{2}}(|H\rangle_\pi - i|V\rangle_\pi) \tag{2.5}$$

constitute a maximal set of mutually unbiased bases (see Chapter 6) in polarization space and are easily generated, manipulated and detected by exploiting standard optical devices like polarizers and birefringent waveplates (in particular half waveplate (HWP) and quarter waveplate (QWP)). In fig 2.1a are depicted the electric field vectors at a given time for circular polarized light beams.

A path qubit is usually defined as:

$$|\phi\rangle = \alpha|0\rangle + \beta|1\rangle = \alpha|a\rangle_k + \beta|b\rangle_k \tag{2.6}$$

where $|a\rangle_k$ and $|b\rangle_k$ indicate two separate possible paths for the photon propagation. Such a state can be immediately generalized to higher dimensions as:

$$|\phi\rangle = \sum_{i=1}^{d} \alpha_i |a_i\rangle_k \tag{2.7}$$

which can be experimentally obtained by dividing the paths via beam splitters (BS) and adding suitable phase shifters in each path (Fig. 2.1 b).

The experimental fundamental link between polarization and path is given by a device called polarizing beam splitter (PBS). A PBS, realizing the following transformation:

$$(\alpha|H\rangle_\pi + \beta|V\rangle_\pi)\,|a\rangle_k \longrightarrow \alpha|H\rangle_\pi|a\rangle_k + \beta|V\rangle_\pi|b\rangle_k \tag{2.8}$$

allows to switch from a polarization qubit to one defined in a hybrid space between polarization and path. Let us notice that the state 2.8 is a single photon entangled state where entanglement is between two different DOF of the same photon. This follows from the fact that a PBS can be seen as a CNOT gate where the control qubit is given by polarization and the target by path. This is just one example of single photon qudit and of an optical device which acts as an interface between two different DOF of the same photon. More examples can be found in the next section where the orbital angular momentum of light is described together with the main tools for its manipulation and its interfacing to polarization and path.

2.2 Orbital Angular Momentum

The existence of mechanical properties of light has been already supposed by Kepler in the XVII century in order to explain the existence of comets' tail. After a couple of centuries Maxwell formulated his beautiful theory which summarizes all properties of electromagnetic field in four famous equations from which it is possible to derive all the classical properties of light, including linear and angular momentum. Angular momentum in particular can be in most cases divided in two distinct contribution. The first one is related to polarization of light and it is called spin angular momentum (SAM). Already in 1909 Poynting anticipated that circularly polarized light should have an angular momentum to energy ratio of σ/ω (where helicity is $\sigma = \pm 1$ for left and right handed polarized light respectively) and that any transformation of polarization state must correspond to an angular momentum exchange with the optical system[175]. Such effect was actually observed by Beth in 1936 [31] in a famous experiment with a birefringent waveplate suspended on a filmament. But SAM is only a part of the total angular momentum of light.

The other contribution is associated with the spatial distribution of the field as first recognized by Darwin in 1932[72]. Such contribution is needed also because higher-order atomic transitions require emitted light to carry multiple units of $\hbar$ angular momentum and hence orbital angular momentum in addition to spin. It was in 1992 that Allen and co workers [5] recognized that all helically phased beams carry an OAM equivalent which is multiple of $\hbar$. This separation of orbital and spin components is complex in the presence of tight focusing, and in such situations one needs to analyze the various components in terms of angular momentum flux[16]. Although a general decomposition of light's angular momentum is still a subject of research [158, 141, 32] in most cases the orbital and spin angular momenta remain distinct quantities and useful concepts with which to analyze many experimental situations. In particular, in paraxial approximation SAM and OAM

contribution are well defined and have been observed separately in several experiments [87, 213]. Paraxial regime is also the natural framework to describe laser beams that have been used in all the experiments here reported, hence hereafter we will always refer to this approximation.

2.2.1 Transverse Modes

A paraxial wave that is propagating along the z axes can be described by a complex amplitude [183]:

$$A(\vec{r}) = u(\vec{r})e^{-jkz} \tag{2.9}$$

For this complex amplitude to satisfy the Helmotz equation

$$\nabla^2 A(\vec{r}) + k^2 A(\vec{r}) = 0 \tag{2.10}$$

the complex envelope $u(\vec{r})$ must satisfy the paraxial Helmotz equation:

$$\nabla_T^2 u(\vec{r}) - j2k\frac{\partial u(\vec{r})}{\partial z} = 0 \tag{2.11}$$

A solution of such equation is the well known Gaussian beam TEM_{00} (transverse electromagnetic) that corresponds to the complex amplitude:

$$u(x,y) = A_0\frac{W_0}{W(z)}exp\left[-\frac{x^2+y^2}{W^2(z)}\right]exp\left[-jkz - jk\frac{x^2+y^2}{2R(z)} + j\zeta(z)\right] \tag{2.12}$$

where the beam parameters are defined as:

$$W(z) = W_0\left[1+\left(\frac{z}{z_0}\right)^2\right]^{1/2} \tag{2.13}$$

$$R(z) = z\left[1+\left(\frac{z}{z_0}\right)^2\right] \tag{2.14}$$

$$\zeta(z) = tan^{-1}\left(\frac{z}{z_0}\right) \tag{2.15}$$

$$W_0 = \left(\frac{\lambda z_0}{\pi}\right)^{1/2} \tag{2.16}$$

and z_0 and λ are respectively the Rayleigh range and the wavelength of the beam. The intensity distribution of this beam has a Gaussian shape and, for a given z depends only on the distance r from the propagation axis:

$$I(r,z) \propto \frac{1}{\pi W^2(z)}exp\left[-\frac{2r^2}{W^2(z)}\right]. \tag{2.17}$$

The phase of the beam is instead:

$$\varphi(r,z) = kz - \zeta(z) + \frac{kr^2}{2R(z)} \tag{2.18}$$

and, on the beam axis ($r = 0$) comprises of two components. The first one, kz is the phase of a plane wave while the second one, $\zeta(z)$, is called *Gouy phase* and represents the excess of delay of the wavefront in comparison to a planewave. The total Gouy phase shift accumulated as the wave travels from $z = -\infty$ to $z = +\infty$ is π. Although the Gaussian beam is the most common laser beam, it is only a particular state of a complete set of solutions of the paraxial equation 2.11.

Hermite-Gauss modes

A well known family of solution for equation 2.11 are the Hermite-Gauss modes HG_{mn} whose analytical form for the amplitude $u_{mn}(x, y, z)$ of the field is given by:

$$u_{m,n}(x, y, z) = A_{m,n}\left[\frac{W_0}{W(z)}\right] G_m\left[\frac{\sqrt{2}x}{W(z)}\right] G_n\left[\frac{\sqrt{2}y}{W(z)}\right] \times exp\left[-jkz - jk\frac{x^2 + y^2}{2R(z)} + j(n + m + 1)\zeta(z)\right] \tag{2.19}$$

where

$$G_n(t) = H_n(t) exp\left(-\frac{t^2}{2}\right) \tag{2.20}$$

is the Hermite-Gaussian function of order n, H_n is a Hermite polynomial and $A_{m,n}$ is a constant. When $m = n = 0$ we obtain the fundamental Gaussian which can also be called HG_{00}. The intensity and phase distribution on the plane $z = 0$ for some HG modes are reported in fig2.2.

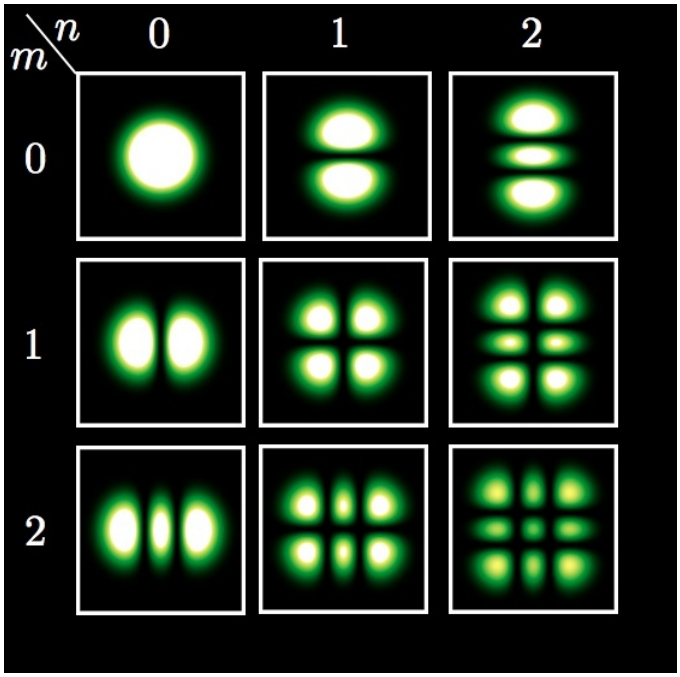

Figure 2.2. Intensity distribution of the lowest HG_{mn} spatial modes

Laguerre-Gauss modes

Another complete set of solution of the paraxial equation is given by the so called Laguerre-Gauss ($LG_{p,l}$) modes that can be obtained solving eq 2.11 by variables separation in cylindrical coordinates (r, φ). The amplitude of LG modes is given by:

$$u_{pl}(r, \varphi) = \frac{C_{p,l}}{(1 + z^2/z_0^2)^{1/2}}\left[\frac{r\sqrt{2}}{W(z)}\right]^{|l|} L_p^l\left[\frac{2r^2}{W^2(z)}\right] exp\left[-\frac{r^2}{W^2(z)}\right] exp\left[-\frac{ikr^2 z}{2(z^2 + z_0^2)}\right] exp\left[i(2p + |l| + 1)\zeta(z)\right] exp(il\varphi) \tag{2.21}$$

where $C_{p,l}$ is a constant and $L_p^l(t)$ is the generalized Laguerre polynomials, the radial index p is not negative and the azimuthal index $l \in Z$. The intensity profile of LG beams is characterized by a null intensity in the center when $l \neq 0$ due to a phase singularity in $r = 0$ given by to the term $e^{il\varphi}$. The parameter p indicates the number of nodes for the electromagnetic field along the radial direction. For $p = 0$ the intensity profile is also called "doughnut" mode (see fig2.3). Since both HG and LG modes are a complete set of solutions

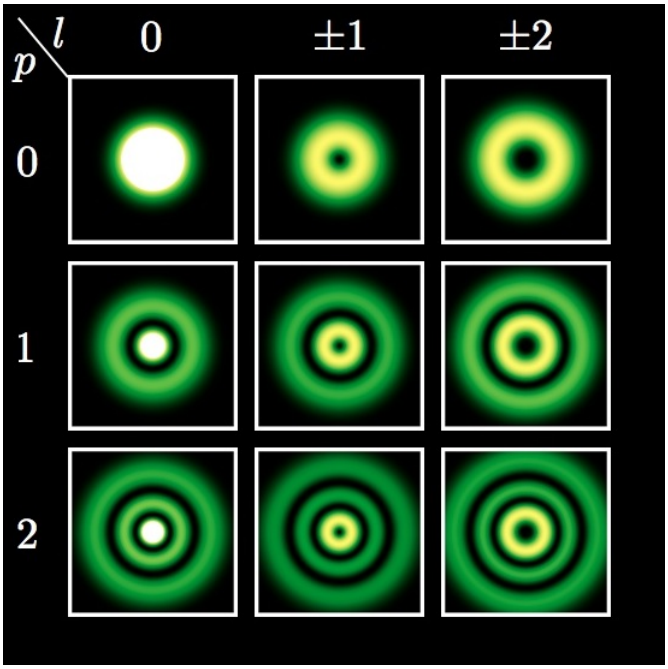

Figure 2.3. Intensity distribution of the lowest LG_{pl} spatial modes

for the Helmotz paraxial equation, an LG mode can always be written as a superposition of HG modes and vice versa. This property is exploited in the cylindrical lens mode converter that will be described in the next section.

OAM eigenstates

LG modes have been recognized as eigenstates of orbital angular momentum for the first time in the paper [5] where is shown that an $LG_{p,l}$ beam carries $l\hbar$ units of orbital angular momentum per photon. More in detail Allen and co-workers considered the angular momentum to energy ratio for a linear polarized LG beam of frequency ω and obtained for this ratio a value of l/ω while, by performing the same calculation for a circular polarized LG beam with helicity σ they obtained $(l + \sigma)/\omega$. Such description is consistent with the quantum picture in which each photon carries $l\hbar$ of orbital angular momentum and left and right handed circular polarization states $|L\rangle_\pi$ and $|R\rangle_\pi$, are eigenstates of the SAM operator S_π^z along the propagation direction of respective eigenvalues $s_\pi^z = \hbar$ and $s_\pi^z = -\hbar$. However LG modes are only a possible set of OAM eigenstates.

More in general, an OAM eigenstate is any spatial mode with azimuthal phase dependence as:

$$u(r, \varphi, z) = u_0(r, z)e^{il\varphi} \tag{2.22}$$

where $u_0(r, z)$ can be an arbitrary function.

This peculiar phase dependence corresponds to a twisting of the wavefront (see fig 2.4) of light around the propagation direction (helicoidal wavefront). The handness and the number of twisting of the wavefront are defined by the integer number l. The amplitude form 2.22 corresponds to a phase singularity on the propagation axis known as optical vortex. The topological charge of this vortex can be defined as:

$$Q = \frac{1}{2\pi} \oint d\chi \tag{2.23}$$

where the integral is performed around the singularity and χ is the phase of the field. For an orbital angular momentum eigenstate we have $Q = l$.

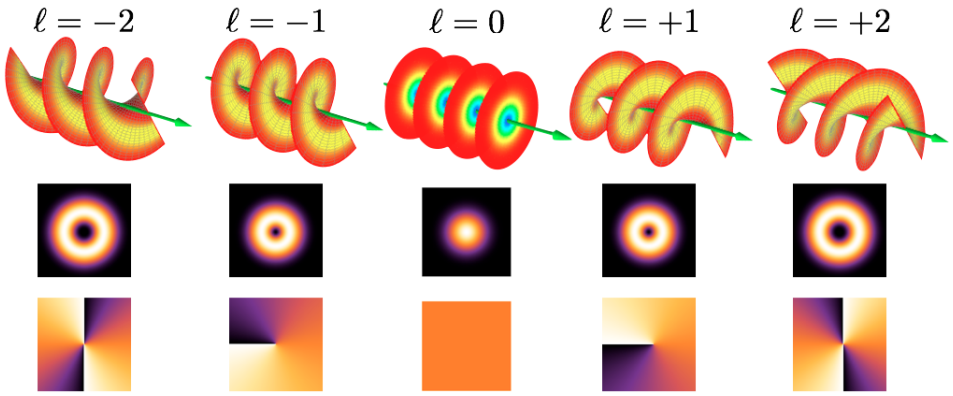

Figure 2.4. OAM eigenstates are characterized by an helicoidal wavefront and a "doughnut" intensity profile. Here are represented wavefront, intensity profile and phase profile for OAM eigenstates with $l \in \{-2, +2\}$

We can define an OAM eigenstate as $|l\rangle_{oam}$ and, since $\langle l_i|l\rangle_j = \delta_{i,j}$, we can exploit this degree of freedom to encode information in the infinite dimensional OAM Hilbert space with $l \in Z$. So as well as we have done with path, we can define an OAM qudit as:

$$|\phi\rangle = \sum_{l=1}^{d} \alpha_l |l\rangle_{oam} \tag{2.24}$$

where the sum runs from 1 to d only for convenience since l can also be a negative integer.

Hypergeometric Gaussian modes

Before conclude this section let us mention another family of OAM eigenstates, the Hypergeometric Gaussian (HyGG) modes [113] for which the complex amplitude is proportional to a confluent hypergeometric function. These states form an overcomplete set of solution for the paraxial equation and their complex amplitude in the pupil plane is given by:

$$u_{p,l}(r, \varphi, 0) = C_{p,l} r^{p+|l|} e^{-r^2 + il\varphi} \tag{2.25}$$

There can be defined several families of HyGG modes depending on the relation between p and l. In particular, for the states with $p = |l|$ we obtain the modified Bessel Beams which show the nice properties to have, in the pupil plane, the amplitude of a fundamental Gaussian beam multiplied by the phase factor $e^{il\varphi}$. This means that in principle we can generate an OAM eigenstate by simply adding a proper phase-shift to a TEM_{00} beam. Actually this is the most common way to generate OAM eigenstates as we will see in the next section.

2.3 OAM manipulation

Although orbital angular momentum is attracting large attention in the last decades, the set of tools for OAM manipulation is still under development in order to become as efficient as their counterparts used for polarization. Nevertheless there already exist several devices which allow to generate, manipulate and detect orbital angular momentum qudits in an efficient way. The most common devices for OAM manipulation are: spiral phase plates [24], cylindrical lens mode converters[23], computer generated holograms [105], interferometric setups [131][188], q-plates[140] and refractive devices for OAM sorting [128]. Among these we will briefly describe cylindrical lens mode converters and spiral phase plates since they are the first to have been developed and exploited in the experiments twenty years ago. Then we will focus on the q-plate and spatial light modulators: the former is a device which allows to couple OAM with polarization, the latter the most used and versatile tool for OAM encoding. Both these devices are the core of the experimental setup exploited in this thesis. The last section reports a novel device developed during this thesis which allows to transfer information between polarization and OAM of a single photon.

Cylindrical lens mode converter

The first tool that has been designed for OAM eigenstates generation is a cylindrical lens telescope that transforms HG modes in LG ones [23]. This conversion is based on the fact that LG modes and $HG(45°)$ modes (HG modes rotated by 45° respect to the HG along the propagation direction) can both be decomposed into a set of Hermite-Gauss modes.

Let us consider for instance the decomposition on HG basis of the LG_{02} mode:

$$LG_{02} = -\frac{1}{2}HG_{20} + \frac{i}{\sqrt{2}}HG_{11} + \frac{1}{2}HG_{02} \tag{2.26}$$

and the same decomposition for an $HG_{02}(45°)$ (see Fig.2.5):

$$HG_{20}(45°) = \frac{1}{2}HG_{20} + \frac{1}{\sqrt{2}}HG_{11} + \frac{1}{2}HG_{02} \tag{2.27}$$

The coefficients of the two decomposition differs only by phase factors, hence it is possible to convert a rotated HG beam in an LG mode by introducing a proper phase shift between the components.

This phase shift can be obtained with cylindrical lenses because, as each HG mode is focused by the lenses it undergoes a different Gouy phase shift depending on its mode indices and orientation with respect to the cylindrical lenses [23]. This mode converter has two main forms: the $\pi/2$ and the π converters which are characterized by different distances between the two cylindrical lenses. In a $\pi/2$ converter a $HG_{mn}(45°)$ (oriented at 45°) to the cylindrical axis of the lens) is converted into an LG_{pl} with $l = m - n$ and $p = min(n, m)$. The π converter, on the other hand, transforms any mode into its own mirror image and is optically equivalent to a Dove prism [99].

Spiral phase plates

As we have seen, OAM eigenmodes are characterized by a phase dependence of the complex amplitude of the field given by $e^{il\varphi}$. One of the simplest way to generate an OAM eigenstate is by introducing in a Gaussian beam an optical retardation which has exactly this azimuthal

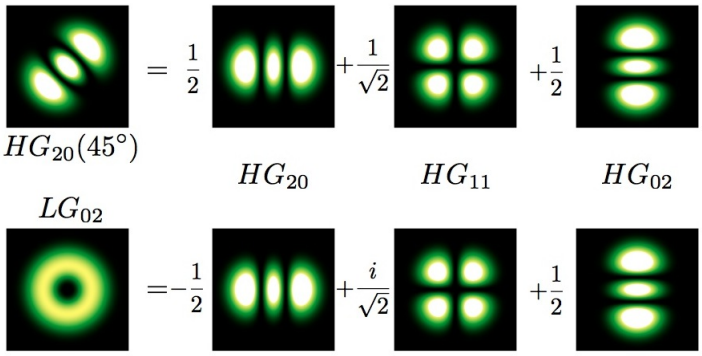

Figure 2.5. Mode decomposition for a LG_{02} beam and a rotated HG_{20} beam. The cylindrical lens mode converter working principle is based on the fact that the two decompositions differs only by phase factors.

dependence. This is the working principle of a spiral phase plate (SPP). A spiral phase plate is a disk of transparent material in which the thickness is a linear function of the azimuthal angle (in a polar reference frame with the origin in the center of the disk) see fig 2.6. The phase retardation introduced by a spiral phase plate in the beam is then:

$$\delta = \frac{(n_1 - n_2)h}{\lambda}\varphi \tag{2.28}$$

where n_1 and n_2 are respectively the refractive index inside and outside the device, h is the difference between maximum and minimum of the thickness, λ is the wavelength of the beam. In order to obtain an OAM eigenstate $|l\rangle_{oam}$, the SPP has to be carefully constructed such that:

$$h = \frac{l\lambda}{(n_1 - n_2)}. \tag{2.29}$$

It is clear from this condition that a SPP can work only with a fixed wavelength. When we shine the device with a TEM_{00} we obtain a modified Bessel beam with a well defined l:

$$SPP|0\rangle_{oam} = |l\rangle_{oam} \tag{2.30}$$

Let us note that a spiral phase plate can only generate the state $|l\rangle$ given an input TEM_{00} beam which makes this device not suitable for the generation of qudits.

2.3.1 Q-plate

In order to generate hybrid qudits a device is needed which acts as an interface between two degrees of freedom. When the two degrees of freedom are polarization and OAM, this interface has to be birefringent and inhomogeneous.

A q-plate [140] is a liquid crystal (LC) cell that acts as a birefringent phase plate whose optical axis orientation angle is not uniform, but changes from point to point in the transverse plane. The optical axis orientation at each point is given by:

$$\alpha(r, \varphi) = q\varphi + \alpha_0, \tag{2.31}$$

where α is the angle that the optical axis forms with a reference axis x in the transverse plane xy, φ is the azimuthal angle coordinate in the same plane, q is a parameter called

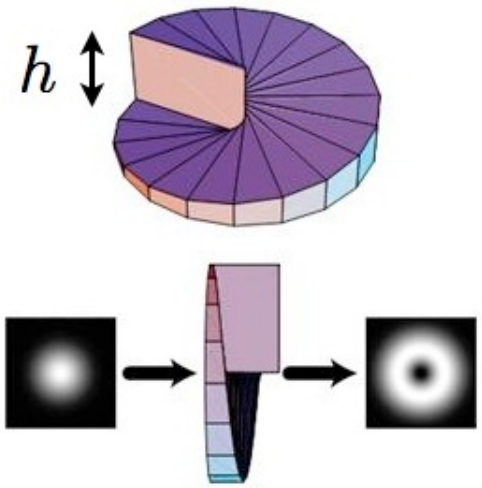

Figure 2.6. Graphic representation of a spiral phase plate. A Gaussian beam incident on the device is converted in a OAM eigenstate.

topological charge and α_0 is a constant. Being a liquid crystal device, in a q-plate the optical axis orientation coincides with the molecular director of liquid crystals and, from the border condition $\alpha(r, 0) = \alpha(r, 2\pi)$ follows the condition for q to be an integer or half integer. In figure 2.7 are shown the molecular directors geometries for q-plates with different q and α_0.

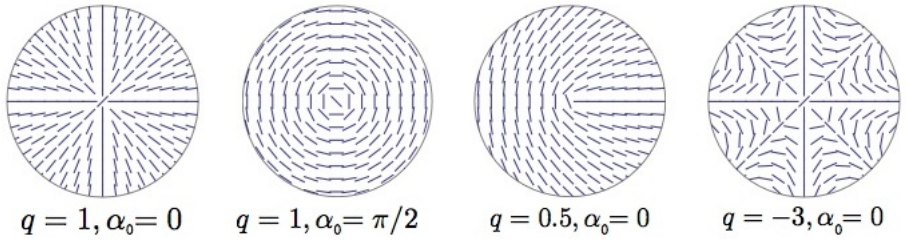

Figure 2.7. Some optical axes geometries for the q-plate device.

As a liquid crystals cell the q-plate introduces a birefringent retardation δ which is uniform across the device and which can be manipulated by acting on an external electric field [169]. For $\delta = \pi$, when a circularly polarized photon passes through a q-plate, its helicity is switched to the opposite one, like in the case of standard half-wave plates. Such polarization transformation, while having the same initial and final states, occurs in a different way in different points of the transverse plane, giving rise to a non-uniform geometrical (or Pancharantam-Berry) phase retardation. More in detail, let us consider the Jones matrix describing the action of a q-plate with optical retardation δ:

$$QP(\delta) = R[-\alpha] \begin{pmatrix} e^{i\delta/2} & 0 \\ 0 & e^{i\delta/2} \end{pmatrix} R[\alpha] \tag{2.32}$$

where R is the rotation matrix and α is given by 2.31. A straightforward calculation of the

action of the q-plate on circular polarized light gives:

$$QP(\delta)|L\rangle_\pi = \quad cos\left(\frac{\delta}{2}\right)|L\rangle + ie^{i2\alpha_0} sin\left(\frac{\delta}{2}\right)|R\rangle_\pi \quad e^{i2q\varphi} \tag{2.33}$$

$$QP(\delta)|R\rangle_\pi = \quad cos\left(\frac{\delta}{2}\right)|R\rangle + ie^{-i2\alpha_0} sin\left(\frac{\delta}{2}\right)|L\rangle_\pi \quad e^{-i2q\varphi} \tag{2.34}$$

where the azimuthal phase dependence of OAM eigenstates is given by the term $e^{\pm i2q\varphi}$. Hence, when $\delta = \pi$ (tuning condition) a q-plate gives rise to the following transformations:

$$QP(\pi)|L\rangle_\pi|l\rangle_{oam} = \quad |R\rangle_\pi|l + 2q\rangle_{oam} \tag{2.35}$$

$$QP(\pi)|R\rangle_\pi|l\rangle_{oam} = \quad |L\rangle_\pi|l - 2q\rangle_{oam} \tag{2.36}$$

which correspond to a flip in the polarization state and a variation of OAM $\Delta l = \pm 2q$ whose sign depends on the input polarization handess. For sake of simplicity we will refer now on to tuned q-plates ($\delta = \pi$) as QP instead of $QP(\pi)$.

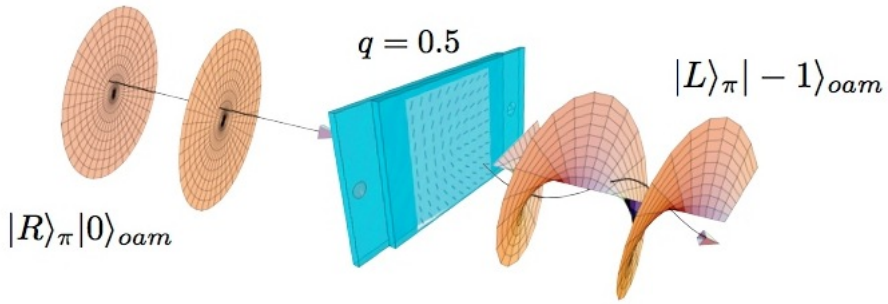

Figure 2.8. Sketch of a q-plate with q=0.5 generating a polarization-OAM hybrid state.

According to transformation 2.35, the action of the q-plate on a horizontal polarized photon is:

$$QP|H\rangle_\pi|0\rangle_{oam} = \frac{1}{\sqrt{2}}\left(|L\rangle_\pi|-2q\rangle_{oam} + |R\rangle_\pi|2q\rangle_{oam}\right) \tag{2.37}$$

which corresponds to an entangled state between two DOF of the same photon and is defined in a four dimensional hybrid space spanned by vectors:

$$\{|H, 2q\rangle, |H, -2q\rangle, |V, 2q\rangle, |V, -2q\rangle\} \tag{2.38}$$

This ququart space has been exploited both for fundamental quantum mechanics investigation and quantum communication [70, 71, 149, 50, 68] as will be described in the following chapters (Chapters 3,4 and 5).

Q-plates fabrication

In a q-plate a thin layer of nematic LC is sandwiched between two glass windows, previously covered with a suitable surface coating for inducing the desired orientational order to the LC layer. For generating the q-plate pattern is adopted a photoalignment method [59], which consists in exposing the aligning layer, which contains suitable photosensitive dyes, with linearly polarized UV light (see Fig.2.9). The polarization direction of the light defines the local anisotropy direction of the aligning coating (the latter is actually orthogonal or parallel to the polarization, depending on the choice of materials), which in turn, induces

the orientation direction of the LC layer. Hence, the q-plate is realized by illuminating the empty cell with a thin line of light, "writing" sector-by-sector the desired angular structure, while constantly controlling the polarization direction of the writing beam and rotating the sample at the same time. The LC is inserted in the cell after writing the alignment pattern. The cell glasses include also a thin conducting transparent layer of Indium Tin Oxide (ITO), in order to apply an electric field and fine-tune the q-plate to the desired total retardation of half-wave.

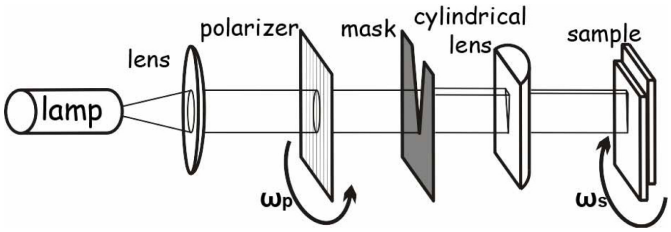

Figure 2.9. Photoalignment setup for q-plates fabrication. The light produced by a UV lamp is polarized and sent through a mask before shine the sample. Both rotational speed of polarization ω_p and sample ω_s can be controlled[189].

The output OAM state quality is defined by the smoothness of the q-plate and the size of central defect. The first one is defined by the sample rotation step, laser line thickness and the choice of the aligning surfactant material. The central defect size is also very sensitive to the alignment of the sample with respect to the writing beam. For low topological charges $q < 10$, a step of 1° and corresponding laser line thickness provides good quality of the final structure. With increase of topological charge, finer q-plate structures required smaller rotation steps (up to 0.1° for $q \geq 25$) and particular attention to rotation error compensation. In combination with suitable azodyes selected as high resolution aligning surfactants [59], it is possible to achieve a high quality of the LC alignment and a low size, with respect to the total aligned area, of the central defect (see Figure 2.10 for polarization microscope image of a q-plate). Up to now q-plates with topological charge as high as $q = 150$ have been fabricated with a mean transmittance of 84% which can be easily improved by applying an antireflection coating on the surfaces of the device.

Figure 2.10. Polarization microscope image of a q-plate. The image shows pictures of three different q-plates between crossed polarizers. For $q = 150$ an area located approximately 1 mm from the center is shown and image size is 366 μm in horizontal and 275 μm in vertical.

2.3.2 Spatial light modulators

Another technique for OAM generation is based on holography [91]. A hologram is the registration of the interference pattern between a target field and a reference field. By

shining the hologram with the reference beam we are able to reconstruct back the target field. Although the first holograms were actually produced by impressing the interference pattern on a photographic film, nowadays they are usually calculated analytically or, eventually, numerically. There exist two kind of holograms:

- amplitude holograms
- phase holograms

In the first case the hologram consists of a modulation of the amplitude of the field corresponding to a real transmission function $T(x, y)$. In the second case $T(x, y)$ represents a phase modulation. It is clear that, being transparent, in general phase modulation holograms assure higher efficiencies respect to amplitude ones. Therefore hereafter we will refer only to phase holograms.

By following the same working principle of a spiral phase plates, the state $|l\rangle_{oam}$ can be generated by adding an azimuthal phase term to a Gaussian beam by letting it pass through a phase hologram with $T(r, \varphi) = l\varphi$. This technique has been first used in [105] and its main drawback is that, since holograms have low diffraction efficiency, the converted beam is superimposed to the non-converted Gaussian beam.

To avoid this problem it is possible to add to the azimuthal phase a blazing term that sends to the first order of diffraction the converted beam. The corresponding transmission function is $T(x, y) = 2\pi x/\Lambda_x + ilTan^{-1}(y/x)$ where Λ_x is the blazing parameter along the direction of x. With this hologram the photons converted to state $|l\rangle_{oam}$ are spatially separated from the unconverted ones in the state $|0\rangle_{oam}$. Thus hologram couples OAM and path with the following transformation:

$$|0\rangle_{oam}|a\rangle_k \rightarrow \sqrt{\eta}|l\rangle_{oam}|b\rangle_k + \sqrt{1-\eta}|0\rangle_{oam}|a\rangle_k \tag{2.39}$$

where η is the diffraction efficiency of the hologram, $|b\rangle_k$ is the first diffraction order direction and contributions related to other diffraction orders are neglected .

When a hologram is calculated by a computer it is called computer generated hologram and it is usually displayed on a device called Spatial Light Modulator (SLM). These devices comprise thin liquid crystal cells, where the application of a voltage across the cell introduces a phase delay to the transmitted light. Rather than applying the same electric field (and hence the same phase change) across the whole aperture, a desired phase structure can be created by varying the strength of the electric field across the aperture of cell. Most commonly, this spatially varying electric field is created by attaching the liquid crystal cell to a programmable, pixellated CMOS array and using the whole device in reflection mode (which also doubles the available phase shift). Typically, in a good quality SLM, each pixel of the device can create a full 2π phase shift with video resolution and update rates. These devices are programmed as secondary monitors from the graphics card of a computer, where an 8-bit greyscale image gives 256 different phase levels. When adopted in this configuration, the SLM is effectively acting as a complicated diffraction grating which changes the phase of the reflected light beam such that upon propagation its intensity and phase cross-section transforms into a specific pattern. The main advantage of an SLM respect to a photographic film is that it can change dynamically (even automatically) the holographic pattern without need of further alignment.

A typical setup with an SLM is shown in figure 2.11.

As we have seen, an OAM eigenstate can be easily generated by displaying on a SLM the transmission function $T(x, y) = 2\pi x/\Lambda_x + ilTan^{-1}(y/x)$. Actually, since SLM

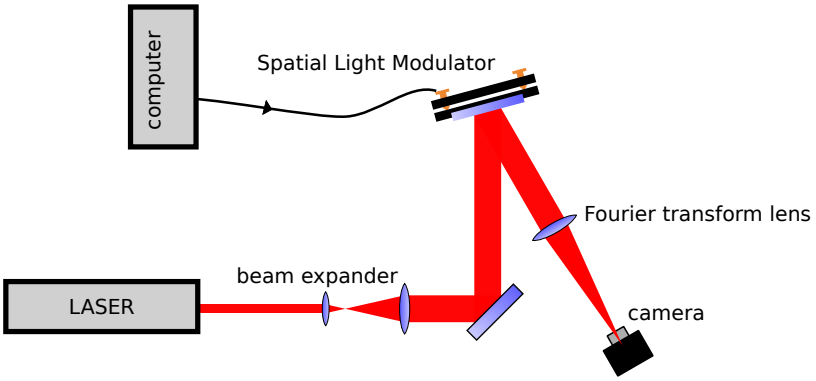

Figure 2.11. A typical experimental setup for beam modulation via a spatial light modulator.

can create a phase shift of 2π we need to slightly change this transmission function to $T(x,y) = \text{Mod}[2\pi x/\Lambda_x + ilTan^{-1}(y/x), 2\pi]$ (where Mod is the modulo function that gives the remainder after division of the first argument by the second) which corresponds to a typical modulation called fork hologram (see fig 2.12). Although high quality SLMs have as a maximum phase shift 2π, in cheaper models this can be not true. However it is still possible to adjust SLM's contrast function in order to optimize the diffraction efficiency with a technique described in [38].

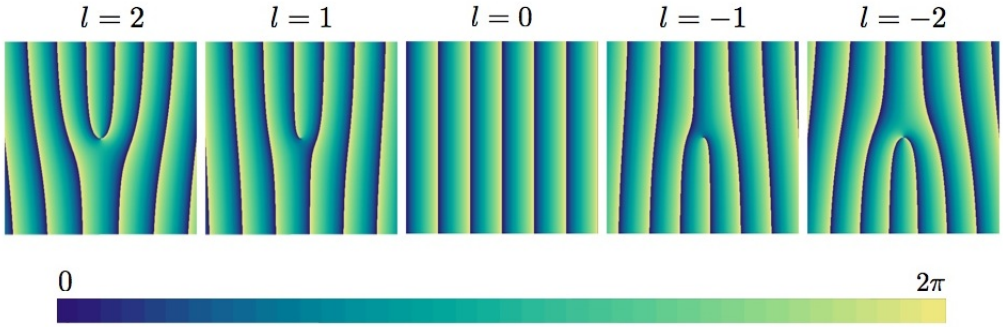

Figure 2.12. Fork holograms for generation of states $|l\rangle_{oam}$ with $l \in [-2, 2]$

The greatest advantage of SLMs respect to all the other devices for OAM manipulation is that they in principle allow to generate and detect qudits of arbitrary dimensions. Despite of the semplicity of the holograms for OAM eigenstates generation, the calculation of the proper hologram for a generic qudit is not straightforward. The fundamental challenge of computer generated holography is actually how to find the hologram design which, when displayed on the SLM, generates the light field we want to create. In other terms, assuming that we illuminate the SLM with a plane wave laser beam of uniform intensity, our scope is to find the right phase pattern $T(x,y)$ to display on SLM in order to obtain the complex field distribution in the far-field (in the focal plane of the lens in Fig2.11). The main problem here is that the SLM is a phase-only optical element, while to obtain arbitrary OAM modes superpositions we need to be able to tailor both the phase and the amplitude transverse profiles of the outgoing field. This can be obtained by modulating both the shape and contrast of the hologram. Although there exist several techniques based on selective losses controlled through the contrast [12, 38] they are non-optimized for the best state fidelity. Since we are interested in the generation of qudits we want them to be as pure as possible.

For this reason, we developed an holographic method that is specifically optimized in the fidelity and that is described in Chapter 6.

Hence a spatial light modulator allows to transform a TEM_{00} mode in an arbitrary superposition of OAM eigenstates:

$$|0\rangle_{oam} \longrightarrow \sum_{l=1}^{d} \alpha_l |l\rangle_{oam} \tag{2.40}$$

and in general to perform an arbitrary rotation of a qudit in its d-dimensional Hilbert space. Moreover, since they are computer controlled, SLMs are suitable for integration in automatized setups. For these reasons spatial light modulators are nowadays the most diffuse resource for OAM manipulation.

2.4 Deterministic Transferrer

A *transferrer* is a device that transfers information from one DOF to another. In reference [151] is described the realization of the first transferrer between the polarization space π and a bidimensional subspace of OAM $o_{|l|} = \{|-l\rangle_{oam}, |+l\rangle_{oam}\}$ based on q-plate technology. However the reported probability of success for the transfer is only $p = 50\%$ since some elements in the setup discard half of the information encoded in different OAM subspaces ($o_{|l|} \to \pi$) or in the polarization ($\pi \to o_{|l|}$). Since a useful quantum information processing requires high efficiencies, one goal for this thesis project has been the realization of a deterministic transferrer ($p = 100\%$) between π and $o_{|l|}$. The results have been published in [V. D'Ambrosio, E. Nagali, C. Monken, S. Slussarenko, L. Marrucci and F. Sciarrino, *Deterministic qubit transfer between orbital and spin angular momentum of single photons.* Optics Letters, 37 (2012), 172.] [69].

2.4.1 Transferrer working principle

Let us consider the $o_{|l|} \to \pi$ transfer process and an incoming photon prepared in an arbitrary OAM and fixed polarization state, so that all information is encoded in the OAM:

$$|H\rangle_\pi |\phi\rangle_{o_{|l|}} = |H\rangle_\pi (\alpha|+l\rangle + \beta|-l\rangle)_{o_{|l|}} \tag{2.41}$$

The transfer process starts with a half waveplate (HWP) whose optical axes is rotated by $\pi/8$ respect to horizontal polarization that transforms the polarization state in the antidiagonal one $|A\rangle_\pi$. The states then becomes:

$$|H\rangle_\pi (\alpha|+l\rangle + \beta|-l\rangle)_{o_{|l|}} + |V\rangle_\pi (\alpha|+l\rangle + \beta|-l\rangle)_{o_{|l|}} \tag{2.42}$$

Hereafter the indices π and $o_{|l|}$ are omitted for brevity. The photon is then sent into a polarizing Sagnac interferometer (PSI) with a polarizing beam-splitter (PBS) input/output port and a Dove prism (DP) in one of its arms [152, 188]. Defining γ as the angle between the base of the prism and the plane of the interferometer, the action of the DP on the counter-propagating H/V linear polarization components with generic OAM l is described by the following equations:

$$|H\rangle|l\rangle \quad \to \quad e^{2il\gamma}|H\rangle|l\rangle, \tag{2.43}$$

$$|V\rangle|l\rangle \quad \to \quad e^{-2il\gamma}|V\rangle|l\rangle \tag{2.44}$$

where the OAM-inverting effect of the reflections can be ignored, for simplicity, as long as the total number of reflections in the setup is even. Thus the two components of state 2.42 in the PSI evolve as:

$$\alpha|H\rangle|+l\rangle + i\beta|H\rangle|-l\rangle \rightarrow \alpha e^{2i\gamma l}|H\rangle|+l\rangle + i\beta e^{-2i\gamma l}|H\rangle|-l\rangle,$$

$$\alpha|V\rangle|+l\rangle - i\beta|V\rangle|-l\rangle \rightarrow \alpha e^{-2i\gamma l}|V\rangle|+l\rangle - i\beta e^{2i\gamma l}|V\rangle|-l\rangle.$$

Setting $\gamma = \pi/(8l)$ and applying these transformations to state 2.42, we obtain (up to a global phase factor) the output state:

$$\alpha|R\rangle|+l\rangle + \beta|L\rangle|-l\rangle.$$

By passing through a q-plate with $2q = l$, such state is finally transformed in:

$$(\alpha|L\rangle + \beta|R\rangle)|0\rangle_o = |\phi\rangle_\pi|0\rangle_o$$

that completes the transfer.

Since all the intermediate transformation steps are unitary, they are deterministic and reversible. The inverse process $\pi \rightarrow o_{|l|}$, is therefore obtained by simply inverting the light propagation direction through the same components. It is also interesting to note that the action of the transferrer is not limited to a $+l$ and $-l$ OAM subspace, but it works with any pair l_1, l_2 of OAM values. By repeating the analysis above, one finds that the transfer is ensured as long as the following general condition on the DP angle is satisfied:

$$\gamma = \frac{\pi}{4(l_1 - l_2)}. \tag{2.45}$$

2.4.2 Experimental realization

The photon source described in the next subsection has provided the input photon states for all the experiments realized in this thesis project. The description of the photon source will be then omitted in all the following chapters.

Entangled photon source

The optical source (see Fig.2.13) for the transferrer experiment is based on a non-linear effect known as *Spontaneous parametric down conversion* (SPDC) which allows to generate couples of entangled photons [125]. More in detail, a Ti:Sa mode-locked laser generates pulses of $\Delta t = 120 fs$ with repetition rate of 76 MHz and wavelength $\lambda = 795$ nm which are doubled in frequency via a second harmonic generation process to obtain a pump beam of power $P = 700$ mW and $\lambda = 397.5$ nm. The pump beam is then focused onto a beta-barium-borate crystal (BBO) of length $l = 1.5$ mm where a type-II SPDC takes place. The output photons are then filtered in frequency with a $\Delta\lambda = 3$ nm filter (IF) and coupled in single-mode fibers which act as a passing filter for the $m = 0$ OAM mode. As a result we have two output photons in the Bell singlet state:

$$|\psi^-\rangle = \frac{1}{\sqrt{2}}\left(|H,0\rangle_A|V,0\rangle_B - |V,0\rangle_A|H,0\rangle_B\right) \tag{2.46}$$

which is generated with a mean fidelity of 99% and which is an optimal starting point for polarization and OAM based experiment. The Bell basis can be completed by generating

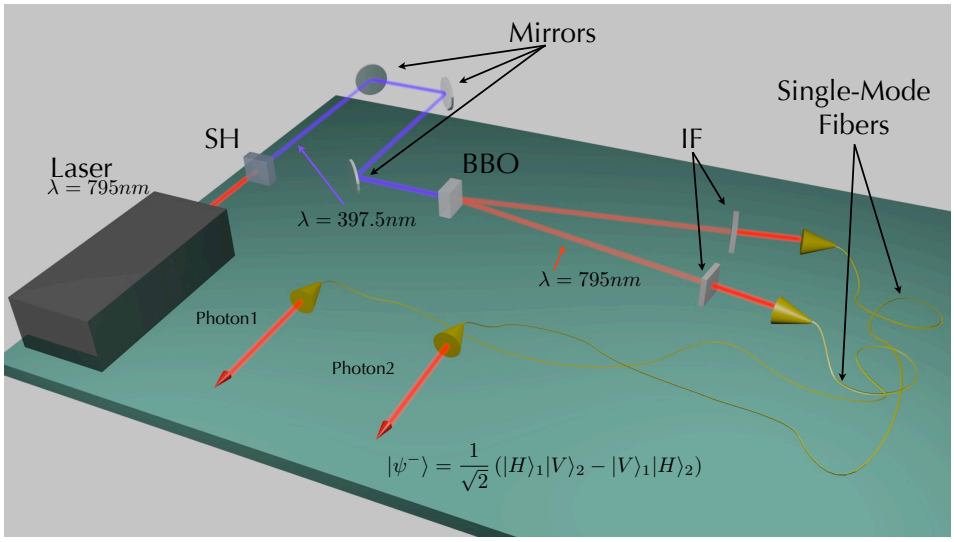

Figure 2.13. Optical source for the generation of coupled photons in the singlet Bell state: Laser light generated by a Ti:Sa laser is doubled in frequency by a second harmonic generation process in the non-linear crystal (SH). The second harmonic light is then sent through a beta-barium-borate (BBO) crystal where spontaneous parametric down conversion takes place. The two resulting photons are then filtered in frequency by filters (IF) and coupled to single mode fibers. The resulting state is a two photon Bell state $|\psi^-\rangle$.

states $|\psi^+\rangle, |\phi^-\rangle, |\phi^+\rangle$ which can be obtained by applying to $|\psi^+\rangle$ a suitable operator that is easily realized by exploiting the action of birefringent waveplates on one of the photons.

$$|\psi^+\rangle = \sigma_z^B|\psi^-\rangle = HWP_0^B|\psi^-\rangle \quad (2.47)$$

$$|\phi^-\rangle = \sigma_x^B|\psi^-\rangle = HWP_{\pi/4}^B|\psi^-\rangle \quad (2.48)$$

$$|\phi^+\rangle = \sigma_y^B|\psi^-\rangle = HWP_0^B HWP_{\pi/4}^B|\psi^-\rangle \quad (2.49)$$

where HWP_x^B indicates a half wave plate acting on photon B and whose optical axis is rotated of an angle x respect to the direction of horizontal polarization. Although these states are two photon entangled states, single photon experiment can be easily performed by exploiting one of the photons as a trigger (heralded photon configuration). Moreover, since the orbital angular momentum of both photons in initialized to $l = 0$ by single mode fibers, such a state is a perfect starting point for OAM generation and manipulation through devices like q-plates and spatial light modulators.

Transferrer setup

The experimental setup we used for demonstrating the deterministic $o_2 \rightarrow \pi$ transfer process can be divided in three sections: (i) encoding of the input OAM qubit, (ii) quantum transferrer, and (iii) output state analysis (see Fig.2.14).

(i) One of the two entangled photons is sent to a detector and acts as a trigger while the other one is sent to the setup in Fig.2.14. A polarizing beam-splitter (PBS) projects the photon onto the state $|H\rangle_\pi$. A quarter waveplate (QWP) and a half-waveplate (HWP) are then used for encoding an arbitrary qubit $\alpha|H\rangle_\pi + \beta|V\rangle_\pi$ in the polarization degree of freedom of the photon. Finally, this qubit is converted into a OAM-encoded one using the $\pi \rightarrow o_2$ *probabilistic* transferrer, as described in [151, 152]. For this step we used

a q-plate with $q = 1$ combined with a PBS, providing conversion into the photon state $|\phi\rangle_{o_2} = \alpha|+2\rangle + \beta|-2\rangle$ with a probability $p = 0.5$. This completes the input state preparation stage of our apparatus (generation box in Fig.2.14).

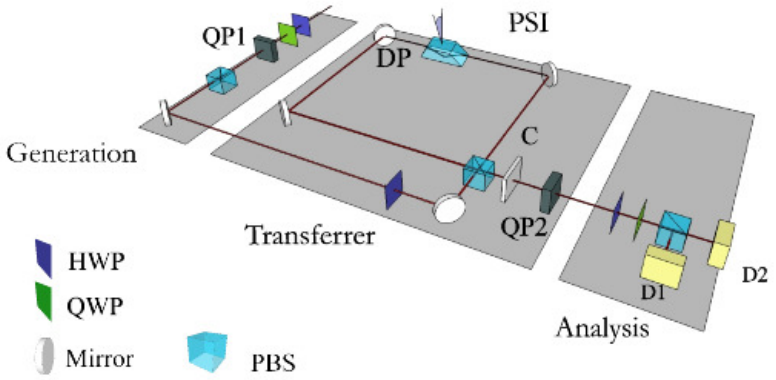

Figure 2.14. Experimental setup adopted for the implementation of the deterministic quantum transferrer $o_2 \to \pi$. The input photon is prepared by a probabilistic transferrer ($\pi \to o_2$) (first two waveplates, QP1 and PBS) into an arbitrary o_2 state with polarization H. After the generation stage, the deterministic transfer ($o_2 \to \pi$) is obtained through the PSI and the QP2 . The outgoing polarization state is analyzed in the last part of the setup (waveplates, PBS, detectors D1 and D2). C is a phase compensation stage to correct all the unwanted phase shifts introduced by the setup.

(ii) The input qubit $|\phi\rangle_{o_2} = \alpha|+2\rangle + \beta|-2\rangle$ is set by a HWP to polarization state $|A\rangle$ and then injected in the PSI. The first PBS of the Sagnac interferometer splits the two polarizations in two opposite directions within the PSI, both passing through a DP rotated at angle $\gamma = \frac{\pi}{16}$. The state is then sent through a q-plate (QP2), which transforms the input state to $\alpha|L\rangle + \beta|R\rangle = |\varphi\rangle_\pi$ with $l = 0$. Thus the information initially encoded in the OAM has been transferred to the polarization degree of freedom.

(iii) At this stage the polarization qubit can be measured by a standard analysis setup which consists of birefringent waveplates and a polarizing beam splitter, which form the final section of our apparatus. The transmitted and reflected photons from the PBS are coupled to single mode fibers and detected by single photon counter modules D_1 and D_2. In order to perform a full qubit tomography, the output of the deterministic transferrer has been analyzed in the three polarization bases $\{|R\rangle, |L\rangle\}, \{|H\rangle, |V\rangle\}, \{|A\rangle, |D\rangle\}$, recording the coincidence counts between detectors $[D_1, D_T]$ and $[D_2, D_T]$ where D_T refers to trigger detector.

The transferrer has been testes for all the states belonging to the three mutually unbiased bases spanning the bidimensional OAM subspace with $|l| = 2$ (o_2): $\{|+2\rangle, |-2\rangle\}, \{|h\rangle, |v\rangle\}, \{|a\rangle, |d\rangle\}$, where, analogously to the polarization case, we define linear superpositions of $|+2\rangle$ and $|-2\rangle$ as $|h\rangle = \frac{1}{\sqrt{2}}(|+2\rangle + |-2\rangle), |v\rangle = \frac{1}{i\sqrt{2}}(|+2\rangle - |-2\rangle)$ and $|a\rangle = \frac{1}{\sqrt{2}}(|h\rangle + |v\rangle), |d\rangle = \frac{1}{\sqrt{2}}(|h\rangle - |v\rangle)$.

The overlap between the input OAM qubit and the polarization output one after the

transferrer has been estimated through the fidelity parameter $F = \frac{C_\psi}{C_{tot}}$ where C_ψ is the number of photon counts recorderd when the state $|\psi\rangle$ is projected over itself and C_{tot} is the total number of coincidences in the base $\{|\psi\rangle, |\psi^\perp\rangle\}$. All results are summarized in Table 2.1, showing that very good values of transfer fidelity are obtained. All the errors have been estimated by considering a Poissonian statistics for the photon counts.

Although ideally the probability of success for the transfer is $p = 1$, the actual value is

State	Fidelity
$\|+2\rangle$	(0.994 ± 0.003)
$\|-2\rangle$	(0.992 ± 0.003)
$\|h\rangle$	(0.982 ± 0.005)
$\|v\rangle$	(0.944 ± 0.008)
$\|a\rangle$	(0.992 ± 0.003)
$\|d\rangle$	(0.980 ± 0.005)
Average value	(0.980 ± 0.002)

Table 2.1. Experimental fidelity of the qubit transfer.

limited by standard optical losses in the optical components (mainly reflections, plus a little scattering and absorption) and by the final single-mode fiber coupling step that we used for experimental convenience and for mode purification, thus leading to an overall efficiency of 0.324. This value is three times larger than the one achieved with the probabilistic device [152]. The obtained improvement is attributed to the adoption of the deterministic scheme based on the Sagnac interferometer, to more efficient q-plates and to a better mode conversion exemplified by a higher single-mode coupling efficiency (compared to the one measured with previous q-plates) equal to 0.30. As further improvements the reflection losses could be reduced by adopting anti-reflection coating (in particular the q-plates are currently uncoated). Finally we note the single-mode fiber coupling (currently 0.5), although convenient for further processing of the output photons, is not a strictly required step.

The deterministic transferrer can be exploited in order to encode two qubits in a single photon. Indeed, if a qubit is encoded for instance in the π space, a second qubit can be added in the π space, once that the $\pi \rightarrow o_{|l|}$ transfer has been completed for the first one. These two qubits can then be decoded by exploiting another transferrer to perform the

$$o_{|l|} \rightarrow \pi$$

transfer on the first qubit, once that the second one has been measured with standard polarization analysis setup. This feature makes the deterministic transferrer a useful resource for hybrid ququart analysis as we will se in Chapter 5.

Chapter 3

Alignment-free quantum communication

In this chapter we present a work in which the properties of hybrid qudits are exploited to realize quantum communication (QC) when the two users are lacking a shared reference frame. In particular we experimentally show that, by identifying a proper subspace of a four-dimensional space obtained by combining polarization and OAM, it is possible to perform quantum communication protocols and violate CHSH inequalities without any information about the reference frame orientation of the two parties (except the direction of propagation of the photons). Such feature allows to overcome a main obstacle to long distance free-space communication and could find application for instance in satellite based communication schemes.

The obtained results have been published in [V. D'Ambrosio, E. Nagali, S. P. Walborn, L. Aolita, S. Slussarenko, L. Marrucci, F. Sciarrino, *Complete experimental toolbox for alignment-free quantum communication*, Nature Communications 3, 961 (2012)].

3.1 The problem of reference frame

Photonic free-space quantum communication has been demonstrated for distances of hundreds of kilometers [200], a progress that could lead to satellite-based long-distance QC [176, 14, 203, 36]. However, standard approaches to QC, for example based on encoding qubits into the polarization of photons, require that all users involved have knowledge of a *shared reference frame* (SRF). For instance, in the bipartite scenario, the emitter and receiver, conventionally called Alice and Bob, must initially align their local horizontal (H) and vertical (V) transverse axes, and then keep them aligned throughout the transmission (see Fig. 3.1 **a**). This in turn requires the exchange of a large (strictly speaking, infinite) amount of classical information, a technically demanding overhead that can impose very serious obstacles [167, 20]. Particularly dramatic are the situations where the users are very far apart from each other, the misalignment between their frames varies in time, or the number of users is large. In general, the lack of a SRF inhibits faithful QC because it is equivalent to an unknown relative rotation, therefore introducing noise into the quantum channel [20].

A possible solution to this problem is to exploit multi-qubit entangled states that are invariant under single-qubit rotations acting collectively on all the qubits (see [205, 34, 37] and references therein). These constitute particular instances of decoherence-free subspaces,

originally introduced in the context of fault-tolerant quantum computing [161, 214, 135]. The idea is thus to encode logical qubits into rotationally invariant states of multiple physical qubits. These can in principle be realized with multiple photons [205, 34, 37]. However, the efficient production and detection of multi-photon states is a technological challenge, they are more susceptible to losses, and the requirement that multiple photons are subject to exactly the same rotation is very seldom perfectly satisfied.

A more efficient way to circumvent misalignments is based on single photon hybrid ququarts encoded in polarization and the OAM as will be clear in the next section.

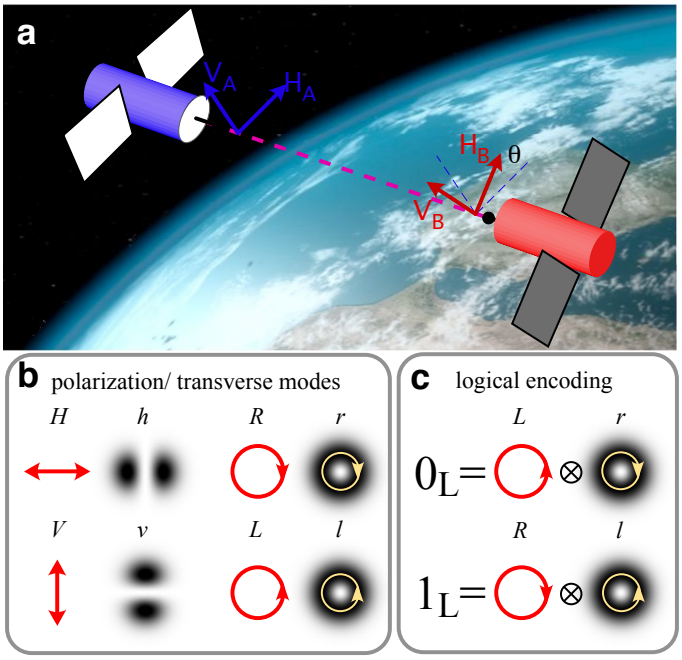

Figure 3.1. Rotational invariant single-photon qubits. a) A faithful free-space quantum communication between two users (Alice and Bob here depicted as satellites) needs in general a shared reference frame. When the information is encoded into polarization of single photons, such reference frame is represented by the relative orientation between horizontal (H) and vertical (V) axes of the two users. Alice and Bob need to carefully control their mutual orientation in order to avoid decoherence in the communication channel is induced by misalignment. **b)** Qubits can be equivalently encoded in both polarization and transverse modes: H/V denote horizontal/vertical linear polarizations, L/R left/right circular polarizations, h/v horizontal/vertical first-order Hermite-Gauss modes, and l/r left- and right-handed first-order Laguerre-Gauss modes. The L/R polarizations are eigenstates with eigenvalues $\pm\hbar$ of the spin angular momentum (SAM), whereas the l/r modes are the equivalent eigenstates of the orbital angular momentum (OAM). **c)** By combining SAM and OAM eigenstates of opposite handedness, two null-eigenvalue eigenstates of the total angular momentum arise. Both these hybrid states are invariant under rotations around the propagation axis, and can therefore encode misalignment-immune logical qubit states, called 0_L and 1_L.

3.2 Hybrid Rotational Invariant Qubits

In order to understand how a subspace of a ququart space can be rotational invariant, let us consider again Alice and Bob encoding qubits in photon polarization and an arbitrary misalignment $R[\theta]$ between their reference frames given by a physical rotation of an angle θ

along the propagation axis. Given $R[\theta]$ in the basis $\{|H\rangle, |V\rangle\}$ as:

$$R[\theta] = \begin{pmatrix} Cos(\theta) & Sin(\theta) \\ -Sin(\theta) & Cos(\theta) \end{pmatrix} \tag{3.1}$$

every polarization qubit will undergo the following transformation (written for simplicity in the circular polarization basis):

$$\begin{aligned} R[\theta]|L\rangle &= e^{i\theta}|L\rangle \\ R[\theta]|R\rangle &= e^{-i\theta}|R\rangle \end{aligned} \tag{3.2}$$

which shows how the rotation $R[\theta]$ corresponds to noise (in this case a phase shift) in the communication channel.

Let us now consider the effect of the same rotation $R[\theta]$ on OAM eigenstates. These eigenstates are characterized by an azimuthal phase dependence of $e^{im\phi}$, hence they will undergo the following transformation:

$$R[\theta]|m\rangle = e^{im\theta}|m\rangle \tag{3.3}$$

We can exploit such effect to realize rotational invariant qubits by restricting our attention to the OAM subspace with $m = \pm 1$ and properly combine together polarization and OAM. From now until the end of the chapter we will rename these OAM eigenstates as: $|+1\rangle = |l\rangle$ and $|-1\rangle = |r\rangle$ in analogy with polarization eigenstates. The rotational invariant logical basis will be:

$$\begin{aligned} |0\rangle_L &= |L\rangle|r\rangle \\ |1\rangle_L &= |R\rangle|l\rangle \end{aligned} \tag{3.4}$$

Indeed any rotation $R[\theta]$ will leave such states unaffected since the phase shift related to the polarization state will be exactly cancelled out by the phase shift of the OAM eigenstate, no matter what the angle θ is. This logical basis is a decoherence free subspace of the particular ququart space obtained from the tensor product of polarization and bidimensional OAM subspace with $m = \pm 1$. Because of linearity, any coherent superposition (or incoherent mixture) of the two logical states, i.e. the entire logical subspace, is also immune to all possible reference frame misalignments during the entire QC session.

3.3 Experimental implementation

The experimental setup used to encode and decode arbitrary hybrid qubit states in the logical basis is shown in Fig. 3.2. Polarization qubits are encoded in single photons generated by SPDC (see section 2.4.2) which are then sent to a tuned q-plate with topological charge $q = 1/2$ to convert polarization qubit into rotational invariant qubit. Indeed such q-plate gives rise to the following transformations:

$$\begin{aligned} |R\rangle_\pi|0\rangle_{oam} &\xrightarrow{q-\text{plate}} |L\rangle_\pi|r\rangle_{oam} &&= |0\rangle_\text{L} \\ |L\rangle_\pi|0\rangle_{oam} &\xrightarrow{q-\text{plate}} |R\rangle_\pi|l\rangle_{oam} &&= |1\rangle_\text{L}, \end{aligned} \tag{3.5}$$

where $|0\rangle_{oam}$ denotes a zero OAM state, such as the TEM_{00}. Consider then a generic polarization-encoded qubit $|\psi\rangle_\pi = \alpha|R\rangle_\pi + \beta|L\rangle_\pi$ prepared in the TEM_{00} spatial mode. From transformations (3.5), sending the qubit through the q-plate yields

$$|\psi\rangle_\pi|0\rangle_{oam} \xrightarrow{q-\text{plate}} \alpha|0\rangle_\text{L} + \beta|1\rangle_\text{L} = |\psi\rangle_\text{L}. \tag{3.6}$$

That is, the qubit is now encoded into the desired rotationally invariant space spanned by logical basis (3.4). Remarkably, the same q-plate device works also as a universal decoder, transferring generic rotationally invariant qubits to their polarization-encoded counterparts. Explicitly, by injecting $|\psi\rangle_{\mathrm{L}}$ into the q-plate, one obtains

$$|\psi\rangle_{\mathrm{L}} \overset{q-\mathrm{plate}}{\longrightarrow} (\alpha|R\rangle_\pi + \beta|L\rangle_\pi)|0\rangle_{oam} = |\psi\rangle_\pi|0\rangle_{oam}, \tag{3.7}$$

which can then be coupled into a single mode fiber and analyzed in polarization using standard methods. The measurement device is sketched in Fig. 3.2**b**. Notice that, again from the linearity of quantum mechanics, the encoding and decoding transformations (3.6) and (3.7) hold even if the polarization state is part of some larger entangled state. In addition, an outstanding feature of the q-plate is that it realizes the polarization-transverse-mode coupling in a single compact device that requires no interferometric stability, therefore providing the scheme with a built-in robustness. Finally, to perform arbitrary rotations of the reference frames of Alice and Bob, we developed an analysis stage which is able to rotate along light propagation axis. Hence we mounted the q-plate, waveplates, PBS, and optical fiber couplers in a compact and robust rotating detection stage Fig. 3.2**b**,**c**.

Our first step was to experimentally verify that the encoding/decoding apparatus works properly in the case of stationary aligned reference frames. We prepared the input photon in one of the polarization states $|H\rangle, |V\rangle, |R\rangle, |L\rangle$, or $|\pm\rangle = (|H\rangle \pm |V\rangle)/\sqrt{2}$. The qubit was then mapped by a first QP into the rotationally invariant encoding, transmitted through free space to the measurement stage, then decoded back to polarization by a second QP, and finally analyzed in polarization using a set of waveplates and a polarizing beam splitter (PBS). The average measured fidelity with the input states was $F = (98 \pm 1)\%$, indicating that the devices work near perfectly.

In order to prove that our logical encoding is really invariant under rotations we performed three different experiments: a feasibility-demonstration of BB84-key distribution protocol, distribution of entanglement, and violation of CHSH inequality.

3.3.1 Alignment-free quantum key distribution.

As a first test we demonstrated the feasibility of quantum key distribution in alignment-free settings by measuring the communication fidelity for different angles of the rotating analysis stage both by adopting hybrid encoding and, for comparison, polarization encoding. By using heralded single photons, and for different angles θ, we encoded, transmitted, and decoded, the four hybrid-qubit states required for the BB84 QKD protocol [29]: $|0\rangle_{\mathrm{L}}, |1\rangle_{\mathrm{L}}$, and $|\pm\rangle_{\mathrm{L}} = (|0\rangle_{\mathrm{L}} \pm |1\rangle_{\mathrm{L}})/\sqrt{2}$. We quantified the potential of our setup for QKD by measuring the fidelities of the states prepared as well as the qubit error rates (QBERs) [186] $\epsilon_{0_{\mathrm{L}}/1_{\mathrm{L}}}$ and $\epsilon_{+_{\mathrm{L}}/-_{\mathrm{L}}}$ for the logical bases $\{|0\rangle_{\mathrm{L}}, |1\rangle_{\mathrm{L}}\}$ and $\{|+\rangle_{\mathrm{L}}, |-\rangle_{\mathrm{L}}\}$, respectively. The experimental results are reported in Fig. 3.3**a,b**.

In particular, Figure 3.3**a** shows that the average fidelity F_{QKD} over the four states, as a function of θ is constantly above the value $F_{\mathrm{T}} = 89\%$ which corresponds to the well-known Shor-Preskill security proof threshold[187]. Above this, under the usual assumptions that Alice's source emits (logical) qubits, Bob's detectors perform (logical) qubit measurements, and there is no basis-dependent flaw in Alice's and Bob's systems[100], unconditional security can be guaranteed. In contrast, the fidelity attained using polarization-encoded qubits falls below the security bound for angles $\theta > 20°$, even in the ideal noiseless case (blue dashed line). Fig. 3.3**b** in turn shows the fidelity for each state, obtained by uniformly

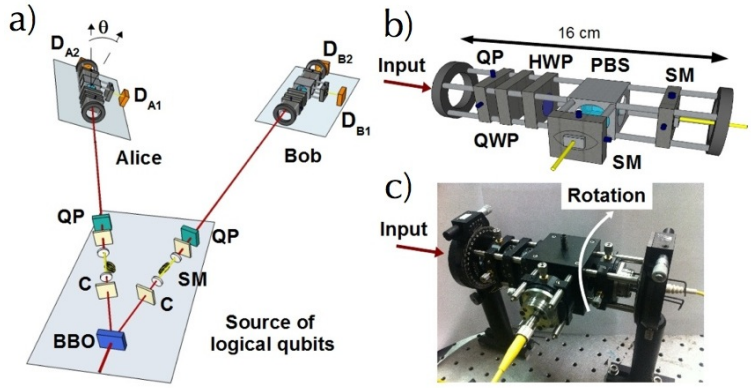

Figure 3.2. Toolbox for experimental alignment-free quantum communication. a) Experimental setup, in the configuration used to generate entangled rotationally invariant photon pairs and perform a misalignment-immune demonstration of non-locality. Reference-frame misalignments are implemented by physically rotating Alice's entire measurement station around the optical axis by an angle θ. For the alignment-free BB84 QKD test, the entangled-photon source together with Bob's measurement station is taken as the transmitting party, and Bob's photon is used to herald the transmission of the other photon to Alice. **b)** Schematics of the rotating device for measuring rotationally invariant qubits in arbitrary reference frames. **c)** Photo of the actual measurement device. Legend: QP - q-plate; BBO - β-barium borate crystal; C walk-off compensation crystals; SM - single-mode fibers; D - single photon detectors; HWP - half-wave plate; QWP - quarter-wave plate; PBS - polarizing beam-splitter.

mixing the data over all measured angles θ. Again, all the individual-state fidelities are consistently larger than the security threshold. Indeed, the measured QBERs, estimated as QBER $= 1 - F$, were $\epsilon_{0_L/1_L} = (0.65 \pm 0.09)\%$ and $\epsilon_{+_L/-_L} = (4.1 \pm 0.2)\%$, from which we expect a secret-key fraction $r = (70 \pm 1)\%$ [186].

3.3.2 Alignment-free entanglement distribution

As a second test we checked entanglement distribution between two parties with misaligned reference frames. We prepared a photon pair in the polarization entangled state

$$|\phi^-\rangle_\pi^{AB} = \frac{1}{\sqrt{2}}(|R\rangle_\pi^A|R\rangle_\pi^B - |L\rangle_\pi^A|L\rangle_\pi^B) \tag{3.8}$$

where the superscripts A and B refer to Alice's and Bob's photons, respectively. Then, following the experimental scheme in Fig. 3.2, the photons were coupled into single mode fibers and sent through a q-plate at the output of each fiber in order to transforms the polarization-entangled state to the rotationally invariant entangled state:

$$|\phi^-\rangle_\pi^{AB} \overset{q-\text{plates}}{\longrightarrow} \tfrac{1}{\sqrt{2}}(|0\rangle_L^A|0\rangle_L^B - |1\rangle_L^A|1\rangle_L^B) = |\phi^-\rangle_L^{AB}. \tag{3.9}$$

We then performed quantum state tomography of the experimental density matrix ρ_L^{AB} measured without misalignment ($\theta = 0$).The real part of the tomographically reconstructed matrix, in the basis $\{|0\rangle_L^A|0\rangle_L^B,\ |0\rangle_L^A|1\rangle_L^B,\ |1\rangle_L^A|0\rangle_L^B,\ |1\rangle_L^A|1\rangle_L^B\}$, is shown in Fig. 3.4**a**. The fidelity with the experimental polarization entangled state ρ_π^{AB} input to the encoder is $F_0(\rho_L^{AB}, \rho_\pi^{AB}) = (93 \pm 1)\%$, while the entanglement of ρ_L^{AB}, as given by the concurrence, is $C = (0.85 \pm 0.03)$. In order to verify the rotational invariance of the state produced,

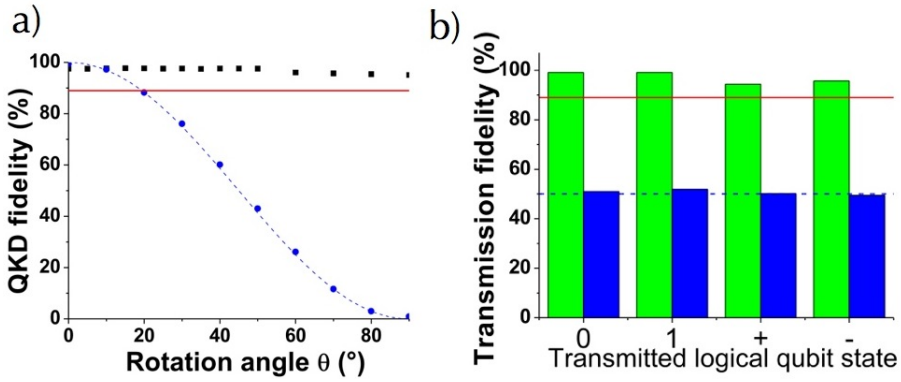

Figure 3.3. Experimental results of alignment-free quantum communication tests. Measured fidelity of qubits encoded in the rotationally invariant polarization-OAM space, in a test of the BB84 quantum key distribution protocol, compared to that of standard polarization-encoded qubits. Panel (a) shows the fidelity F_{QKD} (black square dots) averaged over the four hybrid qubit states used in the protocol, as a function of the misalignment angle θ between the transmission and detection reference frames. Panel (b) shows the individual fidelity of each of the four states (green bars) observed over the whole QC session including all the different rotation angles probed. The latter accounts for the general situation where the misalignment could vary randomly between transmitted photons. In both panels, the blue dots/bars and dashed lines give respectively the measured and theoretically-calculated fidelity for the standard case of polarization encoding. The red line delineates the QKD security threshold. In all data points, the error bars resulting from Poissonian statistics are smaller than the symbols.

we repeated the tomographic reconstruction with Alice's measurement stage rotated by $\theta = 45°$. The corresponding reconstruction is shown in Fig. 3.4**b**. The fidelity with ρ_{π}^{AB} is $F_{45}(\rho_{\mathrm{L}}^{AB}, \rho_{\pi}^{AB}) = (96 \pm 1)\%$, and the concurrence is $C = (0.84 \pm 0.03)$, consistent with the case $\theta = 0$. This indicates that our entanglement distribution scheme is immune to relative misalignments of Alice and Bob.

3.3.3 Alignment-free quantum non-locality

Once verified entanglement distribution, the next step has been to perform a non-locality test with hybrid rotational invariant qubits. Hence we verified a violation of the CHSH inequality $S = |E(a_0, b_0) + E(a_1, b_0) + E(a_0, b_1) - E(a_1, b_1)| \leq 2$ in an alignment-free setting. Where a_x and b_y, with possible values 0 or 1, are the outcomes of Alice's and Bob's measurement settings x and y, respectively, with x and y equal to 0 or 1. and correlators $E(a_x, b_y) = \langle (-1)^{a_x + b_y} \rangle$, with $\langle\rangle$ the statistical average, quantify the fraction of events where Alice's and Bob's outcomes are observed to coincide. For the rotationally invariant quantum violation of the inequality we chose the following hybrid measurement bases: $\{|0\rangle_{\mathrm{L}}, |1\rangle_{\mathrm{L}}\}$ and $\{|+\rangle_{\mathrm{L}}, |-\rangle_{\mathrm{L}}\}$, corresponding to Alice's settings $x = 0$ and $x = 1$, respectively, and $\{\cos\frac{\pi}{8}|0\rangle_{\mathrm{L}} + \sin\frac{\pi}{8}|1\rangle_{\mathrm{L}},\ -\sin\frac{\pi}{8}|0\rangle_{\mathrm{L}} + \cos\frac{\pi}{8}|1\rangle_{\mathrm{L}}\}$ and $\{\sin\frac{\pi}{8}|0\rangle_{\mathrm{L}} + \cos\frac{\pi}{8}|1\rangle_{\mathrm{L}},\ -\cos\frac{\pi}{8}|0\rangle_{\mathrm{L}} + \sin\frac{\pi}{8}|1\rangle_{\mathrm{L}}\}$, corresponding to Bob's settings $y = 0$ and $y = 1$, respectively. Fig. 3.4**c** reports the measured CHSH parameter S versus the rotation angle θ of Alice's measurement frame. The figure shows that the local-hidden-variable bound is violated for all angles, in striking contrast with the experimental polarization state ρ_{π}^{AB} (blue circles), or even with the ideal maximally-entangled polarization state $|\phi^-\rangle_{\pi}^{AB}$ (blue dashed line). For the logically-encoded states, we mixed the data of all different values of θ to test the violation's immunity to

arbitrarily-varying frame orientation, obtaining a value of $S = (2.47 \pm 0.01) > 2$.

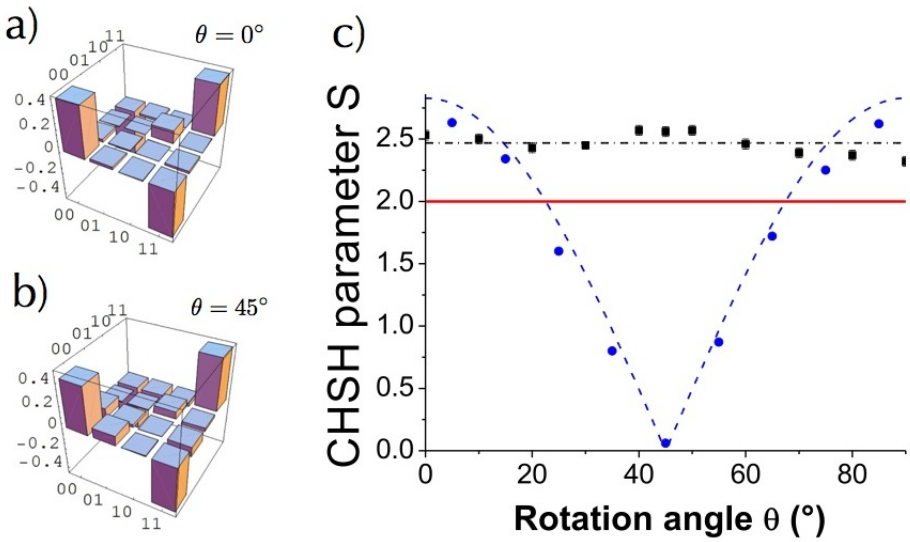

Figure 3.4. Experimental results of alignment-free quantum communication tests. **a-b)** Quantum state tomography of the entangled state of hybrid qubits distributed between Alice and Bob, for the case of aligned reference frames (a) and for a misalignment of $\theta = 45°$ (b). In both cases, only the real part of the density matrices is shown, as the imaginary part is negligible. **c)** CHSH parameter S (black squares) in experimental non-locality tests on photon pairs entangled in the rotationally invariant qubit space, as a function of the relative misalignment θ between Alice's and Bob's frames. The red line is the local-hidden-variable bound. The blue dots represent the measured values of S for the bare polarization-entangled states without the logical protection. Whereas the blue dashed line is the theoretically-calculated maximal CHSH parameter that would be obtained with pure maximally-entangled polarization states. The black dot-dashed line in turn represents the overall CHSH value S of the entire test taking into account all the experimental runs with different θ. In all data points, the error bars resulting from Poissonian statistics are smaller than the symbols.

3.4 Robustness of rotational-invariant hybrid qubits.

All the previous results demonstrate a way to overcome the need of a shared reference frame for quantum communication. However, any realistic long-distance communication scenario has to take into account also perturbations in the communication channel which can be introduced by an obstacle along the way or by atmospheric turbulences.

A remarkable feature of our polarization-OAM hybrid-encoding QC scheme is that it turns out to be robust against the spatial-mode perturbations arising in beam misalignments around axes other than the optical one and atmospheric turbulence effects. Such robustness appears at first glance counterintuitive, since the encoding involves the use of orbital angular momentum, which is quite sensitive to all the above-mentioned spatial perturbations[162, 94] (although significant progresses in pure OAM-based classical and quantum communication through the atmosphere have been recently reported[75, 216, 174]). The main reason of such robustness is that the OAM spread induced by spatial-mode perturbations is neutralized by the polarization degree of freedom, which is in contrast very robust against those spatial-mode perturbations. This allows one to filter out, in the receiving unit, most components of

the state that would otherwise decrease the fidelities. That is, the particular decoding setup used intrinsically implements an effective quantum error-correction procedure that discards (but does not correct) all states outside the logical subspace.

Indeed, spatial-mode perturbations will alter a generic hybrid qubit $\alpha|R\rangle_\pi|l\rangle_{oam}+\beta|L\rangle_\pi|r\rangle_{oam}$, transforming it into the following state:

$$\sum_m [C_{+1,m}\alpha|R\rangle_\pi|m\rangle_{oam} + C_{-1,m}\beta|L\rangle_\pi|m\rangle_{oam}], \tag{3.10}$$

where $|m\rangle_{oam}$ is a generic OAM eigenstate and $C_{m,m'}$ are the probability amplitudes for the photon OAM to be shifted from $m\hbar$ to $m'\hbar$, due to the perturbation. However, in the decoding unit, the photon undergoes another q-plate transformation

$$\overset{q-\text{plate}}{\longrightarrow} \sum_m [C_{+1,m}\alpha|L\rangle_\pi|m-1\rangle_{oam} + C_{-1,m}\beta|R\rangle_\pi|m+1\rangle_{oam}], \tag{3.11}$$

followed by a projection onto an $m = 0$ Gaussian spatial mode (e.g., by coupling it into a single-mode fiber), which leads to the following final state:

$$[C_{+1,+1}\alpha|L\rangle_\pi + C_{-1,-1}\beta|R\rangle_\pi]|0\rangle_{oam}. \tag{3.12}$$

Therefore, if the spatial-mode perturbation satisfies the condition

$$C_{+1,+1} = C_{-1,-1}, \tag{3.13}$$

the final polarization-encoded qubit will be identical to the initial one, except for a global phase and amplitude, and the communication fidelity will be preserved.

In particular, every beam transformation that is mirror-symmetric with respect to a plane containing the initial beam axis will be symmetrical in the sign of OAM and hence will satisfy Eq. (3.13). For example, beam parallel displacements, tilts, elliptical deformations, or aperturings with a circular iris (even if off center) or a half-plane mask (knife-edge), all have this symmetry. An axial misalignment, i.e. a misalignment around an axis other than the optical one, between the transmitting and receiving communication units is equivalent to a beam translation and/or tilt, with both contained in the same plane, and can be treated analogously. Only symmetry-breaking combinations of two or more of the above effects may affect the fidelity. For example, a beam tilt combined with a beam displacement along a different plane will break the mirror symmetry and hence might introduce some degree of qubit alteration. Also, the main optical effects arising from atmospheric turbulence, such as beam wandering and spreading are mirror-symmetric, so that the extent of qubit alteration is expected to be much less significant in our communication scheme than in the case of pure OAM communication.

Another important class of transformations which satisfies Eq. (3.13) is that mathematically defined by pure multiplicative factors acting on the optical field, e.g. the transformations arising from crossing any arbitrary inhomogeneous medium that is thin as compared with the Rayleigh length. It is easy to verify that these will be described by coefficients $C_{m,m'}$ which depend on the difference $m - m'$ and on the absolute values $|m|$ and $|m'|$, so that Eq. (3.13) is automatically satisfied. Weak turbulence, introducing only pure phase wavefront distortions, falls within this class of transformations and is therefore predicted to leave the qubit fidelity intact[162]. If we now consider the fact that light propagation in homogeneous media leaves the various OAM components constant, we conclude that Eq. (3.13) is satisfied even if the turbulent medium is followed and/or preceded by a long-distance free-space propagation, as in the case of earth to satellite (and vice versa) communication through the atmosphere.

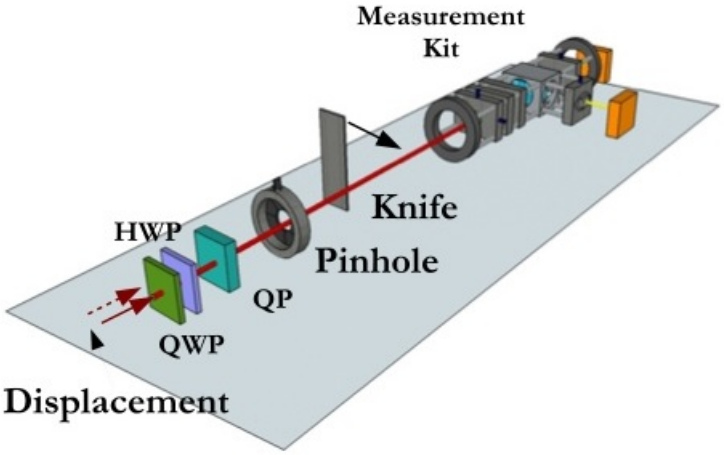

Figure 3.5. Experimental setup adopted for the tests on the resistance of the rotational invariant hybrid photonic qubits to spatial-mode perturbations. In the schematics, we reported both the circular aperture (pinhole) and the half-plane obstruction (a movable knife-edge) that can alter the transmission of the qubits. Displaced beam is represented by a dashed red arrow.

3.4.1 Experimental tests of rotational-invariant qubit robustness.

As a first test of hybrid qubits robustness, we considered transmission through two types of transverse apertures: a half-plane movable obstruction (knife) covering a variable fraction of the transverse mode, and an iris (or pinhole) with variable radius. We have measured the state transmission fidelity F for different input states, at both aligned and 45°-rotated measurement stages, with respect to the transmitting unit, and for an increasing disturbance due to the obstruction. The experimental setup used for this test is illustrated in Fig. 3.5.

We encoded different polarization qubits using two waveplates and mapped them into the hybrid encoding using a q-plate. For the purpose of comparison, we also switched to a pure-OAM encoding by inserting a fixed linear polarizer after the q-plate, so as to erase the polarization content of the qubit. Then the photon was sent through the obstruction and to the receiving unit, and the communication fidelity was measured as a function of the obstuction transmittance, by varying the aperture of the pinhole or the transverse position of the knife. Thus, the lowest transmittivity corresponds to a tiny aperture of the pinhole (0.2 times the beam size), or to the almost complete coverage of the beam. All reported experimental fidelities were obtained by averaging over the six eigenstates of three mutually unbiased bases, therefore providing a good representative of the average fidelity over any input qubit state. The experimental results are reported in Fig. 3.6.

It is seen that the average fidelity of hybrid qubits is independent both of the transmittivity of the aperture and of the rotation angle of the measurement kit, with a global average of $F = (98 \pm 1)\%$ for the case of iris and $F = (96 \pm 1)\%$ for the knife. Moreover, in the former case the fidelity is not affected by the displacement of the pinhole off the beam axis. For comparison, we tested the resistance of qubits encoded only in the two-dimensional OAM subspace $o_1 = \{|+1\rangle, |-1\rangle\}$, i.e., the same subspace used for the hybrid encoding. In this case, the fidelity remains high ($F = (97 \pm 1)\%$) only when the cylindrical symmetry of the modes is not perturbed, as for the centered iris, while for all other cases (non-centered iris or

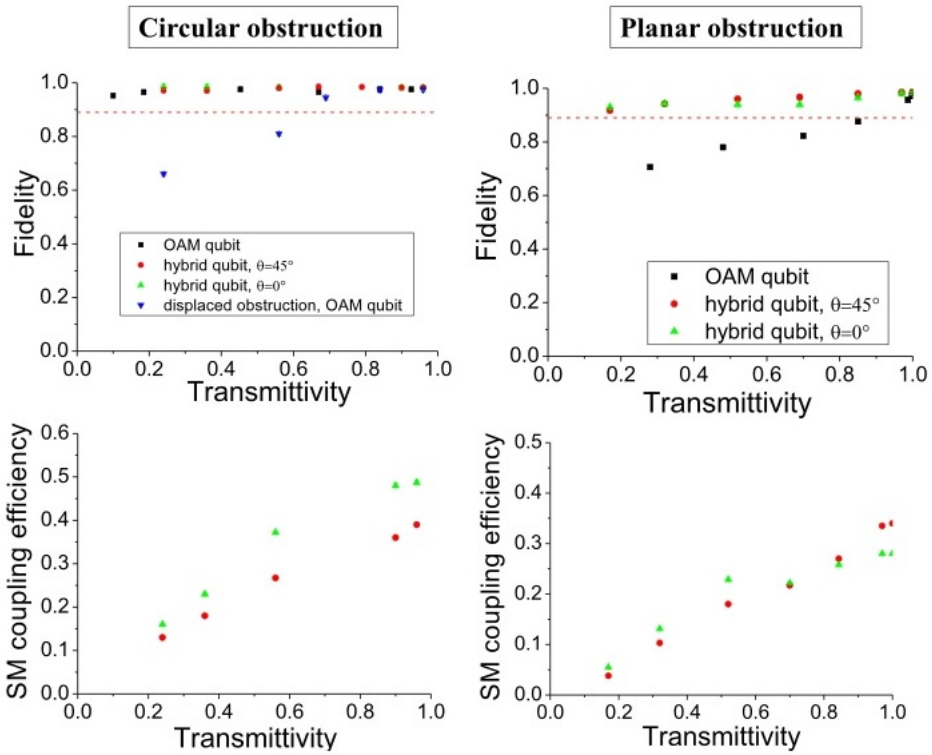

Figure 3.6. Experimental data showing the resistance of rotational invariant hybrid qubits to beam perturbations, compared with the case of pure OAM qubits. Left panel refers to the case of circular aperture. Average fidelity of pure OAM qubits (black squares), hybrid qubits for a measurement stage rotated at an angle $\theta = 0°$ (green triangle) and at an angle $\theta = 45°$ (red circles) with respect to the transmitting unit. The blue triangles refer to the pure OAM qubits case, when the circular aperture is displaced off the beam axis by 5% of the beam waist (the hybrid qubit behavior in the latter case was essentially indistinguishable from the centered aperture case). The transmission efficiency is determined by single-mode (SM) fiber-coupling efficiency after a circular aperture of varying radius, in the case of hybrid qubits only. Right panel refers to half-plane aperture. Average fidelities for hybrid qubits at $\theta = 0°$ (green triangle) and $\theta = 45°$ (red circles). Black squares are the corresponding results for pure OAM qubits. The transmission efficiency is determined by single-mode (SM) fiber-coupling efficiency after a movable half-plane aperture.

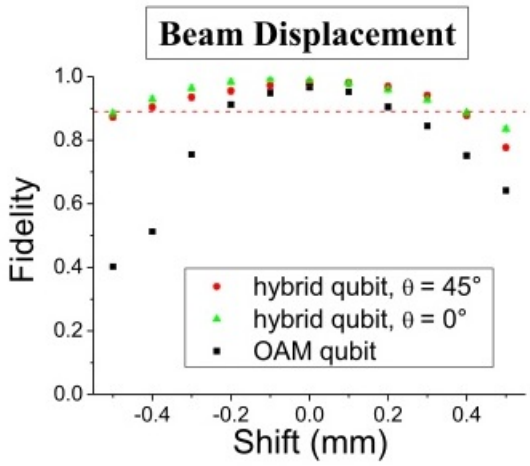

Figure 3.7. Experimental data showing the resistance of hybrid qubits to a beam displacement, compared to the case of pure OAM encoding. The beam waist in our experiment is $w_0 = (1.0 \pm 0.1)$mm.

knife) the fidelity drops rapidly with decreasing transmission.

As a second test, we performed a communication run while changing the angle of the measurement kit without reoptimizing the alignment of the single mode fiber. This corresponds to introducing small uncontrolled tilt and displacements in the beam during the measurement. We found that the system preserves a good quantum communication fidelity (i.e. above the security threshold) for rotations up to 30°. Above this angle it was necessary to slightly readjust the single-mode fiber alignment in order to restore a high fidelity.

Finally, we tested the communication fidelity dependence on a controlled beam displacement, for two fixed angles of the measurement stage. Fig. 3.7 shows the behavior of the average communication fidelity as a function of the beam displacement. The hybrid-qubit fidelity decreases with the displacement, but much slower than that of pure OAM encoding

Conclusions and Perspectives

In this chapter we have shown how to exploit high dimensional quantum systems to overcome the lack of a shared reference frame in quantum communication. Indeed uncontrolled reference-frame misalignments limit quantum communication, as they turn the transmitted quantum messages into noisy, classical ones. We reported the development of a robust and compact toolbox for the efficient encoding and decoding of quantum information into single-photon states that are invariant under arbitrary rotations around the optical axis. Such states belong to a decoherence free subspace of a four dimensional hybrid system. In order to prove the feasibility of rotational invariant quantum communication we performed a cryptographic key distribution protocol, distribution of entanglement and the violation of a Bell inequality, all in alignment-free settings. Our rotational invariant qubits turns out to be also robust against misalignments around other directions than propagation axis, atmospheric turbulences and partial obstructions. This is due to a filtering mechanism intrinsic to our universal-decoder set-up, which maps errors originating from beam rotations around axes other than the optical link, as well as other spatial perturbations, into signal losses instead

of infidelity. Such preliminary result is the first step of a deeper study on resilience to turbulences for hybrid qubits which could be an interesting near future research topic since these features make the misalignment-free scheme here presented a possible resource for long distance satellite quantum communication.

Chapter 4

Photonic polarization gears for ultra-sensitive angular measurements

Following the concept underlying the working principle of rotationa invariant qubits, we investigated the properties of a particular subset of hybrid (polarization-OAM) ququart states and their application in metrology. In this chapter, we demonstrate NOON-like photonic states of m quanta of angular momentum, with m as high as 100, in a setup that acts as a "photonic gear", converting, for each photon, a mechanical rotation of angle θ into an amplified rotation of the optical polarization by the angle $m\theta$. When seen through polarizers, this leads to a "super-resolving" Malus' law, exhibiting $2m$ fringes per turn, instead of the usual two. Exploiting this effect, we demonstrate single-photon angular measurements with the same precision as that of the polarization-only quantum strategies with m photons, but robust to photon losses. Indeed, in this regime every photon is disentangled from all others and hence the loss of a photon does not affect the overall phase coherence, making the scheme loss-robust. Moreover, the experimental state production and detection are exponentially more efficient than for N-photon entangled states.

Although quantum-inspired, our approach is essentially classical, because the enhancement does not come from quantum entanglement but results instead from the rotational sensitivity of large angular momentum eigenmodes. In fact, our photonic gears can operate also in the fully classical regime, as described by coherent states. However the photonic gear is compatible with quantum strategies as we show in the last section of the chapter where we combine the gear rotational enhancement with the quantum correlation effects of entangled photons, thus exploiting the advantages of both approaches. The high "gear ratio" m translates into a similarly high sensitivity enhancement of optical non-contact angular measurements, boosting the current state-of-the-art by almost two orders of magnitude.

These results have been published in [V. D'Ambrosio, N. Spagnolo, L. Del Re, S. Slussarenko, Y. Li, L. C. Kwek, L. Marrucci, S. P. Walborn, L. Aolita and F. Sciarrino, *Photonic polarization gears for ultra-sensitive angular measurements*, Nature Communications 4, 2432 (2013)].

4.1 Photonic gear concept

The key element of our photonic gears are hybrid photon qubits obtained as subspace of the ququart space spanned by vectors $\{|L,l\rangle, |L,-l\rangle, |R,l\rangle, |R,-l\rangle\}$. As we know, for a linearly polarized input, the photonic states generated by a q-plate are superpositions of $m = 2q \pm 1$ quanta in opposite total angular momentum eigenmodes. Although previous achievements were limited to q-plates with low q (up to 3) [189]. The work here presented acted as a prompt to produce new family of devices with q ranging up to 50, producing angular momentum values as large as $m = 101$. These photonic states can be also classically visualized as space-variant polarization states [56]. When these SAM-OAM superposition states are passed through a second q-plate, they are converted back into pure polarization states with zero OAM and a uniform polarization. However, a relative rotation of the transmitting and reading stages by a given angle θ is converted into a rotation of the light optical polarization by the angle $m\theta$, which in our case can be as high as 101θ. It is this "gear ratio" m that gives rise to the angular sensitivity enhancement.

In the following, we will describe the photonic gears concept by adopting a quantum language, with the purpose of comparing our sensitivity enhancement with the shot-noise and Heisenberg limits and to allow an easier generalization to the case in which there is both a classical and a quantum effect. Let us then consider the scenario where a sender Alice and a receiver Bob wish to measure a relative misalignment angle θ between their reference frames around the optical axis (see Fig. 4.1).

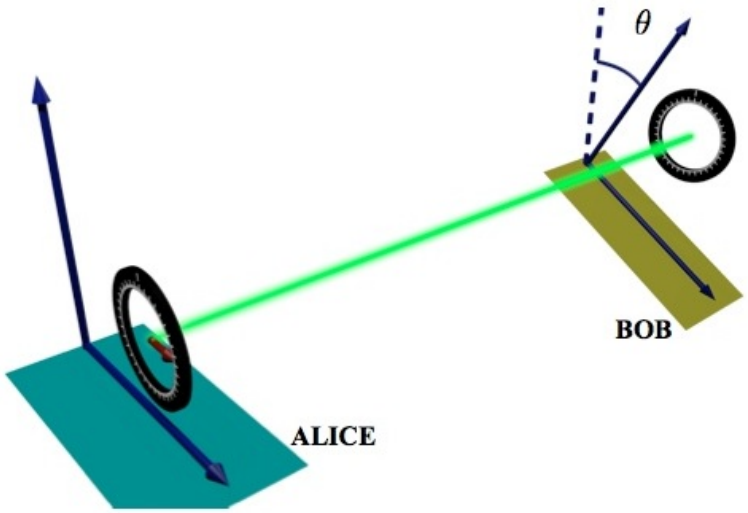

Figure 4.1. The measurement scenario A sender Alice prepares and sends to a receiver Bob photonic probes to measure the relative angle θ between their reference frames.

A classical strategy for this task consists of Alice sending N photons (see Fig. 4.2 (a)), each one in state $|\Psi^{\mathrm{C}}\rangle \doteq |1\rangle_H \equiv \frac{1}{\sqrt{2}}(|1\rangle_R + |1\rangle_L)$, where $|n\rangle_x$ denotes a state of n photons in mode x, with $x = H$, R, or L, representing, as usual, photon polarization modes and all modes in the vacuum state are omitted for brevity. Bob fixes a polarizer in the H direction in his coordinate system, where the misalignment corresponds to a rotation by $-\theta$ of the photons' state. In turn, the L and R polarization states are eigenstates of rotation, so that in Bob's frame $|\Psi^{\mathrm{C}}\rangle$ becomes $|\Psi^{\mathrm{C}}(\theta)\rangle = \frac{1}{\sqrt{2}}(e^{i\theta}|1\rangle_R + e^{-i\theta}|1\rangle_L)$. The conditional probability

that he detects a photon in the H-polarization (of his reference frame) given that the phase is θ is given by Malus' law: $p^{\mathrm{C}}(H|\theta) = \cos^2\theta$. By measuring this probability, Alice and Bob can estimate θ. To strengthen their statistics, they repeat the procedure ν times, consuming a total of $\nu \times N$ photons, and average all the outcomes. Their final statistical error is bounded as

$$\Delta\theta^{\mathrm{C}} \geq \left[2\sqrt{\nu N}\right]^{-1}. \tag{4.1}$$

The right-hand side is the standard quantum limit, and can always be reached in the asymptotic limit of large νN [93]. Our error estimators $\Delta\theta$ are standard root-mean-squared variances. In general, for phases, a cyclic error cost-function would be more appropriate, as for instance the Holevo variance [107]. However, both types of variances coincide in the small-error limit, so for our purposes the standard variance is adequate.

Using quantum resources, the optimal strategy consists of Alice sending ν probes, each one composed of the N-photon entangled NOON state $|\Psi^{\mathrm{Q}}\rangle = \frac{1}{\sqrt{2}}(|N\rangle_R + |N\rangle_L)$. In Bob's frame, this state is expressed as $|\Psi^{\mathrm{Q}}(\theta)\rangle = \frac{1}{\sqrt{2}}(e^{iN\theta}|N\rangle_R + e^{-iN\theta}|N\rangle_L)$. The conditional probability that he detects the unrotated state $|\Psi^{\mathrm{Q}}\rangle$ is $p^{\mathrm{Q}}(\Psi^{\mathrm{Q}}|\theta) \doteq |\langle\Psi^{\mathrm{Q}}||\Psi^{\mathrm{Q}}(\theta)\rangle|^2 = \cos^2(N\theta)$, which resolves values of θ that are N times smaller than $p^{\mathrm{C}}(H|\theta)$. Their uncertainty is then bounded as

$$\Delta\theta^{\mathrm{Q}} \geq \left[2\sqrt{\nu N}\right]^{-1}. \tag{4.2}$$

The right-hand side is now the Heisenberg limit, which can always be reached in the asymptotic limit of large ν [93].

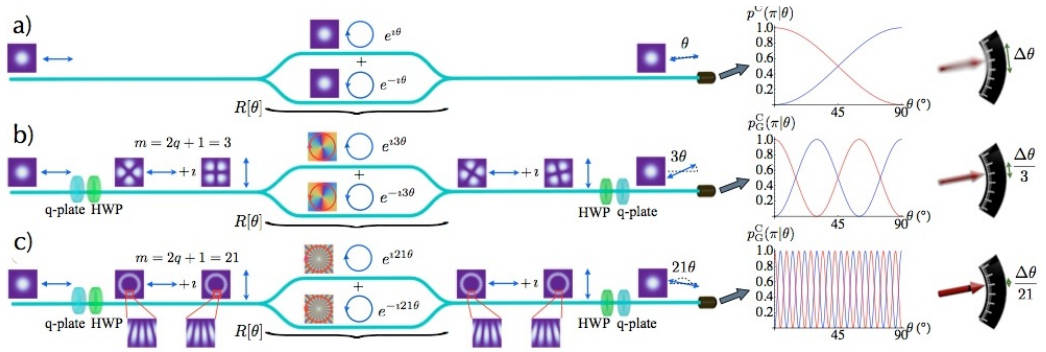

Figure 4.2. Photonic gear concept. Equivalent interferometric scheme to the measurement scenario of Figure 4.1. The action of the physical rotation can be schematically represented as an interferometer, where the two arms correspond to the right- and left-circular components of the photon. (a) Polarization-only states are used. The physical rotation introduces a relative phase between the right- and left-circular components of the photon, corresponding to a rotation of the final photon polarization by the same angle θ. The measurement is repeated ν times, and polarization fringes $p^{\mathrm{C}}(\pi|\theta) = \cos^2\theta$ are recorded (with $\pi = H, V$), from which the angle θ is retrieved with a statistical error $\Delta\theta$ (represented as a blurred arrow pointing to a goniometer). (b-c) Hybrid SAM-OAM photon states are generated by exploiting q-plates [(b) $q = 1$, (c) $q = 10$] and are used to estimate the angle θ. The physical rotation introduces a relative phase between the two components which varies $m = 2q + 1$ times faster than the polarization-only case, so that the output photon polarization rotates m times faster (photonic gear effect). The recorded polarization fringes $p^{\mathrm{C}}_{\mathrm{G}}(\pi|\theta)$ after decoding with a second q-plate now present a periodicity $\propto 1/m$, leading to an improved angular sensitivity $\Delta\theta/m$. The intensity (squared blue contour plots) and phase patterns (squared contour plots in false colors) of the linear and circular polarization components of the employed SAM-OAM states are also shown.

In our photonic gear approach, Alice and Bob exchange photons in SAM-OAM superposition states [see Fig. 4.2 (b-c)]. Alice initially prepares N horizontally-polarized photons,

as in the classical strategy. However, before sending them to Bob, she first has them pass through a q-plate of charge q. The q-plate implements the bidirectional (unitary) mode transformations $\{a^\dagger_{R,0} \leftrightarrow a^\dagger_{L,-2q}, a^\dagger_{L,0} \leftrightarrow a^\dagger_{R,2q}\}$, where the subscripts 0 and $\pm 2q$ refer to the OAM values, and $a^\dagger_{\pi,l}$ denotes the creation operator of a photon with polarization π and OAM component l [151]. This results in the following transformation of Alice's photons: $|1\rangle_{H,0} \overset{q-\text{plate}}{\longrightarrow} \frac{1}{\sqrt{2}}(|1\rangle_{L,-2q} + |1\rangle_{R,2q})$. Next, a half-wave plate (HWP) is used to invert the polarization, to obtain the transmitted states

$$|\Psi^{\mathrm{C}}_{\mathrm{G}}\rangle = \frac{1}{\sqrt{2}}(|1\rangle_{R,-2q} + |1\rangle_{L,2q}). \tag{4.3}$$

This single-photon state represents a superposition of $m = 2q + 1$ quanta in opposite total (spin + orbital) angular momentum eigenmodes. Likewise, if the HWP is removed, the case $m = 2q - 1$ is obtained.

In Bob's frame, the photons arrive as $|\Psi^{\mathrm{C}}_{\mathrm{G}}(\theta)\rangle = \frac{1}{\sqrt{2}}(e^{im\theta}|1\rangle_{R,-2q} + e^{-im\theta}|1\rangle_{L,2q})$. To detect them, he first undoes Alice's polarization flip with another HWP, and undoes her OAM encoding with another q-plate of the same charge q, so that

$$|\Psi^{\mathrm{C}}_{\mathrm{G}}(\theta)\rangle \longrightarrow \frac{1}{\sqrt{2}}(e^{im\theta}|1\rangle_{R,0} + e^{-im\theta}|1\rangle_{L,0}). \tag{4.4}$$

This state corresponds to a uniform linear polarization, but with the polarization direction forming an angle $m\theta$ with respect to Bob's H axis, resulting in the photonic gear effect. Finally, Bob measures the probability of detecting the H linear polarization conditioned on θ as in the classical strategy. This is again given by Malus' law:

$$p^{\mathrm{C}}_{\mathrm{G}}(H|\theta) = \cos^2(m\theta), \tag{4.5}$$

but shows now the m-fold resolution enhancement over the polarization-only strategy.

As usual, Alice and Bob repeat the procedure a total of ν times. Their statistical error is now bounded as

$$\Delta\theta^{\mathrm{C}}_{\mathrm{G}} \geq \left[2m\sqrt{\nu N}\right]^{-1}, \tag{4.6}$$

and can always saturate the bound in the asymptotic limit of large νN. This represents an improvement over the standard limit (4.1) for polarization-only strategies by a factor of m. This enhancement is not quantum but due exclusively to the coherent rotational sensitivity of high-order angular momentum eigenmodes (for more details see Appendix A).

Remarkably, already for $m > \sqrt{N}$ the scaling (4.6) becomes better than the best precision (4.2) attainable with polarization-only NOON states. Furthermore, the photonic-gear strategies, both in the single-photon and classical regimes, greatly outperform the latter in realistic scenarios with large N. First, the production and detection of our SAM-OAM photon states is exponentially more efficient in N than those of NOON states. Second, since state (4.3) does not bear any multi-photon coherences, losses reduce the total number of photons, but leave the remaining ones unaltered. That is, total losses characterized by an overall transmissivity $0 \leq \eta \leq 1$ enter as a constant multiplicative factor, simply rescaling in (4.6) the total number of photons to $\nu N\eta$, in striking contrast to NOON states [76]. Furthermore, one could also consider to exploit the orbital angular momentum of light to mimic the behaviour of other quantum states such us spin-squeezed state, requiring the superposition of many angular-momentum eigenstates.

The last type of strategy we consider is a hybrid classical-quantum one, which exploits both entanglement and high angular momenta through the photonic gear. In its simplest version, each probe may consist of an N-photon entangled NOON state $|\Psi_{\rm G}^{\rm Q}\rangle = \frac{1}{\sqrt{2}}(|N\rangle_{R,-2q} + |N\rangle_{L,2q})$. Following the same steps as above, one finds this time that $p_{\rm G}^{\rm Q}(\Psi_{\rm G}^{\rm Q}|\theta) \doteq |\langle\Psi_{\rm G}^{\rm Q}||\Psi_{\rm G}^{\rm Q}(\theta)\rangle|^2 = \cos^2(mN\theta)$ and

$$\Delta\theta_{\rm G}^{\rm Q} \geq \left[2m\sqrt{\nu}N\right]^{-1}. \tag{4.7}$$

Thus, ideally, this strategy features the Heisenberg precision scaling for hybrid SAM-OAM approaches, but it bears in practice the same loss-sensitivity problems as the polarization-only quantum strategy. However, for small N, these problems can still be efficiently dealt with and interesting applications can be achieved, as we demonstrate below.

Moreover, multi-photon quantum states other than NOON states can also be combined with the photonic gears, obtaining other interesting effects. For example, let us consider two-photon polarization-entangled states, where one photon is sent to Alice and the other to Bob. Alice and Bob make local H/V-polarization analysis in their own rotating stages, which can be set at arbitrary angles $\theta_{\rm A}$ and $\theta_{\rm B}$. When $\theta_{\rm A} = \theta_{\rm B} = \theta$ the system can model two photons travelling in the same mode, subject to the same rotation, and hence yield results analogous to the NOON-state case discussed above for $N = 2$.

When $\theta_{\rm A} \neq \theta_{\rm B}$ one can instead align two distant frames remotely with two-photon probes produced by an unrelated common source, which sends one photon to each frame, by exploiting the quantum correlations among the two photons. More in detail, let us assume that the photons are generated in the maximally entangled polarization Bell state $|\psi^-\rangle = \frac{1}{\sqrt{2}}(|1\rangle_{R,0}^{\rm A}|1\rangle_{L,0}^{\rm B} - |1\rangle_{L,0}^{\rm A}|1\rangle_{R,0}^{\rm B})$. The photons, before transmission, are sent through two q-plates with topological charges $q_{\rm A}$ and $q_{\rm B}$, respectively, and a HWP, as shown in Fig. 4.7. Thus, the following state is distributed to Alice and Bob:

$$|\psi_{\rm G}^-\rangle = \frac{1}{\sqrt{2}}(|1\rangle_{R,-2q_{\rm A}}^{\rm A}|1\rangle_{L,2q_{\rm B}}^{\rm B} - |1\rangle_{L,2q_{\rm A}}^{\rm A}|1\rangle_{R,-2q_{\rm B}}^{\rm B}). \tag{4.8}$$

Alice and Bob, in their rotated frames, apply the same transformations to the photons, thus converting them back to pure polarization states. The probability that Alice and Bob both detect H-polarized photons in their local frames is then $p_{\rm G}^{\psi^-}(HH|\theta_{\rm A}\theta_{\rm B}) = \frac{1}{2}\sin^2[(2q_{\rm A} + 1)\theta_{\rm A} - (2q_{\rm B} + 1)\theta_{\rm B}]$, showing "amplified" polarization correlations. Choosing $q_{\rm A} = q_{\rm B}$, one can for example use these correlations (in combination with classical communication channels) to precisely estimate the relative misalignment $\theta_{\rm A} - \theta_{\rm B}$ and remotely align the two distant frames. If a HWP with the optical axis parallel to H is now inserted in Bob's photon path after generation of the polarization-entangled state (which corresponds to acting with a σ_x Pauli operator in the R/L basis), one obtains the entangled state $|\phi_{\rm G}^-\rangle = \frac{1}{\sqrt{2}}(|1\rangle_{L,2q_{\rm A}}^{\rm A}|1\rangle_{L,2q_{\rm B}}^{\rm B} - |1\rangle_{R,-2q_{\rm A}}^{\rm A}|1\rangle_{R,-2q_{\rm B}}^{\rm B})$, instead of $|\psi_{\rm G}^-\rangle$. Alice's and Bob's HH-photon correlations have now probability $p_{\rm G}^{\phi^-}(HH|\theta_{\rm A}\theta_{\rm B}) = \frac{1}{2}\sin^2[(2q_{\rm A} + 1)\theta_{\rm A} + (2q_{\rm B} + 1)\theta_{\rm B}]$. So, in this case, for $\theta_{\rm A} = \theta_{\rm B} = \theta$, the system is metrologically equivalent to NOON state probes $|\Psi_{\rm G}^{\rm Q}\rangle$ for $N = 2$ and $m = \frac{m_{\rm A}+m_{\rm B}}{2} = q_{\rm A} + q_{\rm B} + 1$. In particular, for $N = 2$ photons, θ can be estimated from the HH-correlation measurements with just half the efficiency as from $p_{\rm G}^{\rm Q}(\Psi_{\rm G}^{\rm Q}|\theta)$, which would require two-photon interference detection. Full efficiency in the estimation process can be recovered by simply registering and considering the four possible two-photon polarization-correlations (HH, HV, VH, VV), which requires no extra measurements. The same result can be generalized to N-photon entangled states.

4.2 Experimental results

Our theoretical predictions were experimentally tested by exploiting a series of q-plates with increasing charge q. We focus first on the single-photon regime. The experimental setup is shown in Fig. 4.3.

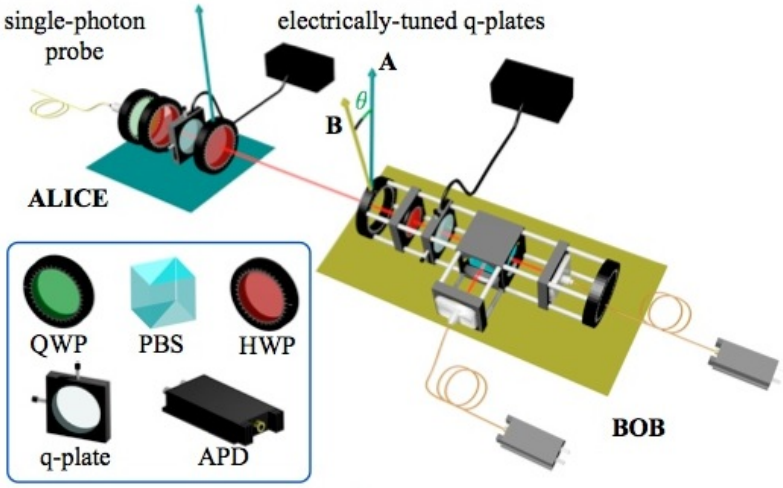

Figure 4.3. Experimental setup In the single-photon regime, Alice uses photons generated by a parametric down-conversion heralded source. In the classical regime, Alice uses coherent laser pulses. The quantum regime, in turn, uses entangled photons and is described in Fig. 4.7. Bob's detection apparatus is mounted in a compact and robust stage which can be freely rotated around the light propagation axis [70]. Legend: QWP - quarter-wave plate, HWP - half-wave plate, PBS - polarizing beam-splitter, APD - fiber-coupled single-photon detector.

Figures 4.4 shows the polarization fringes obtained for several values of q, corresponding to the "super-resolving" Malus' law (4.5). The red curves correspond to the polarization-only approach ($q = 0$), shown for comparison. The oscillation frequency $\propto m = (2q \pm 1)$ highlights the improving angular resolution for increasing q.

Experimental imperfections lead to a non-unitary fringe visibility. As shown in Appendix A the loss of visibility increases the statistical error as:

$$\Delta\theta^m \geq \left[2mV_m\sqrt{\eta_m}\sqrt{\nu N}\right]^{-1} = \Delta\theta^m_{\min}, \tag{4.9}$$

where V_m is the visibility of the oscillation pattern and η_m the efficiency of the detection system. In our case, all curves show a visibility greater than 0.73. As a figure of merit for the enhancement in precision, we consider the ratio between the statistical error of the polarization-only strategy and of the photonic gear: $\Delta\theta^0/\Delta\theta^m \propto mV_m\sqrt{\eta_m/\eta_0}$. Figures 4.5 (a) and (b) show $\Delta\theta^0/\Delta\theta^m$ as a function of m obtained from the interference curves. We obtain a maximum enhancement over the polarization-only strategy by ≈ 55. To obtain the same precision $\Delta\theta$ with the polarization-only strategy, one would have to increase the number of trials by a factor of $55^2 = 3025$, while for the quantum NOON-state strategy, one would require entangled states of $N \approx 55$ photons each. As shown in Figure 4.5 (c)-(d), our estimation protocol gives an estimate $\overline{\theta}$ which converges to the true value θ in a limited number of trials $\nu \sim 300$, where ν is the number of single photons sent through the system. It is possible to show that a three-step adaptive protocol permits an efficient and unambiguous

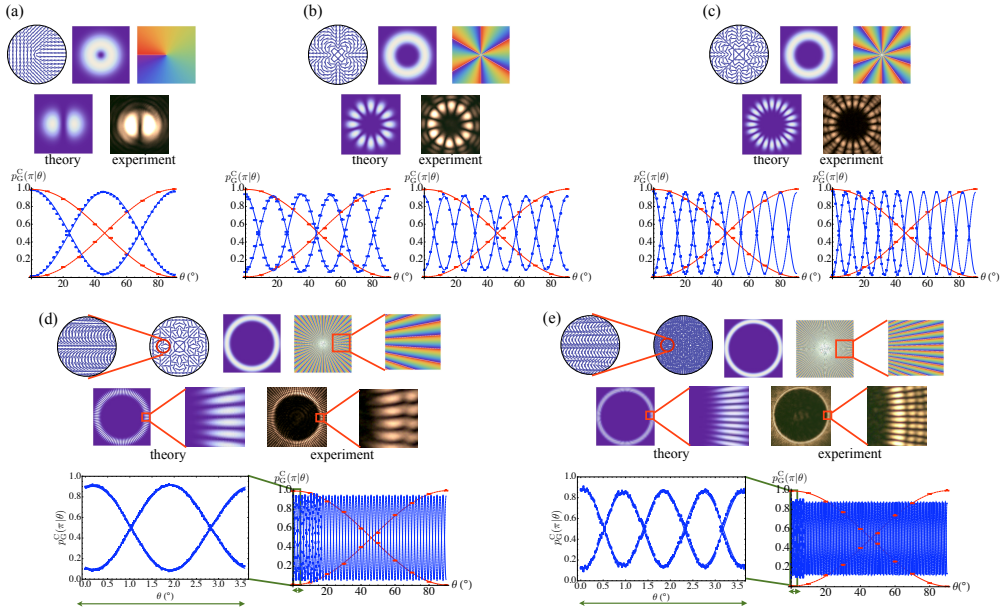

Figure 4.4. Single-photon experimental fringes. Experimental results for single photons and q-plate charges (a) $q = 1/2$ ($l = 1$), (b) $q = 3$ ($l = 6$), (c) $q = 5$ ($l = 10$), (d) $q = 25$ ($l = 50$), and (e) $q = 50$ ($l = 100$). For each case (a-e), we report: the q-plate axis pattern, corresponding to the distribution of the liquid crystal molecular director (top row, left panels); the calculated intensity and phase profiles of the generated OAM fields (top row, middle and right panels); the theoretical and experimental intensities after projection on the H-polarization state (middle panels); the measured fringe patterns (blue dots) as a function of the mechanical rotation angle θ, accompanied by sinusoidal best-fit curves (blue lines) and by the polarization-only case (red dots and lines) (bottom panels). The fringe patterns reported for cases (a,d-e) correspond to $m = 2q + 1$ [(a) $m = 2$, (d) $m = 51$, (e) $m = 101$]. Fringe patterns with $m = 2q - 1$ (without the HWPs, left plots) and $m = 2q - 1$ (with the HWPs, right plots) are shown in (b) ($m = 5$ and $m = 7$) and (c) ($m = 9$ and $m = 11$). In (d) and (e), an inset with a zoomed-in region of the fringes is also shown. Error bars in the polarization fringes are due to the poissonian statistics of the recorded events, while error bars in the set value of the angle θ are due to the mechanical resolution of the rotation stage.

estimation of such θ even when it is a completely unknown rotation in the full $[0, 2\pi)$ interval (see Appendix A).

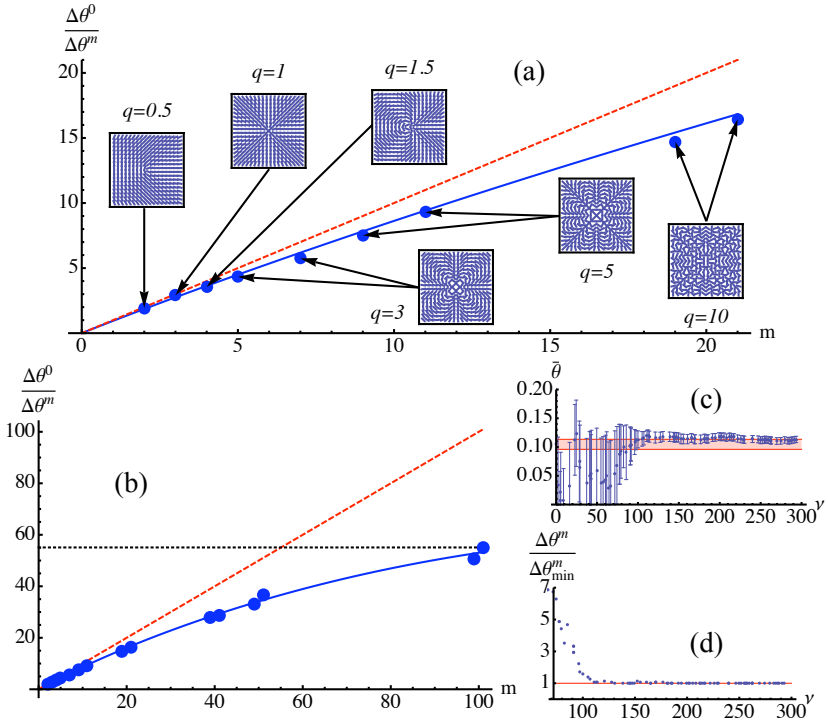

Figure 4.5. Estimation of a rotation angle with photonic gears in the single-photon regime. Ratio between the statistical errors $\Delta\theta^0/\Delta\theta^m$ for the polarization-only strategy versus the gears strategy in the single-photon regime for $q < 10$ (a) and for all the implemented values of q (b). In (a) for each point the pattern of the corresponding q-plate is also shown. We obtain a maximum precision enhancement of ≈ 55 for $q = 50$, corresponding to the generation of optical states with an OAM component with $l = 100$. Red dashed line: theoretical prediction for the ideal case. Blue solid line: model taking into account experimental imperfections [see Eq. (4.9). Black horizonal dashed line: experimental maximum enhancement. (c-d) Convergence of the angle estimation procedure as a function of the number of repeated experiments ν for $m = 7$ ($q = 3$). (c) Measured angle $\bar{\theta}$ versus the number of incident single photons ν (the red area corresponds to the true angle set in the apparatus, up to mechanical resolution). Error bars correspond to the statistical error in the estimation process. (d) Ratio $\Delta\theta^m/\Delta\theta^m_{\text{min}}$ showing the convergence to the Cramér-Rao bound (see Appendix A).

In figure 4.6, we show that the rotational sensitivity enhancement due to the photonic gears effect can also be achieved in the classical regime with an intense laser, making it immediately applicable to real-world optical measurements, which we will now briefly discuss. There, the most common problem is to perform precise non-contact and/or remote optical measurements of roll angles. These are mechanical rotations of an object around one of its symmetry axes [138, 134]. Polarization-based methods, essentially relying on the Malus' law combined with suitable polarization manipulations, are among the most convenient approaches. Depending on the details of the scheme, this typically leads to a sensitivity of about 10^{-2} degrees for a dynamical range of $30 - 360°$, or about 10^{-4} degrees when restricting the range to $\sim 1°$. All these polarization-based methods, irrespective of the details, can be combined with our photonic gear tool without changes. Their sensitivity is therefore predicted to be improved approximately by the factor $m \times V_m$, which we have shown can be made larger than 50. For example, the method reported in Ref.[138] combined

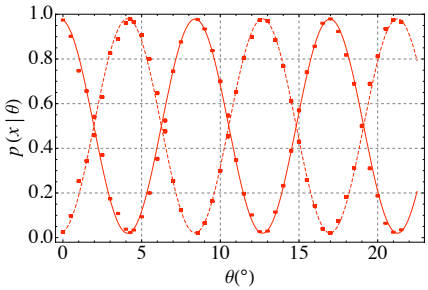

Figure 4.6. Classical regime hybrid photonic gears. The photonic gear concept based on hybrid polarization-OAM states can be adopted also with intense light in the classical regime. To this end, we prepared as input a $P = 1$ mW laser pulse with linear H polarization. The output state is analyzed by measuring the intensity in the two orthogonal linear H and V polarization directions. Here we report the measured oscillation patterns for classical intense input light with a value $q = 10$ and $m = 2q + 1 = 21$. We observe that the super-resolution effect due to the hybrid encoding is efficiently observed also when the input state is a coherent classical beam. Indeed, the experimental visibilities for the two output intensities $I_H(\theta)$ and $I_V(\theta)$ in this case are respectively $V_H = 0.95 \pm 0.02$ and $V_V = 0.91 \pm 0.02$. Points: experimental normalized intensities. Curves: corresponding best-fit curves. Error bars are due to fluctuations in the measured laser intensity.

with our photonic-gear enhancement is expected to achieve a maximal sensitivity of 10^{-6} degrees, or about 0.01 arcsec. The dynamical range is also reduced by a similar factor, but the full dynamical range can be recovered by an adaptive protocol discussed in [71].

We consider at last the quantum regime of entangled photons, using the setup shown in Fig. 4.7. We demonstrate two-photon entangled states where each photon has a different total angular momentum, m_1 and m_2, with a maximum of $m_1 + m_2 = 18$. We carried out two types of experiments. In the first, we generated photon pairs in the "entangled photonic gear state" $|\psi_G^-\rangle$, given in Eq.(4.8). We then measured the HH correlations for two different sets of q-plates. The results are reported in Fig. 4.8 and 4.9 as a function of the angles θ_A and θ_B of Alice's and Bob's stages. The enhancement in oscillation frequency in both the θ_A and the θ_B directions with respect to the polarization-only case is clearly observed and matches our theoretical predictions. Next, we generated the entangled state $|\phi_G^-\rangle$ and rotated the two stages by the same angle $\theta_A = \theta_B = \theta$, thus creating a situation analogous to the case of NOON state probes. The measurement results are shown in Fig. 4.9. The hybrid quantum-classical sensitivity enhancement by the factor $mN = m_A + m_B = 2q_A + 2q_B + 2$ is clearly observed, confirming again our predictions. In particular, the experimental comparison between the 2-photon quantum case with $|\phi_G^-\rangle$ and the single-photon case with $|\Psi_G^C\rangle$ shows that in the former case a quantum enhancement by a factor 2 is superimposed to the classical photonic gear effect.

Conclusions

In summary, we have reported a photonic scheme to measure rotation angles with greatly enhanced precision. We tested our photonic gears in three different regimes: (i) classical intense laser light; (ii) single-photon regime, that we adopted to quantitatively compare the achieved angular sensitivity with the shot-noise and Heisenberg limits; (iii) quantum regime of entangled photons, in which we demonstrated that the photonic gears can be combined with quantum correlations, leading to different kinds of "super-resolving" ro-

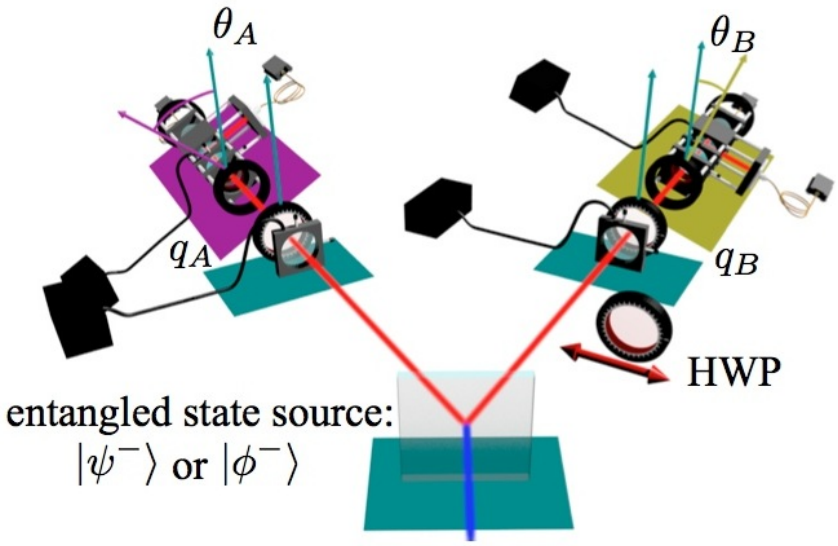

Figure 4.7. Entangled photonic gears. (a) Experimental setup. An entangled photon pair in the polarization state $|\psi^-\rangle$ is generated by type-II spontaneous parametric down conversion. The state can be converted to the $|\phi^-\rangle$ state by inserting a HWP in the path of Bob's photon. Each photon is then converted into SAM-OAM hybrid states by the q-plates q_{A} and q_{B} and a HWP, as before, and is sent to a different rotation stage for the analysis.

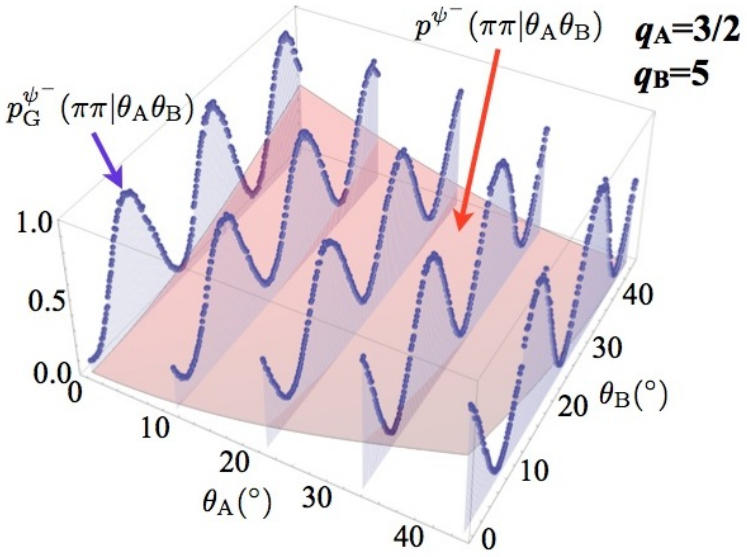

Figure 4.8. Entangled photonic gears. Normalized experimental correlations $p_{\mathrm{G}}^{\psi^-}(\pi\pi|\theta_{\mathrm{A}},\theta_{\mathrm{B}})$ (blue points), with $\pi\pi = HH$, obtained with the $|\psi^-\rangle$ state by measuring the two-fold coincidences in the H-polarization bases on both modes for different values of the rotation angles θ_{A} and θ_{B}. We observe the gear enhancement with respect to the polarization-only case (red surface, theory) in the oscillation frequencies in both directions θ_{A} (with $m_{\mathrm{A}} = 2q_{\mathrm{A}} - 1 = 2$) and θ_{B} (with $m_{\mathrm{B}} = 2q_{\mathrm{B}} + 1 = 11$). Error bars in the correlations are due to the poissonian statistics of the recorded events, while error bars in the set value of the angle θ are due to the mechanical resolution of the rotation stage.

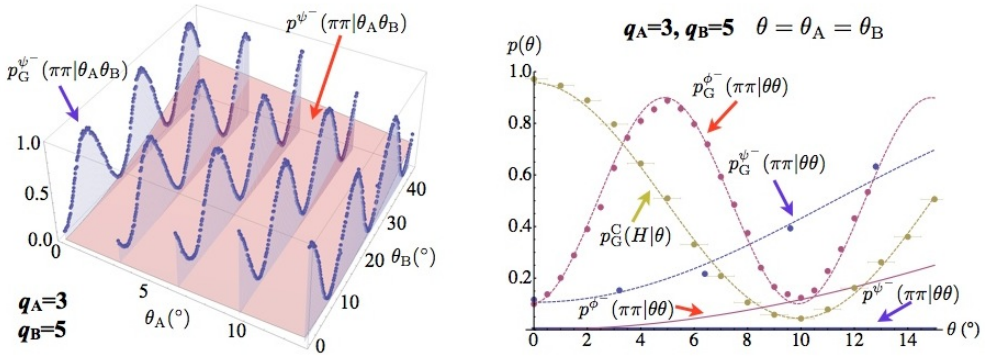

Figure 4.9. Entangled photonic gears. (left) Normalized experimental correlations with $|\psi^-\rangle$ (blue points) for $m_A = 2q_A + 1 = 7$ and $m_B = 2q_B + 1 = 11$. (right) Normalized experimental correlations obtained with the $|\psi^-\rangle$ and $|\phi^-\rangle$ states when rotating the two stages by the same angle $\theta_A = \theta_B = \theta$, for $m_A = 2q_A + 1 = 7$ and $m_B = 2q_B + 1 = 11$. The polarization correlations (blue points: data for $|\psi^-\rangle$, red points: data for $|\phi^-\rangle$) now present an oscillation pattern with a periodicity enhancement of $(m_A + m_B)$ for $|\phi^-\rangle$ and $m_A - m_B$ for $|\psi^-\rangle$, due to quantum entanglement combined with the gear effect. The theoretical polarization-only HH correlation (without the gear enhancement) are also shown, for reference, as a red solid curve in the $|\phi^-\rangle$ state case, oscillating as 2θ, and as a blue solid curve in the $|\psi^-\rangle$ state case, which is constant and vanishing. Yellow points: experimental data for single-photon gear with $m = (m_A + m_B)/2 = 9$, oscillating at half the frequency of $|\phi_G^-\rangle$. Dashed curves: best fit of the experimental data. The visibility of the pattern for $|\phi^-\rangle$ state is $V^{\phi_G^-} = 0.826 \pm 0.011$. Error bars in the correlations are due to the poissonian statistics of the recorded events, while error bars in the set value of the angle θ are due to the mechanical resolution of the rotation stage.

tational correlations between the two measurement stages receiving the two photons. In the regime of single-photon probes, a precision of $\sim 55\sqrt{\nu N}$ has been demonstrated experimentally, with νN the total number of photons. Notably, rather than in an asymptotic limit, this precision was attained already for total photon numbers as small as $\nu N \approx 10^2$ to 10^4. To our knowledge, this constitutes the highest precision per-particle reported so far [133, 153, 112, 106]. We produced a quantum state that is metrologically equivalent to a NOON state, leading to a hybrid quantum-classical enhancement of the angular sensitivity. The precision attained in this case scales as mN times the square root of the number of probes used, the m originating from the gear ratio and the N from quantum entanglement. We performed a proof-of-principle demonstration with $N = 2$ and total angular momentum up to 18.

Rotation sensors based on OAM have been reported before [111, 83, 65, 17, 130], but our approach is qualitatively different from all other OAM-related proposals in the fact that we use SAM-OAM combined states that allow us to "read" the rotation by a simple polarization measurement, thus without introducing the large photon losses arising from diffraction or transmission in the angular masks usually needed to read the OAM state. Immediate application of the photonic-gear concept in a classical regime can improve current polarization-based methods for measuring roll angles to a sensitivity of less than 0.01 arcsec. These values provide substantial progress over the current state of the art.

Chapter 5

Qudits and contextuality

This chapter is devoted to the application of qudits in fundamental quantum mechanics. High dimensional systems indeed show contexual correlations which are not accessible by exploiting qubits. Hence qudits are the key element for any quantum contextuality investigation. As we have seen in Chapter 1, contextual correlations arise only for systems with $d \geq 3$ hence orbital angular momentum (or path) results to be a precious resource for the realization of contextual experiments. In this chapter we consider two different experiments related to quantum contextuality. In the first one we report the experimental observation of an impossible-to-beat quantum advantage on a four dimensional quantum system defined by the polarization and orbital angular momentum of a single photon. The second experiment has been made in collaboration with the quantum optics group of Stockholm University and represents the first experimental realization of a Kochen-Specker set. In both experiments is exploited a hybrid ququart (OAM-polarization) space spanned by vectors:

$$\{|H,+m\rangle, |H,-m\rangle, |V,+m\rangle, |V,-m\rangle\} \tag{5.1}$$

The choice of the hybrid encoding for ququarts is due mainly to two factors:

- Since only the OAM subspace $\{|-m\rangle, |+m\rangle\}$ is involved, hybrid qubits are not affected by decoherence due to different Gouy-phase for free propagation.
- Hybrid ququarts can be generated and detected by exploiting q-plates which are much more efficient than SLMs. Indeed, although both devices are based on liquid crystals, q-plates consist of a single liquid crystal cell so they do not induce diffraction losses due to pixelization.

Hybrid ququarts are also the basic resource of an experiment proposal for quantum cryptography protected by Kochen-Specker contextuality which is reported in the last section of this chapter.

The obtained results have been published in:
[E. Nagali, V. D'Ambrosio, F. Sciarrino, A. Cabello, *Experimental Observation of Impossible-to-Beat Quantum Advantage on a Hybrid Photonic System*, Phys. Rev. Lett. 108, 090501 (2012)],
[V. D'Ambrosio, I. Herbauts, E. Amselem, E. Nagali, M. Bourennane, F. Sciarrino, A. Cabello, *Experimental implementation of a Kochen-Specker set of quantum tests*, Phys. Rev. X 3, 011012 (2013)] and
[A. Cabello, V. D'Ambrosio, E. Nagali, F. Sciarrino, *Hybrid ququart-encoded quantum cryptography protected by Kochen-Specker contextuality*, Phys. Rev. A 84, 030302 (2011)].

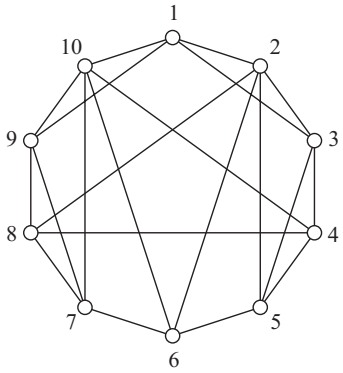

Figure 5.1. Exclusivity graph representing the simplest task of the class with quantum but no post-quantum advantage. Vertices represent propositions, edges link propositions that cannot be simultaneously true.

5.1 Impossible to beat quantum advantage

The search for properties singling out quantum mechanics from more general theories has recently attracted much attention [104, 164, 157, 66, 142, 60, 18, 73]. In this framework, it is natural to address questions such as which is the simplest task in which quantum mechanics provides an advantage over classical theories and no hypothetical post-quantum theory can do it better. Some recent results have seed light on this problem. Let us consider the class of tasks requiring to maximize a sum Σ of probabilities of propositions tested on a system (this class includes some communication complexity tasks [41] and all noncontextual [47, 116, 7] and Bell inequalities). We know that the maximum of Σ is given by $\alpha(G)$, $\vartheta(G)$, or $\alpha^*(G)$, depending on whether classical, quantum, or general resources are used and G indicates the exclusivity graph for our system. The simplest task of this class in which there is a quantum advantage but no post-quantum theory outperforms quantum mechanics corresponds to the simplest graph such that $\alpha(G) < \vartheta(G) = \alpha^*(G)$, requiring a quantum system with the lowest possible dimensionality $\chi(G)$.

In order to experimentally implement the simplest task with quantum but no post-quantum advantage we exploit the properties of the graph of Fig. 5.1, identified in [52] as the simplest one with these properties. Specifically, for this graph $\alpha(G) = 3$ while $\vartheta(G) = \alpha^*(G) = 3.5$ with $\chi(G) = 4$. Experimentally we adopt a photonic hybrid system of dimension four, encoded in the polarization and a bidimensional subspace of the orbital angular momentum. The high-fidelity and reliability of the present scheme allow to achieve a close to theory measured value and a direct test of the exclusivity of the 10 involved orthogonal projectors.

There is a one-to-one correspondence between $\alpha(G)$, $\vartheta(G)$, and $\alpha^*(G)$ and the classical, quantum, and general bounds for the following task: given an $n(G)$-vertex graph G, each player is asked to prepare a physical system and provide a list of $n(G)$ yes-no questions (or tests) Q_i on this system, satisfying that questions corresponding to adjacent vertices in G cannot both have the answer yes. The player who provides the preparation and questions with the highest probability of obtaining a yes answer when one question is picked at random wins.

If the questions refer to preexisting properties,that is, all the answers have a predefine value, the highest probability of obtaining a yes answer is $\alpha(G)/n(G)$. For the graph in Fig.

5.1, the sum of the probabilities of obtaining a yes answer is

$$\Sigma = \sum_{i=1}^{10} P(Q_i = 1) \leq 3 = \alpha(G), \tag{5.2}$$

since at most 3 of the questions in Fig. 5.1 can be true.

However in quantum mechanics, preparing a four-level system in the state

$$\langle\psi| = (0, 0, 0, 1), \tag{5.3}$$

and testing the propositions represented by the projectors $|v_i\rangle\langle v_i|$ over the following 10 (non-normalized) vectors $\langle v_i|$:

$$\langle v_1| = (0, 0, 1, 1), \tag{5.4a}$$
$$\langle v_2| = (1, -1, 1, -1), \tag{5.4b}$$
$$\langle v_3| = (1, -1, -1, 1), \tag{5.4c}$$
$$\langle v_4| = (1, 0, 0, -1), \tag{5.4d}$$
$$\langle v_5| = (1, 1, 1, 1), \tag{5.4e}$$
$$\langle v_6| = (0, 1, 0, -1), \tag{5.4f}$$
$$\langle v_7| = (-1, 1, 1, 1), \tag{5.4g}$$
$$\langle v_8| = (1, 0, 0, 1), \tag{5.4h}$$
$$\langle v_9| = (1, 1, 1, -1), \tag{5.4i}$$
$$\langle v_{10}| = (1, 1, -1, 1), \tag{5.4j}$$

the probability of obtaining a yes answer is $\frac{7}{20} = 0.35$, which is the maximum using quantum resources [namely, $Q(G)/n(G)$], since for the graph in Fig. 5.1,

$$Q(G) = \frac{7}{2}. \tag{5.5}$$

which does not only go beyond the classical limit, but actually saturates the bound for any post-quantum theory. The simplest way to grasp the previous bound is to notice that any other assignment of probabilities to the vertices of the graph in Fig. 5.1 either does not beat the $7/2$ benchmark or is inconsistent with the requirement that the sum of probabilities of mutually adjacent vertices (i.e. those representing mutually exclusive propositions) cannot be larger than 1. As explained in Chapter 1, there is a one-to-one correspondence between the maximum of the sum of the probabilities and the fractional packing number of the graph in which vertices represent propositions and edges exclusiveness. The fractional packing number of the graph in Fig. 5.1 is $7/2$. The remarkable property of the graph in Fig. 5.1 is that $\vartheta(G) = \alpha^*(G)$, so no post-quantum theory can improve this performance. Unlike standard Bell tests where hypothetical post-quantum theories can outperform quantum mechanics [9], here quantum mechanics reaches the maximum performance allowed by the laws of probability, as in this case there is no way to assign probabilities outperforming the quantum ones without violating that the sum of the probabilities of exclusive propositions cannot be higher than 1. Indeed, what makes this experiment special is that it aims the simplest scenario where the quantum probabilities exhibit this curious property.

Experimental implementation

To experimentally verify the quantum predictions we require a four dimensional system and the ability to project ququart states over all the states in Eqs. (5.4) with high fidelity and high reliability. These states are found to belong to all the five different mutually unbiased basis of a ququart [118, 171]. We encoded such high dimensional quantum states by exploiting polarization and orbital angular momentum of the same photon. Here we considered the bidimensional subset of OAM space with $|l| = 2$ (o_2). According to the nomenclature $|\varphi, \phi\rangle = |\varphi\rangle_\pi |\phi\rangle_{o_2}$, the logic ququart basis can be written as

$$\{|H, +2\rangle, |H, -2\rangle, |V, +2\rangle, |V, -2\rangle\}, \tag{5.6}$$

where H (V) refers as usual to horizontal (vertical) polarization. According to these definitions, a generic ququart state expressed as (a_1, a_2, a_3, a_4), as in (5.4), can be experimentally implemented as

$$a_1|H, +2\rangle + a_2|H, -2\rangle + a_3|V, +2\rangle + a_4|V, -2\rangle. \tag{5.7}$$

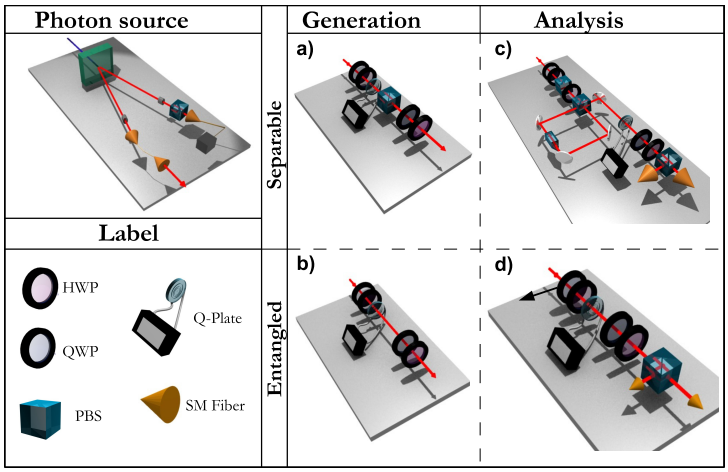

Figure 5.2. Experimental setup for the measurement of the probabilities $P(\Pi_i = 1)$ on different polarization-orbital angular momentum states. In the upper left corner is represented the single photon source. The four schemes we used for the experiment are presented in the right part of the figure. Each state is prepared by one of the two setups of the Generation column: Setup a) for separable states (quantum probabilistic transferrer $\pi \to o_2$ [152]) and setup b) for entangled ones (an "entangler" based on a QP and waveplates). The Analysis column shows the setups for the projection onto the desired states. Setup c) for separable states, a deterministic transferrer $o_2 \to \pi$, and setup d) for entangled states, where a QP is needed to have a deterministic detection.

In Table 5.1 we report the projections over the ten ququart states of the input state $(0, 0, 0, 1) = |V, -2\rangle$ needed to obtain the maximum possible violation in quantum mechanics.

The experimental setup adopted for such measurements is shown in Fig. 5.2. The SPDC source described in section 2.4.2 generates heralded single photon states, sent through single mode fiber to setup a) in order to encode the input state $(0, 0, 0, 1)$, generated adopting a quantum transferrer $\pi \to o_2$. This tool allows to transfer the information initially encoded in the polarization degree of freedom to the OAM, by exploiting the features of the q-plate device combined to a polarizing beam splitter (PBS) [151]. In particular, the input state has been generated by adopting the experimental setup in Fig. 5.2 for separable states, where the first two waveplates were oriented to generate right circular polarization, and the second two

State projection	Code	Type	Probabilities	
			Theory	Experiment
$(0,0,1,1)$	1	S	1/2	0.69 ± 0.02
$(1,-1,1,-1)$	2	S	1/4	0.160 ± 0.007
$(1,-1,-1,1)$	3	S	1/4	0.145 ± 0.006
$(1,0,0,-1)$	4	E	1/2	0.44 ± 0.01
$(1,1,1,1)$	5	S	1/4	0.33 ± 0.01
$(0,1,0,-1)$	6	S	1/2	0.49 ± 0.01
$(-1,1,1,1)$	7	E	1/4	0.160 ± 0.007
$(1,0,0,1)$	8	E	1/2	0.51 ± 0.01
$(1,1,1,-1)$	9	E	1/4	0.34 ± 0.01
$(1,1,-1,1)$	10	E	1/4	0.218 ± 0.008
		SUM	**7/2**	3.49 ± 0.03

Table 5.1. Theoretical predictions and experimental results for the probabilities of the different outcomes from measurements on state $(0,0,0,1) = |V,-2\rangle$. We associate to each projection a number used later to identify the state. In column Type we specify if the state is separable (S) or entangled (E).

waveplates for vertical polarization. Then, measurements have been carried out adopting the measurement setups in Fig. 5.2, depending on whether the state on which the projection had to be carried out was separable or entangled. For the projection on separable states (denoted by S in Table 5.1), we adopted the deterministic transferrer $o_2 \rightarrow \pi$ based on a Sagnac interferometer 2.4. Thanks to this setup, any qubit encoded in a bidimensional subspace of OAM $|\varphi\rangle_{o_2}$ is transferred to the polarization with probability $p = 1$. When the analysis on entangled states has to be carried out, it is possible to exploit the capability of the q-plate to disentangle the polarization from the OAM of a single photon. Indeed, for such projections we adopted a q-plate and a standard polarization analysis setup. The experimental results are reported in Table 5.1 and compared to the theoretical value of $Q(G) = 7/2$. We observed a good agreement with the theoretical expectations, thus demonstrating the advantage of adopting quantum resources over classical ones.

As a second step, we provide the experimental verification of exclusiveness relations between the different states in (5.4), that is, the fact that states connected by and edge cannot be simultaneously both true. We denote by a number from 1 to 10 the states involved in the experiment, and measured the probabilities $p(i,j)$ and $p(j,i)$, where $i,j = 1,\ldots,10$. For the generation of ququart states belonging to entangled bases, we adopted the scheme reported in Fig. 5.2.

In Fig. 5.3 a) we report the experimental values of probabilities $p(i,i)$, measured in order to ensure a high fidelity in the generation and reliability of all ququart states involved in the experiment. In particular, we observed an average fidelity of $F = (0.9492 \pm 0.0001)$. To verify that experimentally we implement orthogonal projectors, we measured the probabilities $p(i,j)$ and $p(j,i)$ where i and j represent two connected vertices in the graph of Fig. 5.1. In Fig. 5.3 b) we report the histogram of the occurrence of different values of probabilities, that quantify the non-orthogonality component of the experimental projectors. We observe a good agreement with the null value expected for orthogonal states. Error bars have been evaluated by considering the poissonian statistics of photon events.

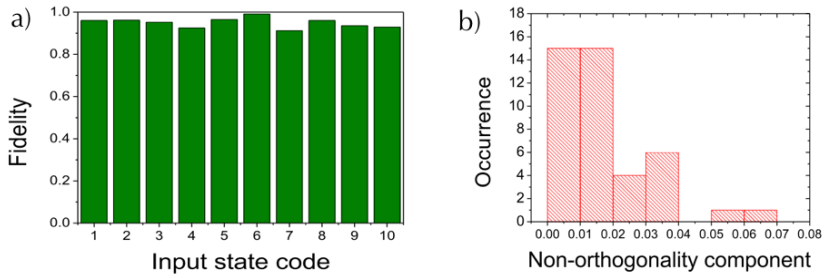

Figure 5.3. a) Experimental fidelities of generation and analysis for the ten states of the graph in Fig. 5.1. b) Experimental results of the exclusiveness test: occurrences of the non orthogonality component of the experimental projectors adopted for the measurements.

Discussion

The classical inequality (5.2) is valid under the assumption that the measured propositions satisfy the exclusiveness relations given by the graph in Fig. 5.1. The results in Fig. 5.3 show a very good agreement with the assumption. Even if the agreement between the experimental sum of probabilities is high, for some probabilities the deviations from the theoretical results are larger than the error bars. We attribute such discrepancy to the experimental implementation of the projectors, whose orientation respect to the input state is slightly different from the expected one. Assuming that inequality (5.2) is only valid with probability $1 - \epsilon$ and assuming that the worst case scenario, in which there are no links in the graph so the bound of the inequality is 10, occurs with probability ϵ, to certify the quantum advantage it is enough that $3(1 - \epsilon) + 10\epsilon < 3.49$. That is, that $\epsilon < 0.071$. The fact that all our 42 experimental probabilities satisfy this condition and that the average value of $\epsilon = 0.016 \pm 0.001$ certify the impossible-to-beat quantum advantage. To our knowledge, this is the first time an experiment aiming a task with quantum but no post-quantum advantage [9, 215, 123] has show results which demonstrate the quantum advantage and are compatible with the impossibility of a better performance.

5.2 Experimental implementation of a Kochen-Specker set of quantum tests

Although the violation of the NC inequality demonstrated in the previuos section certifies the quantum advantage respect to classical resources, it doesn't hold for any system. Indeed the maximum value of Σ is reached only when we project the state $|V, -2\rangle$ over the states reported in table 5.1 corresponding to the 10 vertices of the graph in fig 5.1. Other states will give lower values for Σ.

The conflict between classical and quantum physics can be identified through a series of yes-no tests on quantum systems, without it being necessary that these systems be in special quantum states. Kochen-Specker (KS) sets of yes-no tests have this property and provide a quantum vs classical advantage, free of the initialization problem affecting some quantum computers.

In this section we report the results of a collaboration between quantum optics groups of "Sapienza" University and Stockholm University consisting of two separate experiments based on the same exclusivity graph. In the first experiment, (performed in Rome) we use the polarization and orbital angular momentum of single photons to show how a KS

set can be applied to obtain a state-independent impossible-to-beat quantum vs classical advantage in a specific task. This demonstrate the unique power of this KS set for solving a task avoiding the problem of state initialization. In the second experiment (performed in Stockholm), they produce correlations violating a NC inequality constructed in one-to-one correspondence with the eigenstates of the same KS set, by performing sequential measurements of compatible observables encoded in the path and polarization degrees of freedom of single photons. This shows how KS sets can be used to obtain state-independent maximally contextual quantum correlations.

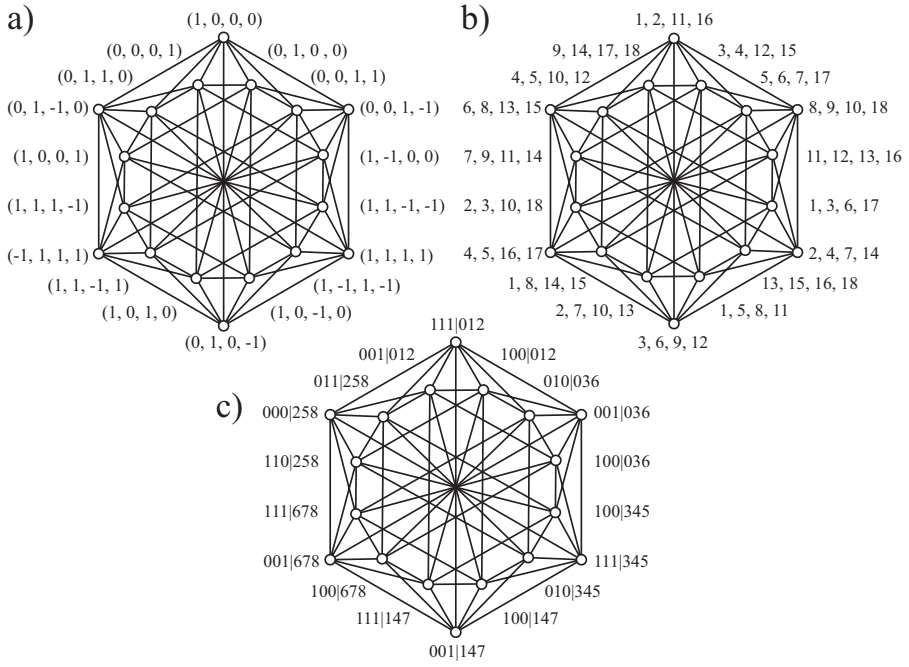

Figure 5.4. a) The 18-test KS set. Each vertex represents a yes-no test (associated in QM to a projector $\Pi_i = |v_i\rangle\langle v_i|$, where $\langle v_i|$ are the unit vectors displayed in the figure; normalization factors are omitted to simplify the notation), and adjacent vertices correspond to exclusive tests (i.e., they cannot both have the answer yes on the same system; in QM they are associated to orthogonal projectors). This vector representation is the one adopted in our experiments. **b) Optimal strategy for the task described in the text using classical resources.** The system is a ball which can be placed in one out of 18 boxes, and "1, 2, 11, 16" denotes the following yes-no test: "Is the ball in box 1 or in box 2 or in box 11 or in box 16?". The set of classical tests in b) results in the maximum probability of obtaining yes using classical resources. **c) Propositions tested in the non-contextuality inequality (5.12) used to obtain state-independent maximally contextual quantum correlations.** Each vertex represents a proposition $abc|xyz$, denoting "The result of measuring x is a, the result of measuring y is b, and the result of measuring z is c". When the measurements are those in (5.11), then each of these sequences of measurements and results projects any initial state onto the corresponding state in a).

Experimental observation of state-independent impossible-to-beat KS-based quantum advantage using polarization and orbital angular momentum of photons

Consider again the task of the previous section [149]: Given an n-vertex graph G, provide n yes-no tests about a physical system, such that each test is associated to a vertex of G, exclusive tests correspond to adjacent vertices, and such that these tests result in the highest

probability of obtaining a yes answer when one of them is chosen at random. As we know, this highest probability may be different depending on whether the physical system and the tests are classical, quantum, or post-quantum. Moreover, for arbitrary graphs, the highest probability may also depend on the state in which the system is prepared. However, two distinguishing features of the graph of Fig. 5.4 a) are that the highest probability in QM can be reached regardless of the state of the system, and cannot be outperformed by any post-quantum theory.

If the available resources are classical, i.e., physical systems with preassigned results and tests thereof, then an optimal strategy is illustrated in Fig. 5.4 b). There, the classical system is assumed to be a ball that can be placed in one out of 18 boxes numbered from 1 to 18. For instance, a yes-no test is: "Is the ball in box 1 or in box 2 or in box 11 or in box 16?", denoted as "1, 2, 11, 16". The other tests are shown in Fig. 5.4 b). The 18 tests satisfy the graph's relations of exclusivity. In addition, no matter which box the ball is placed in, the probability of getting a yes answer when one of the 18 tests is chosen at random is $4/18 \approx 0.22$, since the answer is always "yes" for 4 of the tests and "no" for the others. Alternatively, the performance can be measured by the sum Σ of the probabilities of obtaining a yes answer. For this graph the independence number $\alpha(G) = 4$. Therefore, using classical resources,

$$\Sigma = \sum_{i \in V(G)} P(\Pi_i = 1) \leq 4. \tag{5.8}$$

where $V(G)$ is the set of vertices of the graph in Fig. 5.4 a) and $P(\Pi_i = 1)$ is the probability of obtaining the result 1 (yes) for the yes-no test Π_i.

However, it can be easily checked that, if we use the 18 quantum yes-no tests $\Pi_i = |v_i\rangle\langle v_i|$ in Fig. 5.4 a), then the probability of a yes answer is $1/4 = 0.25$ and

$$\Sigma_{\mathrm{QM}} = 4.5. \tag{5.9}$$

Since this advantage is independent of the initial quantum state of the system, this is an example of a task with quantum advantage for which the initialization problem affecting nuclear magnetic resonance quantum computers [92, 64] is not an obstacle. Moreover, as for the graph in Fig. 5.1, the Lovátz number is equal to the fractional packing number for this task ($\vartheta(G) = \alpha^*(G) = 4.5$), hence even hypothetical post-quantum theories cannot outperform QM.

Experimental state independent quantum advantage

In order to test this state-independent impossible-to-beat quantum advantage in an experiment, we used again the hybrid polarization-OAM encoding described in the previous section. Again the space we exploit is spanned by vectors:

$$\{|H, +2\rangle, |H, -2\rangle, |V, +2\rangle, |V, -2\rangle\}, \tag{5.10}$$

and the experimental setup is the one shown in Fig.5.2.

Since now the advantage is state independent, we measured for 28 different input states the projections over the 18 states which consitute the KS set and whose components in our four dimensional space are reported in Fig.5.4a. The experimental results for Σ, as measured on 15 different states, are reported in Table 5.2. The experimental data are in good agreement with the theoretical prediction, with a mean value of $\Sigma_{exp} = 4.512 \pm 0.005$ to be compared

Code	State	Implementation	Σ
v_1	(1,0,0,0)	$\|H,+2\rangle$	4.60 ± 0.02
v_2	(0,1,0,0)	$\|H,-2\rangle$	4.45 ± 0.02
v_7	(1,1,1,1)	$\|A,h\rangle$	4.50 ± 0.02
v_{11}	(1,0,1,0)	$\|A,+2\rangle$	4.51 ± 0.02
v_{15}	(1,0,0,1)	$\|\psi_1\rangle = \frac{1}{\sqrt{2}}(\|H,+2\rangle + \|V,-2\rangle)$	4.59 ± 0.02
v_{16}	(0,1,-1,0)	$\|\psi_3\rangle = \frac{1}{\sqrt{2}}(\|H,-2\rangle - \|V,+2\rangle)$	4.47 ± 0.01
v_{17}	(0,1,1,0)	$\|\psi_4\rangle = \frac{1}{\sqrt{2}}(\|H,-2\rangle + \|V,+2\rangle)$	4.41 ± 0.02
v_{18}	(0,0,0,1)	$\|V,-2\rangle$	4.50 ± 0.02
v_{19}	(0,0,1,0)	$\|V,+2\rangle$	4.45 ± 0.03
v_{20}	(1,1,0,0)	$\|H,h\rangle$	4.57 ± 0.02
v_{24}	(1,0,0,-1)	$\|\psi_2\rangle = \frac{1}{\sqrt{2}}(\|H,+2\rangle - \|V,-2\rangle)$	4.58 ± 0.02
ρ_{25}		$\frac{13}{16}\|\psi_1\rangle\langle\psi_1\| + \frac{1}{16}\sum_{j=2}^{4}\|\psi_j\rangle\langle\psi_j\|$	4.57 ± 0.02
ρ_{26}		$\frac{5}{8}\|\psi_1\rangle\langle\psi_1\| + \frac{1}{8}\sum_{j=2}^{4}\|\psi_j\rangle\langle\psi_j\|$	4.55 ± 0.02
ρ_{27}		$\frac{7}{16}\|\psi_1\rangle\langle\psi_1\| + \frac{3}{16}\sum_{j=2}^{4}\|\psi_j\rangle\langle\psi_j\|$	4.53 ± 0.02
ρ_{28}		$\frac{1}{4}\sum_{j=1}^{4}\|\psi_j\rangle\langle\psi_j\|$	4.50 ± 0.02
Average value			4.512 ± 0.005

Table 5.2. Experimental results for Σ for 15 quantum states. Each input state was projected onto each of the 18 states in Fig. 5.4 a). Notation: $|A\rangle = \frac{|H\rangle+|V\rangle}{\sqrt{2}}$, $|h\rangle = \frac{|+2\rangle+|-2\rangle}{\sqrt{2}}$. Error bars were evaluated by considering the Poissonian statistics of coincidence counts. All reported values lie in the range $[\Sigma_{min}, \Sigma_{max}]$ (see Fig. 5.5).

to $\Sigma = 4.5$, and shows the clear advantage of the quantum settings with KS projectors over any classical strategy.

In addition, the exclusivity between the tests in Fig. 5.4 a) was experimentally verified, confirming that tests corresponding to adjacent vertices cannot be both simultaneously true. Experimentally, the probabilities $P_{|v_j\rangle}(\Pi_i = 1)$, obtained by projecting the state $|v_i\rangle$ onto the state $|v_j\rangle$ for orthogonal states (adjacent vertices), are close to 0, as expected. Specifically, we obtained that the mean value of $P_{|v_j\rangle}(\Pi_i = 1)$ is $\epsilon = (0.014 \pm 0.001)$.

The theoretical classical and quantum bounds for the task should be properly corrected to take into account that $\epsilon \neq 0$. As in the previous section, assuming that inequality (5.8) is only valid with probability $1-\epsilon$ and that the worst case scenario, in which there are no edges so the upper bound of the inequality is 18, occurs with probability ϵ, to certify the quantum advantage it is enough that $4(1-\epsilon) + 18\epsilon < \Sigma$, which, using $\Sigma = 4.5$, implies $\epsilon < 0.035$, a condition which is fulfilled in our experiment. Moreover, we expect to observe a quantum advantage lying in a range $[\Sigma_{min}, \Sigma_{max}]$, where $\Sigma_{min} = 4.5(1-\epsilon)$ and $\Sigma_{max} = 4.5(1-\epsilon) + 18\epsilon$. Here Σ_{max} (Σ_{min}) corresponds to the situation of having all 18 propositions true (false) with probability ϵ. In Fig. 5.5 we report the experimental values of Σ, not only for the 15 states in Table 5.2, but also for other 13 states. The quantum advantage is observed for all 28 states, in good agreement with the state-independent value predicted by the theory.

Experimental state-independent maximally contextual quantum correlations by sequential measurements on polarization and path of photons

KS sets can also be used to generate non-classical contextual correlations by performing sequential compatible measurements on individual systems. The signature of non-classicality

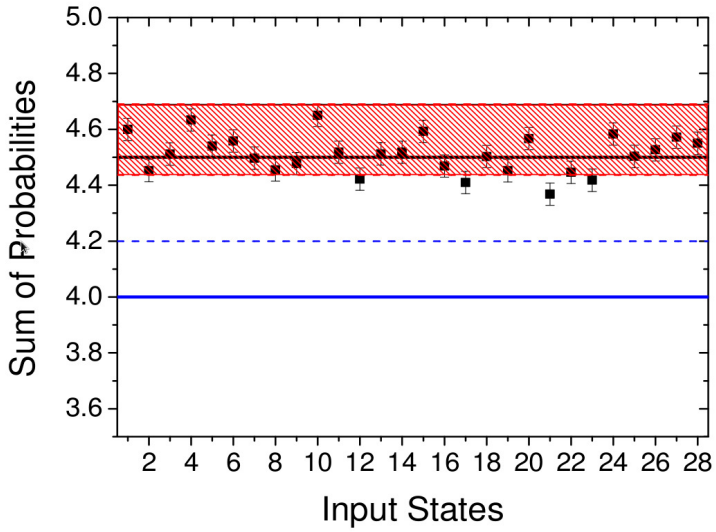

Figure 5.5. Experimental results for Σ for 28 quantum states. The solid (dashed) blue line refers to the (corrected) classical upper bound for Σ. The red area represents the range $[\Sigma_{min}, \Sigma_{max}]$ in which we theoretically expect to find all experimental values of Σ. The first 18 states correspond to the ones in Fig. 5.4 a). States 19–28 are defined in Table 5.2.

is the violation of a NC inequality, which is an inequality involving linear combinations of joint probabilities of sequential compatible measurements, satisfied by any NCHV theory.

For most of the experimental demonstrations of contextual correlations reported before this experiment [145, 21, 127, 6], the system had to be prepared in a special state. There are also theoretical [47] and experimental works [117, 7, 148] on state-independent contextuality. However, none of the previous experiments implement a KS set of yes-no tests.

In the Stockholm experiment they use the KS set of Fig. 5.4 a) to obtain a non-contextuality inequality violated by any quantum state. This inequality follows from identifying sequential compatible measurements such that any initial state is projected onto one of the eigenstates of the yes-no tests of the KS set of Fig. 5.4 a). This guarantees that the propositions *abc|xyz* denoting "the result of measuring x (first measurement of the sequence) is a, the result of measuring y (second) is b, and the result of measuring z (third) is c" keep all the relations of exclusivity existing in Fig. 5.4 a).

It can be easily seen that, by using the following measurements:

$$\begin{array}{lll} 0 := \sigma_z \otimes \mathbb{I}, & 1 := \mathbb{I} \otimes \sigma_z, & 2 := \sigma_z \otimes \sigma_z, \\ 3 := \mathbb{I} \otimes \sigma_x, & 4 := \sigma_x \otimes \mathbb{I}, & 5 := \sigma_x \otimes \sigma_x, \\ 6 := \sigma_z \otimes \sigma_x, & 7 := \sigma_x \otimes \sigma_z, & 8 := \sigma_y \otimes \sigma_y, \end{array} \tag{5.11}$$

where σ_x, σ_y, and σ_z are the Pauli matrices along the x, y, and z directions, $\otimes$ denotes tensor product, and assigning the results 0 and 1 to the degenerate eigenvalues -1 and 1 of the operators, the 18 propositions in Fig. 5.4 c) are in one-to-one correspondence with the 18

states in Fig. 5.4 a). Therefore, the corresponding non-contextuality inequality reads

$$\begin{aligned}\xi =& P(001|012) + P(111|012) + P(100|012) \\ &+ P(010|036) + P(001|036) + P(100|036) \\ &+ P(100|345) + P(111|345) + P(010|345) \\ &+ P(100|147) + P(001|147) + P(111|147) \\ &+ P(100|678) + P(001|678) + P(111|678) \\ &+ P(110|258) + P(000|258) + P(011|258) \overset{\text{NCHV}}{\leq} 4,\end{aligned} \tag{5.12}$$

where the upper bound for NCHV theories follows from the classical bound of inequality (5.8). For any initial state, these sequences of quantum measurements lead to

$$\xi_{\text{QM}} = 4.5, \tag{5.13}$$

in correspondence with the quantum advantage (5.9). Again, the contextuality revealed by this violation cannot be outperformed by any post-quantum theory.

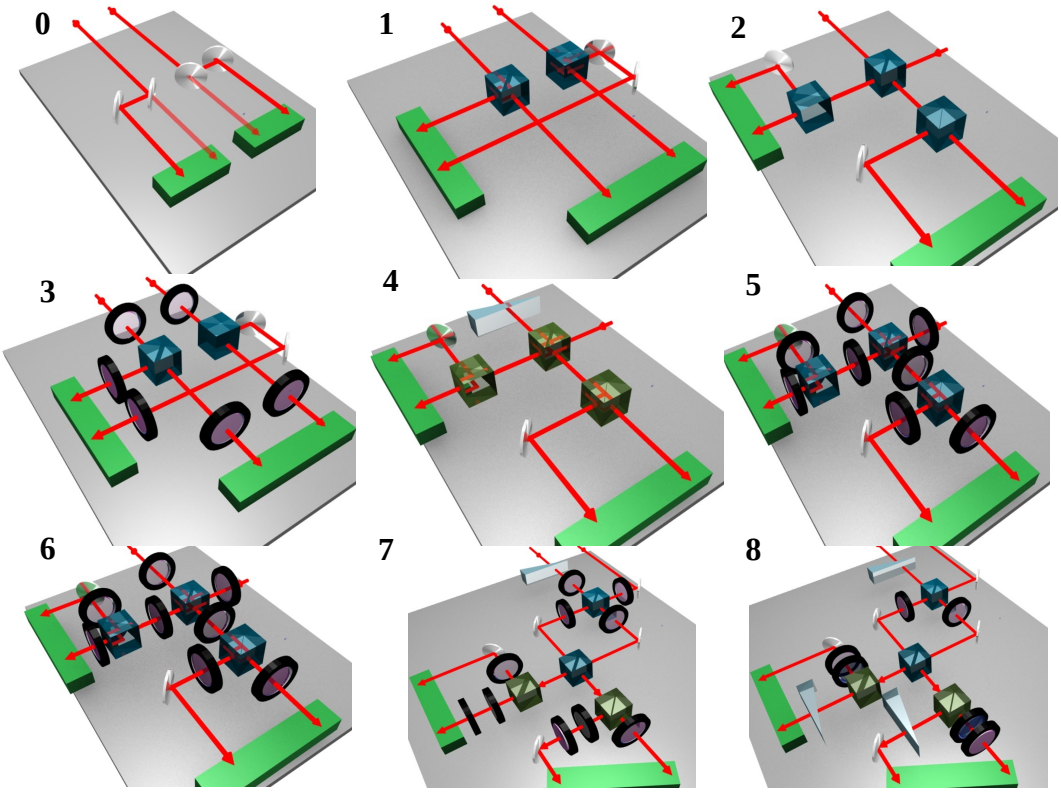

Figure 5.6. Stockholm experimental setups for the observables in (5.11). For the measurement of observable 0, it is only necessary to distinguish between the paths r and t. To measure observable 4, a polarization-independent beam splitter is used to distinguish the eigenstates through interference. The measurements of observables 1 and 3 are standard polarization measurements using PBSs and HWPs. Observables 2, 5, and 8 are Bell-state measurements, and so are the measurements of 6 and 7, but in the latter group the Bell measurement is preceded by a rotation of the polarization to guarantee compatibility with observable 8. To measure the probabilities appearing in inequality (5.12), these measurement devices are arranged in a cascaded way [6, 7].

Inequality (5.12) has been tested in a separate experiment performed in Stockholm university using hybrid ququarts encoded in the spatial path and polarization of the photon. For this experiment, the logical basis is

$$\{|t,H\rangle,|t,V\rangle,|r,H\rangle,|r,V\rangle\}, \tag{5.14}$$

where t and r denote the transmitted and reflected paths of the photon, respectively, and H and V denote horizontal and vertical polarization, respectively.

The experiment involves testing a sequence of three compatible measurements, corresponding to rows or columns in (5.11). To do so, the experimental setup is designed as a cascade of measurement boxes representing the compatible observables, preceded by a preparation device, and followed by detectors [6, 7]. The preparation device consists of a source of H-polarized single photons, implemented using a narrow bandwidth cw diode laser at 780 nm of long coherence length, attenuated to a mean photon number of 0.06 photons per coincidence gate. Combinations of HWPs, PBSs, and a wedge placed after the single-photon source create any desired state in the logical basis 5.14. The detection stage uses calibrated silicon avalanche photodiodes, with a 8-channel coincidence logic, and a coincidence window of 1.7 ns.

Crucial for the experimental test of the non-contextuality inequality (5.12) is the proper design of the devices for measuring the observables in (5.11). These devices should satisfy two conditions: compatibility [the three measurements corresponding to rows and columns in (5.11) should be compatible, so that any subsequent measurement of any of them would give the same result] and non-contextuality [every observable in (5.11) has to be measured using the same device in any of the sequences]. These conditions were achieved with the design of the 9 measuring devices shown in Fig. 5.6.

To construct the cascade setup, displaced Sagnac interferometers have been used due to their high stability. The obtained visibilities were in the 90%–99% range, depending on the implemented sequence. The experimental value of ξ for 15 different quantum states is reported in Table 5.2. Under the assumption that the detected photons were an unbiased subset of the emitted photons (fair sampling assumption), the results in Table 5.2 are in good agreement with a state-independent violation of inequality (5.12). The deviations from the quantum prediction for an ideal experiment with perfect compatibility are due to the systematic errors arising from the interferometers, the light-mode overlapping, and the imperfection of the polarization components.

5.3 Hybrid ququart-encoded quantum cryptography protected by Kochen-Specker contextuality

In the last chapter we have seen how hybrid ququarts can be used to violate non-contextual inequality by realizing Kochen-Specker sets of quantum tests. Here we show how Kochen-Specker contextuality can offer an extra protection in quantum key distribution protocols.

QKD protocols allow two distant parties to share a secret key by exploiting the fundamental laws of quantum mechanics (see Chapter 1). However, standard quantum cryptographic protocols based on quantum complementarity, like BB84 [29], are nonsecure against attacks in which the adversary imitates complementarity with classical resources in which the outcomes of measurements in each basis are preassigned (see [195] and next section for details on this kind of attack). Interestingly, BB84-like protocols can be improved to assure "the best possible protection quantum theory can afford" [195], by exploiting the

Code	State	Implementation	ξ
v_1	(1,0,0,0)	$\|t,H\rangle$	4.195 ± 0.001
v_2	(0,1,0,0)	$\|t,V\rangle$	4.269 ± 0.002
v_7	(1,1,1,1)	$\|p,D\rangle$	4.379 ± 0.001
v_{11}	(1,0,1,0)	$\|p,H\rangle$	4.440 ± 0.002
v_{15}	(1,0,0,1)	$\|\psi_1\rangle = \frac{1}{\sqrt{2}}(\|t,H\rangle + \|r,V\rangle)$	4.260 ± 0.001
v_{16}	(0,1,-1,0)	$\|\psi_3\rangle = \frac{1}{\sqrt{2}}(\|r,H\rangle - \|t,V\rangle)$	4.255 ± 0.002
v_{17}	(0,1,1,0)	$\|\psi_4\rangle = \frac{1}{\sqrt{2}}(\|r,H\rangle + \|t,V\rangle)$	4.199 ± 0.002
v_{18}	(0,0,0,1)	$\|r,V\rangle$	4.300 ± 0.002
v_{19}	(0,0,1,0)	$\|r,H\rangle$	4.334 ± 0.003
v_{20}	(1,1,0,0)	$\|t,D\rangle$	4.411 ± 0.001
v_{24}	(1,0,0,-1)	$\|\psi_2\rangle = \frac{1}{\sqrt{2}}(\|t,H\rangle - \|r,V\rangle)$	4.246 ± 0.001
ρ_{25}		$\frac{13}{16}\|\psi_1\rangle\langle\psi_1\| + \frac{1}{16}\sum_{j=2}^{4}\|\psi_j\rangle\langle\psi_j\|$	4.31 ± 0.08
ρ_{26}		$\frac{5}{8}\|\psi_1\rangle\langle\psi_1\| + \frac{1}{8}\sum_{j=2}^{4}\|\psi_j\rangle\langle\psi_j\|$	4.34 ± 0.09
ρ_{27}		$\frac{7}{16}\|\psi_1\rangle\langle\psi_1\| + \frac{3}{16}\sum_{j=2}^{4}\|\psi_j\rangle\langle\psi_j\|$	4.3 ± 0.1
ρ_{28}		$\frac{1}{4}\sum_{j=1}^{4}\|\psi_j\rangle\langle\psi_j\|$	4.3 ± 0.1

Table 5.3. Experimental results for ξ for 15 quantum states. Notation: $|p\rangle = \frac{|t\rangle+|r\rangle}{\sqrt{2}}$, $|D\rangle = \frac{|H\rangle+|V\rangle}{\sqrt{2}}$. The errors in the results of ξ were deduced from the standard deviation of 50 samples in the 10-second time period.

fact that the Bell [25] and Kochen-Specker (KS) [122] theorems show that the outcomes of quantum measurements do not admit local and noncontextual descriptions, respectively. The extra security provided by the Bell theorem has been extensively investigated [80, 19, 2]. However, this extra security is based on the assumption that the legitimate parties can perform a loophole-free Bell test, something which is beyond the present technological capabilities and is not expected to be an easy task in the future [180]. A similar problem affects recent proposals combining the KS theorem with entanglement [48, 108]. Therefore, it is worth to explore the extra security offered by the KS theorem in situations which do not require entanglement nor composite systems, but only single systems with three or more distinguishable states. For cryptographic purposes, the difference between qubits and systems of higher dimensionality is that, whereas in qubits different basis are always disjoint, from qutrits onwards different basis may share common elements. Here we investigate the experimental requirements for obtaining the extra security offered by a KS-protected QKD protocol introduced by Svozil [196], based on the properties of the simplest KS set of states [53]. Hence we propose to implement such a protocol by adopting hybrid ququart states encoded in polarization and orbital angular momentum of single photon.

Svozil's protocol

The cryptographic protocol introduced by Svozil in [196] is a variation of BB84 and works as follows: (i) Alice randomly picks a basis from the 9 available in Fig. 5.7, and sends Bob a randomly chosen state of that basis. (ii) Bob, independently from Alice, picks a basis at random from the 9 available, and measures the system received from Alice. (iii) Bob announces his bases over a public channel, and Alice announces those events in which the state sent belongs to the measured basis. Therefore, the probability of adopting the same basis is 1/9. (iv) Alice and Bob exchange some of the remaining matching outcomes over a

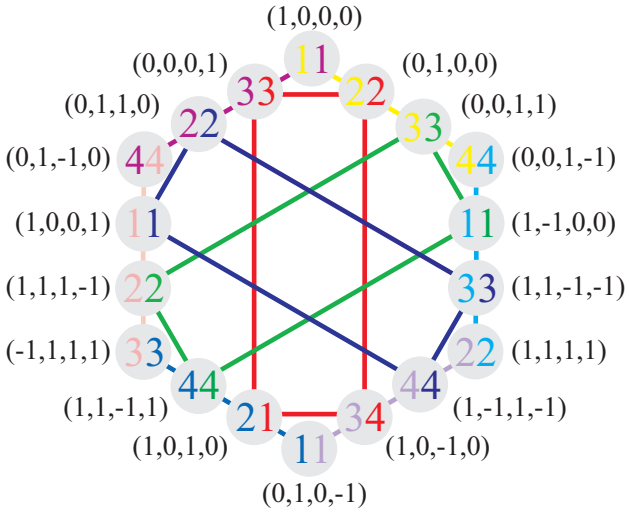

Figure 5.7. The protocol is based on a KS set of 18 states which can be grouped in 9 bases represented by 9 colors. Every state belongs to two different bases. No set of 18 balls can have all the properties required to imitate the KS set; at least two balls must have different symbols. Therefore, the imitation can be detected.

public channel to ensure that nobody has spied their quantum channel. (v) Alice and Bob encode the four outcomes by using four different symbols. As a result, for each successful exchange Bob and Alice share a common random key.

The advantage of this protocol over BB84 is that it is protected by the KS theorem against attacks in which the adversary replaces the quantum system with a classical one. These attacks can be described using a classical toy model [195, 196] in which, in step (i), Alice is actually picking one of 9 differently colored eyeglasses (instead of a basis), and picking a ball with two color symbols in it (instead of a state) from an urn. Each one of the 9 differently colored eyeglasses only allows her to see one of the 9 different colors. To reproduce the quantum predictions: (*a*) each of the balls must have one symbol $S_i \in \{1, 2, 3, 4\}$ written in two different colors chosen among the 18 possible pairs of colors. Her choice of eyeglass decides which symbols Alice can see. (*b*) All colors are equally probable and, for a given color, the four symbols are equally probable. In step (ii), Bob is actually picking one of 9 differently colored eyeglasses and reading the corresponding symbol. A classical strategy like this one can successfully imitate the quantum part of BB84 (see [195] for details), but not the protocol described above. The reason is that the requirements (*a*) and (*b*) cannot be satisfied simultaneously. Fig. 5.7 shows how to prepare 18 balls with the minimum number of balls not having the same symbol.

Experimental requirements

As shown in Fig. 5.7, the minimum number of balls not having the same symbol is 2 out of 18. A ball attack can be detected only in those runs in which Alice and Bob pick differently colored eyeglasses. Therefore, for the set in Fig. 5.7, the trace of such an attack will be a $\frac{2}{18}$ probability of Alice picking a symbol such that the corresponding interlinked symbol (seen only with differently colored eyeglasses) is different. As a consequence, to demonstrate that the experimental results cannot actually be imitated with balls, and experimentally certify the extra security of this KS-based QKD protocol, we need an experimental probability w of

wrong state identification, defined as the probability that Bob makes a wrong identification of the state sent by Alice when Bob has successfully measured in a correct basis, of $w < \frac{1}{9} \approx 0.111$.

Set	Logic	E	**Setup b**		
			PSI	QWP	MC
I	1000 | 0100 0011 | 001-1				$\pi/4$
III	1111 | 1-11-1 10-10 | 010-1				$\pi/4$
IV	-1111 | 11-11 1010 | 010-1	√	√	$\pi/4$	0
IX	01-10 | 0110 1000 | 0001	√	√	$\pi/4$	0

Set	Logic	E	**Setup c**			
			PSI1	PSI2	MC	Waveplate
II	1111 | 11-1-1 1-100 | 001-1				$\pi/4$	HWP $\pi/8$
V	1001 | 01-10 111-1 | -1111	√ √	√	√	$\pi/4$	HWP $\pi/8$
VI	1001 | 0110 11-1-1 | 1-11-1	√		√	0	QWP $\pi/4$
VII	111-1 | 11-11 0011 | 1-100	√		√	0	QWP $\pi/4$
VIII	0001 | 1010 10-10 | 0100					HWP $\pi/8$

Table 5.4. The ququart states that compose the KS set are divided in 9 basis and encoded in polarization and orbital angular momentum degrees of freedom. For each basis are reported the experimental settings of the analysis stage. The column E identifies the entangled states of the two degrees of freedom.

Implementation using polarization-OAM encoded ququarts

Here we propose a scheme for the experimental implementation of the KS-protected QKD protocol. To test its feasibility, we need to prepare the 18 states, measure each of them in two different bases, and obtain an average value of w over the 18×2 possibilities. The condition which must be fulfilled is $w < 0.111$, which corresponds to a mean fidelity value of the transmission of the state of $F = 0.889$. In addition, to check that any intercept and resend strategy causes a disturbance, one should be able to measure what happens when the states are measured in the wrong basis. While in the correct basis the probabilities for the four possible outcomes are (in the ideal case) 0, 0, 0, and 1, in the wrong basis they are either 0, 0, $\frac{1}{2}$, and $\frac{1}{2}$, or 0, $\frac{1}{4}$, $\frac{1}{4}$, and $\frac{1}{2}$.

Svozil's protocol uses 9 sets of four-dimensional states defining a 18-state KS set. We propose encoding four-dimensional quantum states by exploiting hybrid qudits in

polarization and OAM subspace, denoted as o_1, spanned by states with OAM eigenvalue $l = \pm 1$. The logic ququart basis can be re-written as:

$$\{|1\rangle, |2\rangle, |3\rangle, |4\rangle\} \rightarrow \{|H, +1\rangle, |H, -1\rangle, |V, +1\rangle, |V, -1\rangle\}, \tag{5.15}$$

The OAM equivalent of the basis $|H\rangle$ and $|V\rangle$ is defined as $|h\rangle = \frac{1}{\sqrt{2}}(|+1\rangle + |-1\rangle)$ and $|v\rangle = \frac{i}{\sqrt{2}}(|+1\rangle - |-1\rangle)$. Finally, the $\pm 45°$ angle "anti-diagonal" and "diagonal" linear polarizations OAM equivalent will be $|a\rangle = (|h\rangle + |v\rangle)/\sqrt{2}$ and $|d\rangle = (|h\rangle - |v\rangle)/\sqrt{2}$. It is convenient to work with Laguerre-Gauss laser modes ($LG_{0,\pm 1}$) as OAM eigenstates since, in this case, the states ($|h\rangle$,$|v\rangle$,$|a\rangle$,$|d\rangle$) will result as the Hermite-Gauss modes ($HG_{1,0}$,$HG_{0,1}$) along the axes and rotated by 45° (see Chapter 2). This feature allows us to easily transform the states by an astigmatic laser mode converter [23]. By choosing a bidimensional subspace of OAM we avoid detrimental effects on the state due to the radial contribution in the free propagation and Gouy-phases associated to different OAM values. According to the previous definitions, a state (a_1, a_2, a_3, a_4) of the KS set is implemented as

$$a_1|H, +1\rangle + a_2|H, -1\rangle + a_3|V, +1\rangle + a_4|V, -1\rangle. \tag{5.16}$$

The coefficients a_i for each state are shown in Table I, along with the settings needed to analyze each basis.

Generation.—Fig. 5.8 shows the optical schemes for the generation and detection of any ququart state of the KS set. The generation of the states can be achieved by adopting a SPDC source of pair of photons, as in Fig. (5.8-**a**), where we consider a collinear generation of couples $|H\rangle|V\rangle$, where one of the two photons acts as a trigger for the heralded generation of a single photon to be sent to the experimental setup. The manipulation of the OAM degree of freedom can be achieved by adopting a q-plate with topological charge $q = 1/2$. In order to generate all the states of the KS set, it is sufficient to exploit a technique based on the probabilistic quantum transferrer $\pi \rightarrow o_1$ described in [150]. The OAM eigenmodes produced in this way are not exactly *LG* modes but *HyGG* ones [113]. Since some of the detection schemes are based on the properties of Laguerre-Gaussian modes, this fact will lead, in some cases, to a detection efficiency of around 80%. Thus in order to avoid noise due to different OAM order contributions, is sufficient to insert in the detection stage (see Fig.5.8) a q-plate and a single mode fiber connected to the detector.

Measurement of the KS bases.—The bases involved in the KS set have different structures as shown in Table I. They can be classified in three groups, depending on whether they are composed of separable, entangled (between polarization and OAM) or both separable and entangled states.

The detection setup consists of schemes (b) and (c). Their components are a Polarizing Sagnac Interferometer with a Dove prism (PSI) [188], an cylindrical lens Mode Converter (MC) [23] (see Chapter 2), and a Laguerre-Gauss mode Sorter (LGS) [206]. The PSI consists of a Sagnac interferometer with a polarising beam splitter as input-output gate and a Dove prism that intercepts the two counterpropagating beams and can be rotated around the optical axes. This scheme allows, under appropriate conditions, to transform an entangled state into a separable one. In this case, the prism must be rotated in order to add a phase shift of $\Delta\phi = \pi/2$ between $|H\rangle$ and $|V\rangle$ ($\alpha = \pi/8$ in Fig. 6.2). For example, the states of basis IV are transformed into $(|L, a\rangle, |L, d\rangle, |R, +1\rangle, |R, -1\rangle)$. The MC consists of two cylindrical lenses (with the same focal length f) at distance $f/\sqrt{2}$. It allows us to convert the HG states ($|a\rangle$,$|d\rangle$) into ($|+1\rangle$,$|-1\rangle$) and, if rotated by 45° along the optical axes, to convert ($|h\rangle$,

$|v\rangle$) into ($|+1\rangle, |-1\rangle$) [23]. The LGS consists of a Mach-Zehnder interferometer with a Dove Prism in each arm. The two prisms are rotated by $\beta = \pi/4$ one respect to the other. A phase plate ($\psi = \pi/2$) in one of the two arms allows us to send $|+1\rangle$ and $|-1\rangle$ in the two different output ports of the Mach-Zehnder. States belonging to sets $I - III - IV - IX$ can be analyzed by adopting the scheme reported in Fig. 6.2-**b** with some slight modifications related to the specific basis to be measured. The scheme in Fig. 6.2-**c** leads to the analysis of bases $II - V - VI - VII - VIII$. All the details on the settings of the different measurement devices are in Table I.

Conclusions

In this chapter we described two experiments on fundamental quantum mechanics focused on the study of contextual correlations in four dimensional systems. Both experiments have been based on the photonic implementation of exclusivity graphs. The graph of the first experiment represented a task in which quantum mechanics gives an advantage respect to classical mechanics and there exist no post quantum theory which can do it better. By exploiting hybrid ququarts we reported the violation of a non-contextual inequality which certify the quantum advantage. The second experiment has been realized in collaboration with Stockholm University and reports the first experimental implementation of a KS set of quantum tests. We first demonstrated the unique power of this KS set for solving a task avoiding the problem of state initialization (Rome experiment). This is done by showing that, for 28 different quantum states encoded in the orbital angular momentum and polarization degrees of freedom of single photons, the KS set provide an impossible-to-beat solution. Then (Stockholm experiment) maximally contextual quantum correlations have been generated by performing compatible sequential measurements of the polarization and path of single photons. In the last section of the chapter we reported an experimental proposal for a quantum cryptographic protocol protected by KS contextuality and based again on hybrid ququarts.

Our results pave the way for further developments that may include implementing higher dimensionality KS sets [115] and portable KS sets in integrated photonic circuits [173, 168, 184, 185]. Other developments that could be pursued in future work are device-independent security based on contextuality [48, 108] and state-independent quantum correlations with computational power [8].

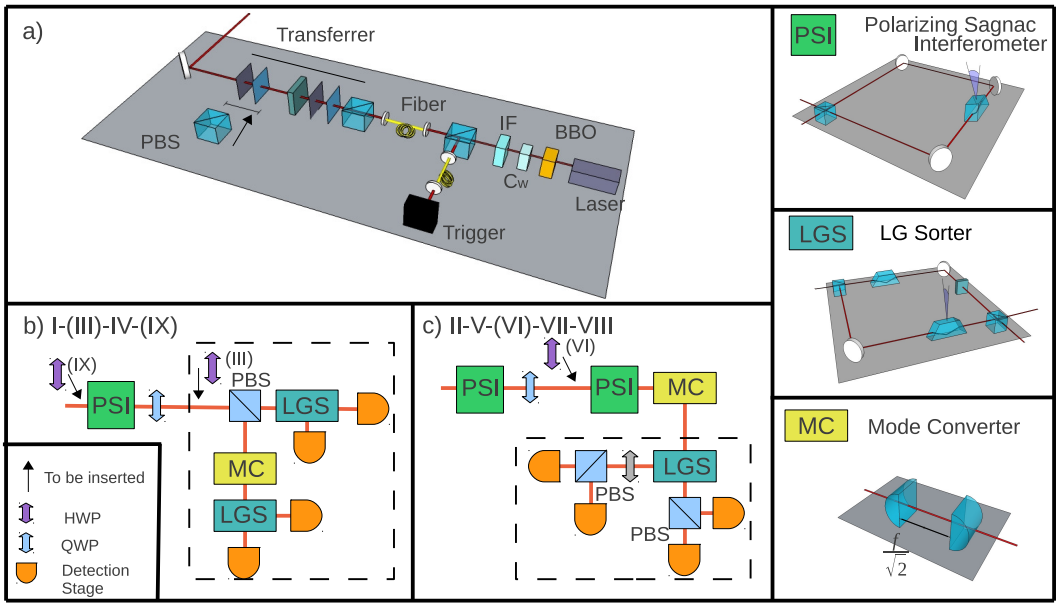

Figure 5.8. a) Setup for the generation of ququart states: one of the two photons emitted by SPDC acts as a trigger, while the other one is sent to a polarizing beam splitter (PBS), wave plates and a quantum transferrer based on the q-plate in order to generate the desired ququart. **b)** Setup for the analysis of bases (I-III-IV-IX): the setup in the dotted rectangle analyzes the four states of basis I; basis III can be measured by inserting a half wave plate (HWP) at $\pi/8$ before the PBS. A polarizing Sagnac interferometer (PSI) and a quarter wave plate are needed to analyze bases IV and IX (adding an HWP before the PSI). **c)** Setup for the analysis of bases (II-V-VI-VII-VIII): The part in the dotted rectangle is suitable to sort the four states of all the bases (the grey wave plate can be a HWP or a QWP depending on the particular basis as shown in Table I); this part is sufficient to analyze basis VIII. Basis II can be analyzed by adding a mode converter (MC). Using a PSI before the MC makes it possible to analyze bases VI (adding a HWP) and VII. Finally, the states of basis V can be sorted by an additional PSI and QWP. The pictures in the three boxes on the right represent the Sagnac interferometer, the LG mode sorter, and the cylindrical lens mode converter, respectively. The detection stage consists of a q-plate, a single mode fiber and a detector.

Chapter 6

Mutually unbiased bases for six-dimensional photonic quantum systems

The "complementarity" of different observables of a same physical system is one of the basic features of the quantum world [33]. Mathematically, complementary observables are described by noncommuting Hermitian operators whose sets of eigenstates form different bases in the Hilbert space that are said to be "mutually unbiased" (MUBs). This expression refers to the fact that the overlap (or inner product) of any pair of states belonging to different bases is the same [77].

In quantum cryptography, complementary observables and the associated MUBs are the core of all protocols proposed for secure quantum key distribution, starting from BB84 protocol and its extension to three qubit bases [22]. As we have seen in Chapter 1 the "no cloning theorem" implies that Alice and Bob can always recognize a possible eavesdropper attack by detecting the associated disturbance introduced in the system. In particular, the adoption of MUBs for encoding the information is known to maximize this disturbance allowing one to recognize the attack most effectively [97]. In quantum state tomography, MUBs play a crucial role because they correspond to the optimal choice of the measurements to be performed in order to obtain a full reconstruction of the density matrix.

Given a Hilbert space of dimension d, an important problem is to find the maximum number of MUBs that can be defined simultaneously. Although for spaces of prime-power dimensions there exist several methods to find a maximal set of $d + 1$ MUBs [172], this problem remains in general hitherto unsolved [15, 27]. Dimension six, in particular, has been widely investigated in the last few years [28, 39, 40, 177] because it is the lowest one for which the problem is still open.

Different experimental approaches have been recently adopted to implement complete sets of MUBs for state reconstruction in photonic systems in Hilbert spaces of dimensions $d = 2, 3, 4, 5, 7, 8$[95][136]. However, since in $d = 6$ no complete set of MUBs is known, this case has never been experimentally investigated hitherto.

In this chapter we demonstrate the generation of MUBs in dimension $d = 6$ by exploiting two different approaches. In the first case we prepare and analyze all states of three MUBs in a hybrid space obtained by combining the polarization and a given three dimensional subspace of the OAM. In our second experiment, we prepare and test the same set of MUBs in a by exploiting only the OAM of the photon. The needing of high fidelity in the MUBs

generation led us to develop a novel holographic method for OAM qudits generation. Indeed, MUBs are very sensitive to the generation fidelity and relatively small imperfections are immediately visible in the MUBs cross overlaps. A high fidelity is also crucial to exploit MUBs for quantum cryptography.

The results here presented are published in [V. D'Ambrosio, F. Cardano, E. Karimi, E. Nagali, E. Santamato, L. Marrucci, F. Sciarrino, *Test of mutually unbiased bases for six-dimensional photonic quantum systems*, Sci. Rep. 3, 2726 (2013)].

6.1 Mutually unbiased bases.

Let A and B be two operators in a d-dimensional Hilbert space, with orthonormal eigenbases $\{|a_i\rangle\}$ and $\{|b_i\rangle\}$ respectively. Eigenstates of these observables are said to be mutually unbiased [211, 77] if

$$|\langle a_i|b_j\rangle|^2 = \frac{1}{d}, \quad \forall\, i, j \in \{1, ..., d\}. \tag{6.1}$$

Such operators are also called mutually complementary, or maximally noncommutative, since given any eigenstate of one, the outcome resulting from a measurement of the other is completely undetermined. In a d-dimensional Hilbert space a pair of MUBs can always be found. Indeed, let $\{|a_i\rangle\}$ be the computational basis,

$$\{|a_i\rangle\} = \{|0\rangle, |1\rangle, ..., |d-1\rangle\}\,. \tag{6.2}$$

A discrete Fourier transform can be then used to define the following dual basis, which is mutually unbiased to the previous one:

$$|b_i\rangle = \frac{1}{\sqrt{d}} \sum_{j=0}^{d-1} \omega_d^{ij} |a_j\rangle \tag{6.3}$$

where $\omega_d = \exp(\mathrm{i}2\pi/d)$, and the non-italic i denotes the imaginary unit (not to be confused with the index i). The pair of operators associated to these bases, often named $\hat{Z}$ and $\hat{X}$ reminiscent of the Pauli operators, provides an algebraic complete set of observables that fully parametrizes the physical degree of freedom described by the Hilbert space: all other operators acting on this space are product of powers of $\hat{Z}$ and $\hat{X}$ [77].

An open issue concerns the maximal number of MUBs that can be found in a d-dimensional space; in the specific case when d is equal to a prime number or to a prime power, a maximal set of $d + 1$ MUBs does exist [77]. This set is also "complete", in the sense that by projective measurements over its states $(d-1)(d+1) = d^2 - 1$ independent real parameters can be obtained, which are exactly the number of parameters needed for full density matrix reconstruction [211]. A complete set of MUBs can be found using several methods, i.e., the Galois Field, the Heisenberg-Weyl group, Hadamard matrices, etc. (for a review see [77, 172]). However, in the general case of composite dimensions that are not prime powers such as $d = 6, 10, 12, ...$, all these methods fail [10]. On the base of extensive numerical simulations, it has been conjectured that complete sets of MUBs do not exist in this case [45, 101], although such conjecture hitherto has not been rigorously proven. A minimum number of MUBs that is known to exist in such cases is given by $p^k + 1$, where p^k is the lowest factor in the prime decomposition of the number d [119]. For instance, in the $d = 6$ case, three MUBs can be easily constructed, but no evidence for the existence of a fourth basis that is unbiased with the first three has ever been found.

The Hilbert space $\mathcal{H}^6$ of a 6D system can be always factorized in the direct product of a 2D and a 3D space, i.e.,

$$\mathcal{H}^6 = \mathcal{H}^2 \otimes \mathcal{H}^3. \tag{6.4}$$

Both these Hilbert subspaces possess complete sets of MUBs, $\left\{|m_i^\alpha\rangle\right\}$ and $\left\{|n_j^\beta\rangle\right\}$, containing respectively three and four bases. Although the states of these bases can be combined to form twelve different separable bases for the space $\mathcal{H}^6$, which can be used for a complete tomography of the qusix state, only sets with three MUBs can be constructed. A possible choice is given by the following three bases:

$$\begin{aligned} I &= \{|m_i^1\rangle \otimes |n_j^1\rangle\} \\ II &= \{|m_i^2\rangle \otimes |n_j^2\rangle\} \\ III &= \{|m_i^3\rangle \otimes |n_j^3\rangle\} \end{aligned} \tag{6.5}$$

where $i \in \{1, 2\}$ and $j \in \{1, 2, 3\}$; an explicit matricial expression of states that we consider is reported in the Appendix B. It can be immediately seen that any other basis obtained introducing the fourth one $\left\{|n_j^4\rangle\right\}$ of the space $\mathcal{H}_3$ would not be mutually unbiased with the others, since it is missing a different basis in $\mathcal{H}_2$. This set of 18 product states cannot be extended by any other vector in $\mathcal{H}_6$, even if entangled states are considered [144]; moreover if a complete MUB set in $d = 6$ existed, then only one among the seven bases therein could be composed of product states, while all others must be entangled [143].

6.2 OAM encoding and the holographic technique.

We now define a 3D subspace O in OAM as that spanned by the three eigenvectors $\{|+1\rangle, |0\rangle, |-1\rangle\}$ where we are omitting the subscript "*oam*". These states can be taken to define the logical basis O_1 of a photonic qutrit in the Hilbert space O. A second basis in O that is mutually unbiased with the logical one can be obtained as the Fourier-transform one $O_2 = \{|\alpha_1\rangle, |\alpha_2\rangle, |\alpha_3\rangle\}$ defined as in Eq. (6.3). Explicitly, we have $|\alpha_1\rangle = (|-1\rangle + |0\rangle + |1\rangle)/\sqrt{3}, |\alpha_2\rangle = (|-1\rangle + \omega|0\rangle + \omega^2|+1\rangle)/\sqrt{3}, |\alpha_3\rangle = (|-1\rangle + \omega^2|0\rangle + \omega|+1\rangle)/\sqrt{3}$, where $\omega = \omega_3 = \exp(i2\pi/3)$ and we have used the identity $\omega^4 = \omega$. The other two bases of a maximal set of MUBs in O are then defined as follows: $O_3 = \{|\beta_1\rangle, |\beta_2\rangle, |\beta_3\rangle\}$ with $|\beta_1\rangle = (|-1\rangle+\omega|0\rangle+\omega|1\rangle)/\sqrt{3}, |\beta_2\rangle = (|-1\rangle+\omega^2|0\rangle+|+1\rangle)/\sqrt{3}, |\beta_3\rangle = (|-1\rangle+|0\rangle+\omega^2|+1\rangle)/\sqrt{3}$ and $O_4 = \{|\gamma_1\rangle, |\gamma_2\rangle, |\gamma_3\rangle\}$ with $|\gamma_1\rangle = (|-1\rangle + \omega^2|0\rangle + \omega^2|1\rangle)/\sqrt{3}, |\gamma_2\rangle = (|-1\rangle + \omega|0\rangle + |+1\rangle)/\sqrt{3}, |\gamma_3\rangle = (|-1\rangle + |0\rangle + \omega|+1\rangle)/\sqrt{3}$.

As shown in Eq. (6.5), in order to construct three MUBs in the 6D hybrid space, we will only need the first three bases O_1, O_2, O_3. The intensity and phase profiles of the nine OAM qudits belonging to these three MUBs are shown in Fig. 6.1.

Let us now discuss the experimental method we adopted for the generation (and detection) of these nine states, and of all other OAM qudits in this work. As we have seen in Chapter 2, arbitrary optical field transverse modes can be obtained by diffraction of an input Gaussian TEM_{00} mode on a SLM programmed for displaying a prescribed hologram (also known as "kinoform"), that is the pattern determining the phase retardation experienced by the input wave in diffraction. The main problem is that the SLM is a phase-only optical element, while to obtain arbitrary OAM modes we need to be able to tailor both the phase and the amplitude transverse profiles of the outgoing field. This can be obtained by modulating both the shape and contrast of the kinoform fringes. To determine the kinoform, we initially tried some of the most commonly used methods [12], but found that they often give rise to a

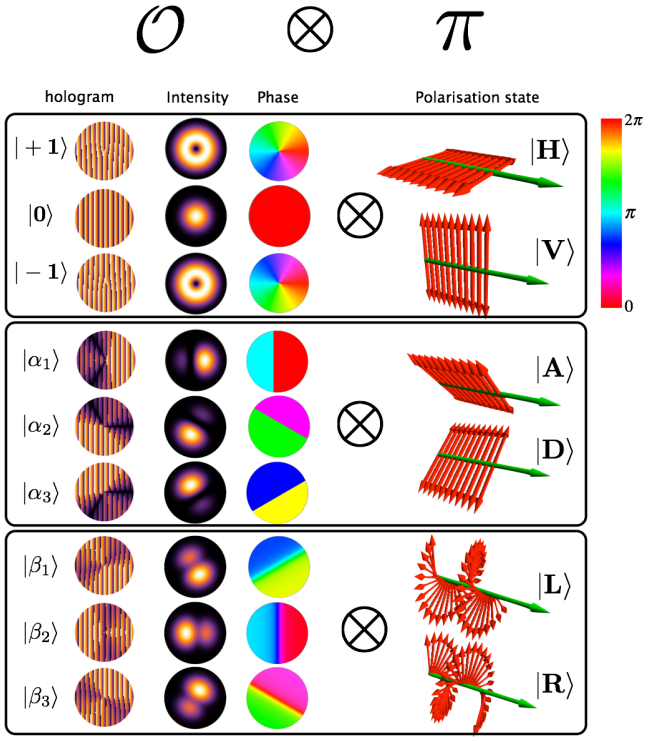

Figure 6.1. MUBs for hybrid photonic qusix encoding: Representation of quantum states with dimension $d = 6$ obtained from the direct product of a three-dimensional subspace O of OAM and the two-dimensional space π of polarization. The three main boxes correspond to the three MUBs. On the left side, the intensity and phase distributions of each OAM spatial mode and the corresponding generating kinoform are shown. On the right side the polarization states are illustrated graphically by showing the optical electric field orientation in space at a given time.

non-negligible "cross-talk", i.e., nonzero overlaps between different states of the same basis, and to significant unbalances in the overlaps of each state of a given basis with the states of other bases. In other words, the generation fidelity of these methods was not good enough for our purposes. For this reason, we developed an holographic method that is specifically optimized in the fidelity.

Holographic technique

Let us first assume that the input field is a plane wave. Our goal is to obtain in the first order of diffraction a prescribed optical field $\mathcal{A}e^{i\Phi}$, $\mathcal{A}$ and Φ being the optical field normalized amplitude and phase, respectively. A straightforward calculation [35] shows that such optical field is obtained in the far field if the kinoform phase modulation has the following expression:

$$\mathcal{M} = \mathrm{Mod}\left[\left(\Phi - \pi\mathcal{I} + \frac{2\pi x}{\Lambda}\right), 2\pi\right]\mathcal{I} \tag{6.6}$$

where Λ is the grating period that fixes the diffraction angle, $\mathcal{I} = \left(1 + \mathrm{sinc}^{-1}(\mathcal{A})/\pi\right)$, in which sinc^{-1} stands for inverse of $\mathrm{sinc}(x) = \sin(x)/x$ function in the domain $[-\pi, 0]$, and Mod is the modulo function that gives the remainder after division of the first argument by the second. The inverse of sinc function was evaluated numerically by the Newton method, with an accuracy of seven digits.

By this method we calculated the kinoforms needed to generate the nine OAM states of the first three MUBs of the OAM qutrit. The resulting hologram patterns are shown in Fig. 6.1. It can be seen that these kinoforms include only an azimuthal dependence, since the OAM state definition ignores the radial coordinate. This implies that the same kinoforms can also be used with a Gaussian input beam instead of a plane wave and only the radial profile of the diffracted wave will be affected, while the OAM state will remain the same. Moreover, we do not need to finely adjust the input beam waist of the Gaussian beam.

We note that the holograms defined by Eq. (6.6) generate ideally exact modes in the far field, so that the expected overlap between states belonging to the same basis vanishes identically and that between states belonging to different MUBs is $1/3$ in the qutrit space (and hence it will be $1/6$ in the qusix space, after combining with polarization). As mentioned, this is not the case for other commonly used holographic methods. For example, numerical simulations based on the method reported in Ref. [129] yielded mean state fidelities of 100%, 88.5% and 84.5% for the three OAM qutrit bases. This corresponds to 6% and 7.7% of mean cross-talk between states belonging to the last two bases. Moreover, the overlap between states of different MUBs is found to vary between 21% and 48%, depending on the state pair. These fidelity problems are absent in our method. More details about the performances of the holographic method used in this work are reported in [35].

6.3 Hybrid qusix encoding and characterization.

Our first experimental implementation of qusix photonic states has been achieved by combining the bi-dimensional space π of polarization and the 3D subspace O of OAM in single photons. The logical basis I of quantum states in dimension six has been hence implemented as follows(see Fig. 6.1):

$$I = \{|H,-1\rangle, |H,0\rangle, |H,+1\rangle, |V,-1\rangle, |V,0\rangle, |V,+1\rangle\} \tag{6.7}$$

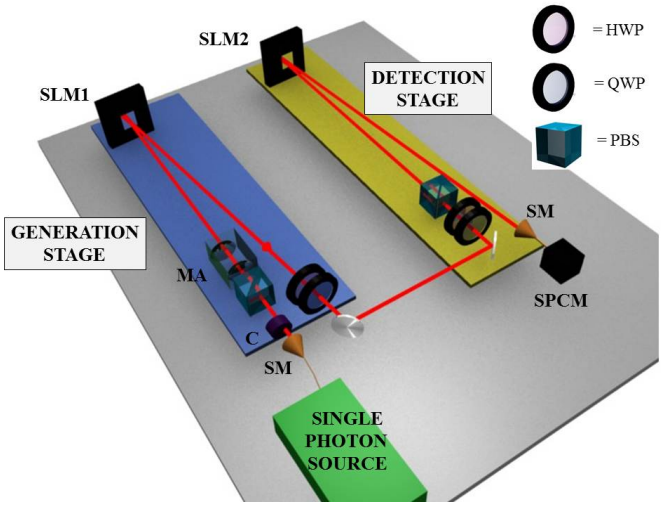

Figure 6.2. Sketch of experimental setup for generating and testing photonic MUBs in dimension six. The polarization state is controlled by suitable sequences of wave plates, while the OAM mode is controlled by SLMs and single-mode fibers. Legend: SM - single-mode fiber; C - polarization compensation waveplates; HWP - half-wave plate; QWP - quarter-wave plate; MA - radial mode adjustment lens set; SLM - spatial light modulator; SPCM - single-photon counter module.

Following Eq. (6.5), a second basis II, unbiased with the first, is obtained by combining the diagonal $|D\rangle$ and antidiagonal $|A\rangle$ polarization states with the OAM qudits of basis O_2. The third basis of the set of MUBs was finally obtained by combining the circular polarization states with the OAM third basis O_3.

In order to experimentally generate these hybrid qusix states we employed the setup shown in Fig. 6.2. Single photons generated by the setup described in section 2.4.2 are sent through a polarizing beam splitter (PBS) (polarization qubit initialization) and, after adjusting the radial-mode size by a pair of lenses (MA), to a first reflecting spatial light modulator (SLM1) which generates the desired OAM qutrit state. The hologram kinoform displayed on the SLM1 for each OAM state to be generated, in the first-order diffraction, is shown in Fig. 6.1. After SLM1, a half wave-plate (HWP) and a quarter wave-plate (QWP) are used to write the polarization qubit in the photon. Hence we are able to generate any hybrid qusix that is a product of a qutrit and a qubit.

The qusix-carrying photon is then sent to the detection stage. This stage is composed of a polarization analysis set (HWP, QWP and a PBS) and a second spatial light modulator (SLM2) for converting in diffraction the OAM state to be detected back into a Gaussian mode. The photon is finally coupled to a single mode fiber, to filter only this Gaussian mode, connected to a single-photon counter module (SPCM). To eliminate the Gouy phase-shift effects between different OAM eigenstates occurring in free propagation, an imaging system (not shown in the figure) has been included to image the screen of SLM1 onto the SLM2. All waveplates and SLMs were computer-controlled so as to allow for a fully automatic generation and measurement procedure. With this setup, it is possible to perform a projective measurement upon every possible separable state of polarization and OAM.

As a first test, we verified the MUBs properties by generating each qusix $|\psi_i\rangle$ among the 18 states of the MUBs and then projecting it onto all the 18 states $|\psi_j\rangle$. Figure 6.3 shows the resulting measured probability distribution $P_{ij} = |\langle\psi_j|\psi_i\rangle|^2$, compared to the theoretical

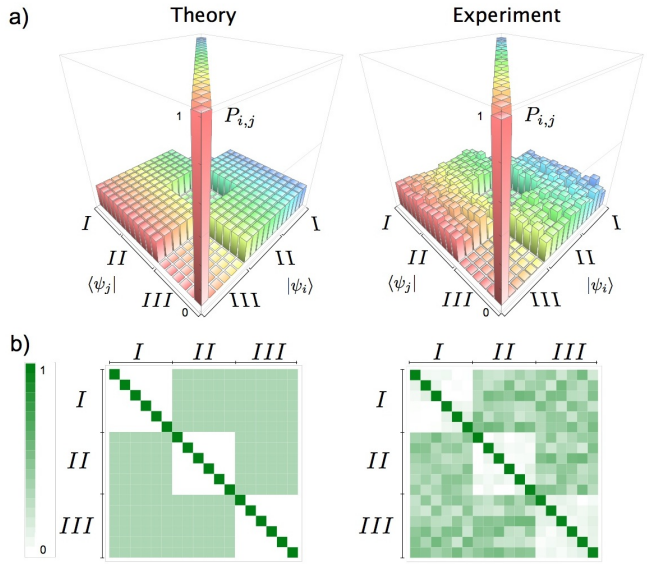

Figure 6.3. Experimental analysis of hybrid qusix photonic states: Probability distribution resulting from all 18×18 projections of each state within the three MUBs over all the others, comparing theoretical and experimental values. According to theoretical predictions, we expect that the 18×18 matrix can be divided into nine 6×6 blocks A_n^m, where the two indices $m, n \in$ {I,II,III} label generation and detection bases, respectively. Blocks that correspond to projection of one basis over itself ($m = n$) should be diagonal, i.e., $(A_m^m)_{i,j} = \delta_{ij}$. Other blocks, whose values represent the overlap between states belonging to two different bases, should be flat, i.e., $(A_n^m)_{i,j} = 1/6$, for $m \neq n$.

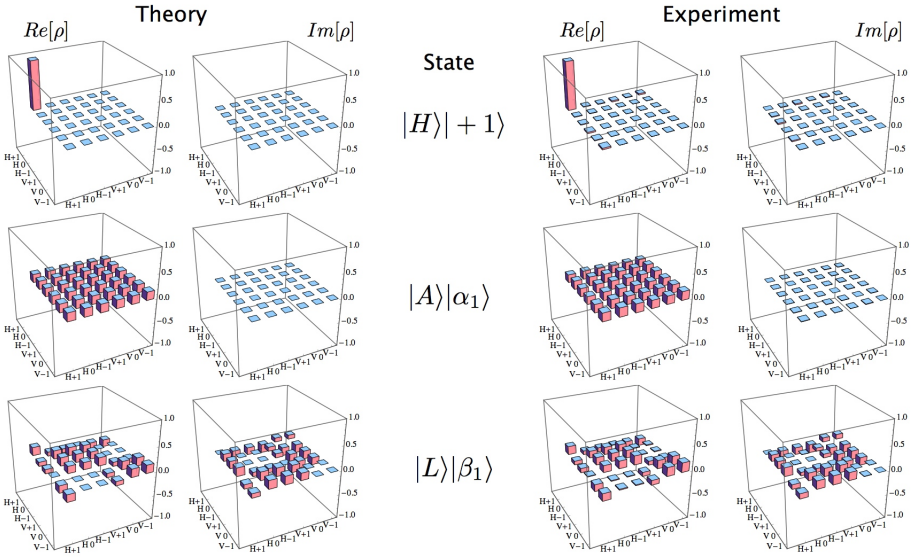

Figure 6.4. Quantum tomography of hybrid qusix photonic states: Density matrices associated to states of each of the three MUBs have been fully reconstructed by projections over all the 72 states obtained by direct product of the three MUBs of the 2D polarization space π and the four ones of the 3D OAM subspace O. Here we show one state for each MUB. Experimental and theoretical matrices are reported for comparison.

one P'_{ij}. For a quantitative comparison, we used the similarity parameter $S = \frac{\left(\sum_{i,j}\sqrt{P_{ij}P'_{ij}}\right)^2}{\sum_{i,j}P_{ij}\sum_{i,j}P'_{ij}}$, which is a natural generalization of the fidelity used to compare two wavefunctions, finding $S = (99.19 \pm 0.04)\%$. As a second check of the quality of our hybrid qusix states, we reconstructed the density matrix of all the 18 states by quantum state tomography. Since we lack a complete set of MUBs in dimension six, we performed measurements in all possible product states obtained combining the three MUBs of the polarization space π and the four MUBs in the OAM space O, for a total of 72 projections. In Table 6.1, the resulting experimental fidelities of the 18 MUBs states are reported. The overall mean fidelity was $\bar{F} = (98.51 \pm 0.04)\%$. Moreover, Figure 6.4 shows the reconstructed density matrices compared to the theoretical ones for three representative qusix states, one for each MUB considered here.

6.4 Pure-OAM qusix encoding and characterization.

Our second experimental implementation of qusix photonic states has been based on the OAM space only. Although the hybrid approach offer some advantages (as we have seen in the previous chapters), an encoding in OAM is in principle suitable of extension to arbitrary dimensionality and enables the generation of any kind of state, including the entangled ones which, for hybrid encoding, would need a more complex experimental setup. To define a 6D Hilbert space, we adopted the following OAM eigenstates as logical basis:

$$I = \{|-3\rangle, |-2\rangle, |-1\rangle, |1\rangle, |2\rangle, |3\rangle\}. \tag{6.8}$$

The three MUBs were still defined starting from the tensor products of a 2D and a 3D spaces, as given in Eq. (6.5). More details about the resulting states of the three bases I, II, III are given in Appendix B.

The experimental setup used for generating and testing the states of the MUBs is the same as in the hybrid qusix case (see Fig. 6.2), but with the polarization optics set so as to keep a fixed polarization everywhere. Figure 6.5 shows the intensity and phase profile of the 18 OAM modes which form the three MUBs. In Figure 6.6, the theoretical and experimental probability distributions for all combinations of state preparation and detection are reported. The similarity between the two distributions is $S = (99.06 \pm 0.04)\%$ while the mean fidelity over the 18 states is $F = (98.78 \pm 0.08)\%$. Comparing this result with the hybrid case, in which only OAM states in dimension 3 were generated, we find that the fidelity of the OAM generation does not decrease rapidly with the dimensions. Hence, the holograhic method used in this work promises to be suitable for the high-fidelity generation of OAM photonic qudits with very large dimension d.

Discussion

In summary, we have reported the experimental implementation of a non-extendable set of three MUBs for a photonic quantum system of dimension six by two different approaches. In the first, the qusix states have been implemented via a hybrid scheme based on polarization-orbital angular momentum encoding. All the 18 states belonging to the MUBs are in this case separable states of two different degrees of freedom. The demonstration of MUBs with high fidelity and unbiasedness has required the development of a new method for determining the hologram to be visualized in the spatial light modulator. The second demonstrated

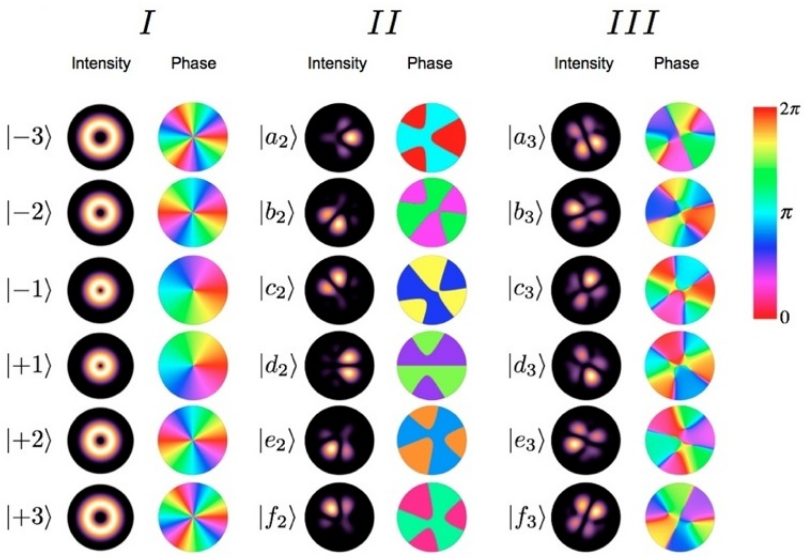

Figure 6.5. Graphical representation of all 18 states of the three selected MUBs, in the case of pure OAM 6D encoding. For each state, both the intensity and phase patterns are shown.

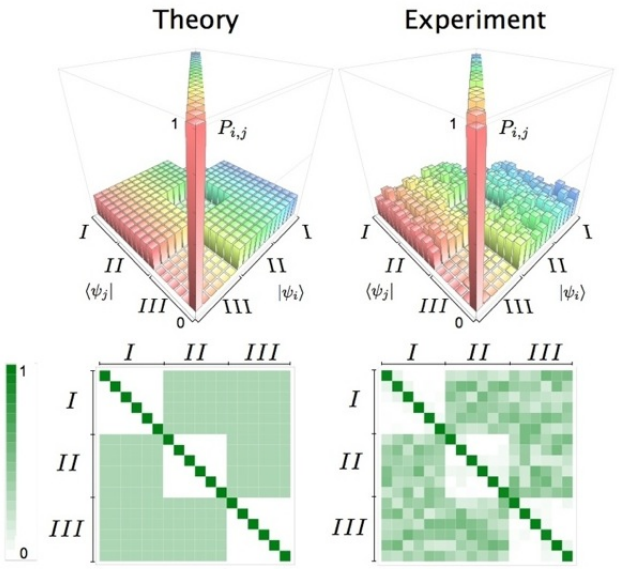

Figure 6.6. Theoretical and experimental probability distributions for an experiment based on pure OAM 6D encoding in which all the 18×18 combinations of generated/detected states belonging to the three MUBs are tested.

Basis	State	Fidelity
I	$\|H\rangle\|+1\rangle$	0.986 ± 0.002
	$\|H\rangle\|0\rangle$	0.982 ± 0.002
	$\|H\rangle\|-1\rangle$	0.986 ± 0.002
	$\|V\rangle\|+1\rangle$	0.988 ± 0.002
	$\|V\rangle\|0\rangle$	0.980 ± 0.002
	$\|V\rangle\|-1\rangle$	0.983 ± 0.002
II	$\|A\rangle\|\alpha_1\rangle$	0.989 ± 0.001
	$\|A\rangle\|\alpha_2\rangle$	0.981 ± 0.002
	$\|A\rangle\|\alpha_3\rangle$	0.986 ± 0.002
	$\|D\rangle\|\alpha_1\rangle$	0.989 ± 0.001
	$\|D\rangle\|\alpha_2\rangle$	0.982 ± 0.002
	$\|D\rangle\|\alpha_3\rangle$	0.980 ± 0.002
III	$\|L\rangle\|\beta_1\rangle$	0.981 ± 0.002
	$\|L\rangle\|\beta_2\rangle$	0.981 ± 0.002
	$\|L\rangle\|\beta_3\rangle$	0.979 ± 0.002
	$\|R\rangle\|\beta_1\rangle$	0.977 ± 0.002
	$\|R\rangle\|\beta_2\rangle$	0.972 ± 0.002
	$\|R\rangle\|\beta_3\rangle$	0.970 ± 0.002
	Average Fidelity	0.9851 ± 0.0004

Table 6.1. Experimental fidelities measured for all 18 qusix hybrid states that characterize the three chosen MUBs.

approach was based on a quantum encoding in the photon OAM space only, at a fixed polarization. The generation of a set of MUBs with high fidelity was again verified and this method is suitable for a convenient extension to higher dimensionality. The techniques we have demonstrated here can find application in fundamental tests of quantum mechanics, quantitative wave-particle duality, detection of entanglement [194], quantum key distribution [58], tests of quantum complementarity, logical indeterminacy and the so called “mean king’s problem” [201][81].

Chapter 7

Conclusions and perspectives

In the past years, qubits have been the fundamental resource for both theoretical and experimental investigation in quantum information and fundamental quantum mechanics. Being a simple two dimensional quantum system they provided an optimal tool for the study of fundamental properties of nature like entanglement or the realization of protocols like quantum teleportation. Despite this succes, qubits present some limitations which have become clear when, in the last decades, much attention has been spent in the investigation of their multidimensional extension, a quantum d-dimensional systems known as "qudit". High dimensional quantum sistems indeed opened new perspective in many fields and in particular in fundamental quantum mechanics [114, 202, 120] where they allow to study quantum contextual correlations and in quantum information [58, 86, 126] where high dimensionality assures for instance larger alphabets for information encoding and higher security in quantum key distribution protocols.

Although qubits are often implemented by exploiting the polarization state of single photons, this degree of freedom is not suitable for qubits implementation. The experimental realization of higher dimensional systems requires multiphoton states, or, as alternative resource, different degrees of freedom of a single photon like frequency, path or orbital angular momentum (OAM). This last degree of freedom is related to the spatial profile of a paraxial light beam and is defined in an infinite dimensional Hilbert space. Therefore a qudit can be encoded in a OAM subspace of single photons or, as alternative, in the product Hilbert space of polarization and orbital angular momentum spaces (hybrid encoding).

This thesis is the result of three years of research activity performed in the quantum optics group of "Sapienza" University focused on the study of single photon qudits and their applications in several fields like quantum communication, quantum cryptography, fundamental quantum mechanics and metrology.

A first part of this research have been devoted to the development of new tools for the manipulation of optical orbital angular momentum. As a first result we developed an optical device which is able to transfer information between the polarization and a bi-dimensional subspace of OAM in a deterministic way (transferrer)[69]. This device allows to easily encode (and decode) two qubits stored in a single photon. Moreover we investigated the optimization conditions for one of the most widely used devices for OAM manipulation, the spatial light modulator, a liquid crystal device which allows to add a phase profile to an optical beam [38].

A second part of the research has been devoted to the study of the properties of hybrid qudits encoded in polarization and OAM. The fundamental experimental tool for hybrid

qubits generation has been the so called q-plate, a liquid crystal cell which allows to couple polarization and orbital angular momentum. In particular we individuated a bi-dimensional subspace of a hybrid ququart space whose vectors are invariant under physical rotations around the photon's propagation direction. These states have been then exploited as qubits in order to realize an alignment-free quantum communication between two distant users [70]. We also demonstrated that these rotational invariant qubits are robust against beam perturbations hence they could provide a useful resource for realistic long distance quantum communication scenario. As well as rotational invariant qubits are insensitive to rotations along the propagation axis, it is also possible to exploit other hybrid ququart subspaces in order to enhance such rotations. Hence we focused on this class of hybrid qubits and developed the concept of "photonic gear". This device allow to enhance the precision of a polarization based roll angle measurement thanks to a super resolved Malus law and could be exploited as a new resource both in metrology and quantum metrology.

The third part of this thesis project have been focused on fundamental quantum mechanics experiments based on high dimensional systems. By exploiting q-plates and the transferrer just developed we designed two experiments in order to study contextual correlations. In the first experiment we realized a task that has been proven to be the simplest task in which quantum mechanics gives an advantage, based on contextual correlations, respect to classical mechanics and no post-quantum theories can do it better [149]. In the second experiment, realized in collaboration with Stockholm University, we reported the first experimental realization of a Kochen-Specker set of quantum tests [68].

Finally, as application of qudits to quantum cryptography, we proposed an experiment based on hybrid ququarts in which quantum contextuality offers an extra protection against attacks in which complementarity is imitated with classical resources [50]. Moreover we experimentally realized a non-extendable set of three mutually unbiased bases (MUBs) in dimension six with two different physical systems by exploiting both hybrid encoding and pure orbital angular momentum states superporitions. In order to exploit MUBs for cryptographic purposes or quantum state tomography, the correponding qudits have to be experimentally implemented with high fidelity. This goal led us to develop a novel holographic technique that allows to generate, in principle, qudits of arbitrary dimension.

The results here presented open several perspectives that can be investigated in the near future.

Alignment-free quantum communication for instance has been demonstrated only on distances of several meters in the laboratory. In order to make rotational invariant qubits a fundamental resource for real world satellite based quantum communication, further tests are needed. In particular align-free quantum communication over long distances and an experimental test on resilience to atmospheric turbulences are two challenges that can be addressed in the next future.

A possible perspective in metrology is the enhancement of the current best technologies for roll angle measurements by exploiting the photonic gear based on hybrid qubits.

The holographic technique developed for the generation of MUBs in dimension six can be exploited for instance in the experimental implementation of quantum information protocols based on qudits or as a tool for high dimensional state reconstruction via quantum state tomography.

Finally, in fundamental quantum mechanics qudits are the keystone for several further investigations. Indeed, here we have shown that it is possible to exploit ququarts to violate non-contextual inequalities which holds for classical systems. Moreover we experimentally realized the simplest task in which this quantum advantage is impossible to beat by any

post-quantum theory. However, for a generic experiment, post-quantum correlations can outperform the results of quantum mechanics. The fact that this post-quantum advantage has never been experimentally observed leads to a natural question on what is the principle that limits quantum correlations to be as they are. Although this is still an open question, qudits will surely be the fundamental tool for further investigations.

Appendix A

Photonic Gears: Technical details

Photonic gears and their precision

In this note, we describe the theoretical details behind the bound given in Eq. (6) of the main article for the precision of the hybrid SAM-OAM photonic gear concept.

Quantum Fisher information including photon-losses and non-unitary conversion efficiency

The maximum amount of information which can be extracted about a parameter θ from an N-photon state $\varrho_N(\theta)$ is quantified by the quantum Fisher information $F_N = F_N(\varrho_N(\theta))$. In particular, the minimal uncertainty in the estimation of θ from measurements on $\varrho_N(\theta)$, optimized over all possible measurements, satisfies the so-called quantum Cramér-Rao (QCR) bound:

$$\Delta\theta_{\min} \geq (\nu F_N)^{-1/2}, \tag{A.1}$$

where ν is the number of measurement runs with copies of $\varrho_N(\theta)$. In addition, the bound can always be saturated in the asymptotic limit of large ν, for a suitable estimation function.

When $\varrho_N(\theta)$ is obtained from a unitary evolution $\mathcal{U}_\theta = e^{-\imath\mathcal{G}\theta}$ of a pure state $|\psi_N(\theta)\rangle = \mathcal{U}_\theta|\psi_N^0\rangle$, the quantum Fisher information takes the simple θ-independent form: $F_N(\varrho_N(\theta)) = F_N(\psi_N^0) = 4\langle\psi_N^0|(\Delta\mathcal{G})^2|\psi_N^0\rangle$, where $\Delta\mathcal{G} = \mathcal{G} - \langle\psi_N^0|\mathcal{G}|\psi_N^0\rangle$. For the hybrid SAM-OAM strategy with single photons, each photon is prepared in the state $|\Psi_{\rm G}^{\rm C}\rangle$. Then, in the absence of losses, the state $|\psi_N^0\rangle$ is given by the N-photon state $|\Psi_{\rm G}^{\rm C}\rangle^{\otimes N}$. The generator of the rotations around the z axis is $\mathcal{G} = (S_{\rm p}^z + S_{\rm o}^z)/\hbar$, where $S_{\rm p}^z$ and $S_{\rm o}^z$ are are the corresponding polarization and orbital angular momentum operators, respectively. The quantum Fisher information is additive, hence $F_N(|\Psi_{\rm G}^{\rm C}\rangle^{\otimes N}) = NF$, where we have introduced the notation $F = F_1(|\Psi_{\rm G}^{\rm C}\rangle)$. By evaluating the variance of $\mathcal{G}$ over the unperturbed single-photon state $|\Psi_{\rm G}^{\rm C}\rangle$, we obtain the explicit expression $F = 4m^2$ for the Fisher information per photon. This, together with the QCR bound above, gives us precisely bound (4.6) of Chapter 4:

$$\Delta\theta_{\rm G}^{\rm C} \geq \frac{1}{2m\sqrt{\nu N}}. \tag{A.2}$$

Let us now consider the presence of photon losses. The total losses (including those at the detection stage) are quantified by a single transmittivity parameter $0 \leq \eta \leq 1$, and transform the ideal single-photon state $|\Psi_{\rm G}^{\rm C}(\theta)\rangle$ arriving at Bob's station into:

$$\varrho_{\rm G}^{\rm C}(\theta) = \eta|\Psi_{\rm G}^{\rm C}(\theta)\rangle\langle\Psi_{\rm G}^{\rm C}(\theta)| + (1-\eta)|0\rangle\langle 0|, \tag{A.3}$$

where $|0\rangle$ is the vacuum state. Since $\varrho_{\mathrm{G}}^{\mathrm{C}}(\theta)$ is the sum of two terms which correspond to orthogonal subspaces, the quantum Fisher information per photon is

$$F(\varrho_{\mathrm{G}}^{\mathrm{C}}(\theta)) = \eta F(|\Psi_{\mathrm{G}}^{\mathrm{C}}(\theta)\rangle) + (1-\eta)F(|0\rangle) = \eta F. \tag{A.4}$$

Here we have used the fact that $F(|0\rangle) = 0$, since no information can be acquired from the vacuum state. Using the additivity property of the Fisher information, the QCR bound (A.1), the precision in presence of losses is

$$\Delta\theta_{\mathrm{G}}^{\mathrm{C}} \geq \frac{1}{2m\sqrt{\eta\nu N}}. \tag{A.5}$$

That is, the overall effect of photon losses is simply to rescale the total number of photons from νN to $\eta\nu N$.

We conclude by discussing the effect of a non-unitary conversion efficiency of the q-plates. In this case, the action of these devices are described by the following map:

$$\mathcal{Q}(\varrho) = \epsilon\,\mathcal{U}_q\varrho\mathcal{U}_q^{\dagger} + (1-\epsilon)\mathbb{1}_{\pi,q}\varrho\mathbb{1}_{\pi,q}, \tag{A.6}$$

where $\mathcal{U}_q$ is the unitary evolution operator representing a perfect q-plate, and $\mathbb{1}_{\pi,q}$ is the identity operator on the joint polarization-OAM space, and ϵ is the conversion efficiency. The output state of a photon after the encoding, rotation and decoding stages is measured with multimode fibers. The multimode fiber accepts all OAM states, and thus no measurement of the final OAM is performed, corresponding mathematically to the partial trace on the OAM subspace. The output density matrix then reads:

$$\varrho_{\mathrm{G}}^{\mathrm{C}}(\theta) = \epsilon_1\epsilon_2|\Psi_{\mathrm{G}}^{\mathrm{C}}(\theta)\rangle\langle\Psi_{\mathrm{G}}^{\mathrm{C}}(\theta)| + [\epsilon_1(1-\epsilon_2)+(1-\epsilon_1)\epsilon_2]\frac{\mathbb{1}_\pi}{2} + (1-\epsilon_1)(1-\epsilon_2)|\Psi^{\mathrm{C}}(-\theta)\rangle\langle\Psi^{\mathrm{C}}(-\theta)|, \tag{A.7}$$

where $\mathbb{1}_\pi = |1\rangle_{R\,R}\langle 1| + |1\rangle_{L\,L}\langle 1|$, and ϵ_1 and ϵ_2 refer respectively to the conversion efficiencies of Alice's and Bob's q-plates. Finally, we observe that the latter term in $(1-\epsilon_1)(1-\epsilon_2)$ is small for typical efficiencies of the q-plates ($\epsilon_i > 0.9$), and can be neglected. The output state before detection can be then written as:

$$\varrho_{\mathrm{G}}^{\mathrm{C}}(\theta) \simeq V|\Psi_{\mathrm{G}}^{\mathrm{C}}(\theta)\rangle\langle\Psi_{\mathrm{G}}^{\mathrm{C}}(\theta)| + (1-V)\frac{\mathbb{1}_\pi}{2}, \tag{A.8}$$

where $V = \epsilon_1\epsilon_2/[(1-\epsilon_1)(1-\epsilon_2)]$ is the fringe pattern visibility achieved with polarization detection. Evaluating the quantum Fisher information for state (A.8) again in the presence of photon losses, gives the bound for the precision $\Delta\theta^m$:

$$\Delta\theta^m \geq \frac{1}{2mV\sqrt{\eta\nu N}}. \tag{A.9}$$

In principle, η and ϵ display no dependence on q and therefore enter in the precision as just constant factors. In practice, a number of experimental imperfections can cause the two parameters to slightly depend on q. We considered this effect with an heuristic model, which includes a dependence on q in Eq. (A.9) of the form: $V\sqrt{\eta} \to V_0\sqrt{\eta_0}[1-\gamma m^\delta]$. The parameters γ and δ are retrieved by fitting the experimental data, while V_0 and η_0 are the visibility and the efficiency for $q = 0$. For the data shown in Figure 4.5 of Chapter 4, we obtained $\gamma = 0.026 \pm 0.008$ and $\delta = 0.62 \pm 0.07$, showing that the dependence on q is very weak.

Classical Fisher information of the outcomes of polarization measurements

Let us next show that the measurement strategy described in Chapter 4 is indeed the optimal one, reaching the QCR (A.1). We do this first for the ideal case $\eta = 1$ and $V = 1$, and then, below, briefly present the case with experimental imperfections. In the H/V linear polarization basis, the state of each photon arriving at Bob's station reads

$$|\Psi_{\mathrm{G}}^{\mathrm{C}}(\theta)\rangle = \cos(m\theta)|1\rangle_{H,0} + \sin(m\theta)|1\rangle_{V,0}. \tag{A.10}$$

Bob measures each photon in the fixed H/V linear-polarization basis, and obtains a classical outcome x with possible values H or V, distributed according to the conditional probability distribution $p_{\mathrm{G}}^{\mathrm{C}}(x|\theta) = |\langle\Psi_{\mathrm{G}}^{\mathrm{C}}(\theta)\|1\rangle_{x,0}|^2$. From this, the minimum uncertainty he can get is again dictated by the Cramér-Rao (CR) bound $\Delta\theta_{\mathrm{G}}^{\mathrm{C}} \geq (\nu N f)^{-1/2}$, where f is the classical Fisher information per particle associated to the particular measurement strategy[1], defined as

$$f = f(p_{\mathrm{G}}^{\mathrm{C}}(x|\theta)) = \sum_{x=H,V} \frac{1}{p_{\mathrm{G}}^{\mathrm{C}}(x|\theta)} \left(\frac{\partial p_{\mathrm{G}}^{\mathrm{C}}(x|\theta)}{\partial\theta}\right)^2. \tag{A.11}$$

Substituting $p_{\mathrm{G}}^{\mathrm{C}}(H|\theta) = \cos^2(m\theta)$ and $p_{\mathrm{G}}^{\mathrm{C}}(V|\theta) = \sin^2(m\theta)$ into (A.11), one obtains $f = (2m)^2$. This, in turn, with the CR bound above, directly leads to optimal quantum bound (A.2). In addition, for a suitable estimation function, the bound is always saturated in the limit of $\nu \to \infty$. Hence, the adopted measurement strategy allows Bob and Alice to reveal as much information about θ as allowed by quantum mechanics.

In the presence of experimental imperfections, including photon losses and non-unitary efficiencies for the q-plates [see Eq. (A.8)], the CR bound with polarization measurements is straightforwardly calculated to be:

$$\Delta\theta^m \geq \frac{1}{2mV\sqrt{\eta}\sqrt{\nu N}\sqrt{C(\theta)}}, \tag{A.12}$$

where $C(\theta)$ is the following function:

$$C(\theta) = \frac{\sin(2m\theta)^2}{1 - V^2\cos(2m\theta)^2}. \tag{A.13}$$

Hence, the minimum statistical error exhibits a dependence on the actual value of the angle, and the QCR bound can only be saturated for $\tilde{\theta} = \pi/(4m) + k\pi/(2m)$, with integer k. However, in the next section, we discuss an adaptive protocol that succeeds in saturating the QCR bound for all values of θ.

Coherent states

Here, we show that the estimation protocol works equally well for coherent pulses of average photon number N as for N single photons. That is, for the same measurement strategy, the resulting precision bound is given by (A.2). We discuss explicitly only the ideal case, the case with experimental imperfections follows straightforwardly and gives (A.12). Consider a coherent state $|\mathrm{coh}(\alpha)\rangle_{H,0}$ of generic complex amplitude α as input to Alice's q-plate. The mean photon number is $|\alpha|^2$, and the state has H linear polarization and is prepared in the zero-OAM mode. We can write $|\mathrm{coh}(\alpha)\rangle_{H,0} = D_{H,0}(\alpha)|0\rangle$, where $D_{H,0}(\alpha) = e^{\alpha a_{H,0}^\dagger - \alpha^* a_{H,0}}$ is the displacement operator with amplitude α, $a_{H,0}^\dagger$ and $a_{H,0}$ are the

creation and annihilation operators of a photon in the corresponding mode, respectively, and $|0\rangle$ represents the vacuum state. Alice's q-plate and HWP transform the mode operators as $a^\dagger_{H,0} = \frac{1}{\sqrt{2}}(a^\dagger_{R,0} + a^\dagger_{L,0}) \to \frac{1}{\sqrt{2}}(a^\dagger_{R,-2q} + a^\dagger_{L,2q})$, where $a^\dagger_{R,-2q}$ ($a^\dagger_{L,2q}$) is the creation operator of a photon in the total angular momentum eigenmode of R (L) circular polarization and OAM $-2q$ ($2q$). The operator $a_{H,0}$ undergoes an analogous transformation. Then, using linearity and some simple algebra, one obtains that Alice's station induces the state transformation:

$$|\mathrm{coh}(\alpha)\rangle_{H,0} = D_{H,0}(\alpha)|0\rangle \to D_{R,-2q}(\alpha/\sqrt{2})D_{L,2q}(\alpha/\sqrt{2})|0\rangle = |\mathrm{coh}(\alpha/\sqrt{2})\rangle_{R,-2q}|\mathrm{coh}(\alpha/\sqrt{2})\rangle_{L,2q} = |\Psi^{\mathrm{coh}}_{\mathrm{G}}\rangle, \tag{A.14}$$

where the last equality defines our coherent-state hybrid SAM+OAM states.

Under rotation, $|\Psi^{\mathrm{coh}}_{\mathrm{G}}\rangle$ evolves into $|\Psi^{\mathrm{coh}}_{\mathrm{G}}(\theta)\rangle = \mathcal{U}_\theta|\Psi^{\mathrm{coh}}_{\mathrm{G}}\rangle$, with $\mathcal{U}_\theta = e^{-\imath\mathcal{G}\theta}$, and $\mathcal{G}$ the generator of state rotations defined above. Using that $\mathcal{U}_\theta a^\dagger_{L/V,\pm 2q}\mathcal{U}^\dagger_\theta = e^{\mp im\theta}a^\dagger_{L/V,\pm 2q}$, and analogously for $a_{L/V,\pm 2q}$, we have

$$|\Psi^{\mathrm{coh}}_{\mathrm{G}}(\theta)\rangle = |\mathrm{coh}(e^{im\theta}\alpha/\sqrt{2})\rangle_{R,-2q}|\mathrm{coh}(e^{-im\theta}\alpha/\sqrt{2})\rangle_{L,2q}, \tag{A.15}$$

where as before $m = 2q + 1$. The quantum Fisher information $F_N(|\Psi^G_{\mathrm{coh}}(\theta)\rangle)$ calculated from the probe state $|\Psi^{\mathrm{coh}}_{\mathrm{G}}(\theta)\rangle$ is $F_N(|\Psi^{\mathrm{coh}}_{\mathrm{G}}(\theta)\rangle) = 4\langle\Psi^{\mathrm{coh}}_{\mathrm{G}}(\theta)|(\Delta G)^2|\Psi^G_{\mathrm{coh}}(\theta)\rangle$, leading to the precision

$$\Delta\theta^{\mathrm{coh}}_{\mathrm{G}} \geq \frac{1}{2m\sqrt{\nu|\alpha|^2}}. \tag{A.16}$$

For the particular case when the mean photon number $|\alpha|^2$ is N, bound (A.16) is equal to (A.2).

Next, we show that Bob's polarization measurements are optimal, even for the case of coherent states. To the coherent-pulse, he applies the same decoding transformations as in the single photon strategy: a HWP followed by q-plate of charge q. The output state is

$$|\Psi^G_{\mathrm{coh}}(\theta)\rangle \to |\mathrm{coh}(e^{im\theta}\alpha/\sqrt{2})\rangle_{R,0}|\mathrm{coh}(e^{-im\theta}\alpha/\sqrt{2})\rangle_{L,0} = |\mathrm{coh}(\cos(m\theta)\alpha)\rangle_{H,0}|\mathrm{coh}(\sin(m\theta)\alpha)\rangle_{V,0}, \tag{A.17}$$

As in the single-photon case, he sends output state through a H/V polarizing beam splitter, and detects the conditional probability distribution $p(n_H, n_V|\theta)$ of obtaining n_H horizontally polarized photons and n_V vertically polarized ones with an intensity measurement. The associated classical Fisher information is

$$f(p(n_H, n_V|\theta)) = \sum_{n_H,n_V=0}^{\infty} \frac{1}{p(n_H, n_V|\theta)}\left(\frac{\partial p(n_H, n_V|\theta)}{\partial\theta}\right)^2, \text{ with} \tag{A.18}$$

$$p(n_H, n_V|\theta) = e^{-|\alpha|^2}\frac{(\cos^2(m\theta)|\alpha|^2)^{n_H}(\sin^2(m\theta)|\alpha|^2)^{n_V}}{n_H!n_V!}, \tag{A.19}$$

where the explicit form (A.19) of distribution $p(n_H, n_V|\theta)$ is obtained by expanding the right-hand side of (A.17) in the Fock-state basis. A straightforward calculation shows that the CR bound applied to Fisher information (A.18) coincides exactly with the optimal quantum scaling (A.16). Also, as usual, with a suitable estimator, the bound is saturated in the limit $\nu \to \infty$. Hence, the polarization analysis adopted for single-photon probes is also the optimal measurement strategy for coherent-pulses.

The estimation procedure

Here we describe the technical details of our phase estimation procedure.

A. Bayesian estimator

With the measurement strategy established, an estimator must be used to process the experimental data obtained. The experimental outcomes of $M = \nu \times N$ independent photons can be represented by the string $X = (x_1, \ldots, x_M)$, with $x_i = H$ or V, for $1 \leq i \leq M$. An estimator is a function that maps X into an estimate $\overline{\theta}$ of the actual value θ^*. A suitable choice is given by the Bayesian estimator[39], which is based on Bayes' rule:

$$P(\theta|X)P(X) = P(X|\theta)P(\theta). \tag{A.20}$$

$P(\theta|X)$ is the conditional probability of θ^* being equal to θ given that the observed outcome string is X. This is the desired distribution, as from it both the estimate and its uncertainty can be directly obtained. $P(X|\theta)$ gives the conditional probability of getting X given that the phase is θ. Since the photons are independent, it can be decomposed as

$$P(X|\theta) = \prod_{k=1}^{M} p(x_k|\theta). \tag{A.21}$$

In addition, since the experimental setup is well-characterized, the distributions $p(x_k|\theta)$ with which one can explicitly evaluate (A.21) are known. For instance, for the SAM+OAM states, these are given by

$$p(x_k|\theta) = p_{\mathrm{G}}^{\mathrm{C}}(x_k|\theta) = \begin{cases} \cos^2(m\theta) & \text{if } x_k = H, \\ \sin^2(m\theta) & \text{if } x_k = V, \end{cases} \tag{A.22}$$

for all $1 \leq k \leq M$. In turn, $P(X)$ is the probability of getting X regardless of the value of θ. This can also be explicitly evaluated, as it is defined in terms of $P(X|\theta)$: $P(X) = \int_\Omega d\theta P(X|\theta)$, where Ω is the interval of bijectivity of $P(X|\theta)$ as a function of θ, of length $0 < \mathcal{T} \leq 2\pi$, in which θ^* is known to lie. Finally, $P(\theta)$ is the probability of the phase being θ regardless of the detected outcomes, which is of course unknown. In Bayesian estimation, one simply guesses θ^* based on whatever apriori knowledge. That is, one substitute $P(\theta)$ by $P_{\mathrm{prior}}(\theta)$, which describes this knowledge. When no prior knowledge about θ^* is available, except that it belongs to Ω, one has $P_{\mathrm{prior}}(\theta) = 1/\mathcal{T}$. This, together with rule (A.20) and decomposition (A.21), gives the desired *a-posteriori* distribution:

$$P(\theta|X) = \frac{1}{\mathcal{T}P(X)} \prod_{k=1}^{M} p(x_k|\theta). \tag{A.23}$$

With this, the estimate and its associated mean square statistical error are obtained as

$$\overline{\theta} = \int_\Omega d\theta\, \theta P(\theta|X), \tag{A.24}$$

$$\text{and } \Delta\theta^2 = \int_\Omega d\theta\, (\theta - \overline{\theta})^2 P(\theta|X), \tag{A.25}$$

respectively. This estimation displays the following two convenient properties[40]: (i) It is *locally unbiased*. This means that, in the asymptotic limit of large M, $\overline{\theta}$ converges to the

true value θ^*, for arbitrary θ^* in Ω. (ii) The Bayesian estimator displays phase-independent sensitivity. That is, in the same asymptotic limit, it saturates the Cramér-Rao inequality, for any $\theta^* \in \Omega$. Furthermore, it has been shown[39,41] that the output phase distribution obtained with Bayesian analysis reaches a Gaussian function faster than other approaches, such as Maximum-likelihood estimators, leading to a faster convergence when the sample size is small.

B. Concatenated adaptative estimation strategy

As q increases, the oscillation frequency of distributions (A.22) grows, so that the length of their longest intervals of bijectivity, as functions of θ, decreases with q. Therefore, if the Bayes estimator is directly applied to estimate a phase $\theta^* \in [0, 2\pi)$, the resulting estimate (A.24) will only be defined up to a degeneracy that increases with q. To circumvent this, we adopt an estimation strategy with adaptive concatenated steps. We show here that the maximal number of concatenated steps needed to fully remove any ambiguity in the estimate is only 3. For simplicity, we describe the strategy in the single-photon regime, its extension to the coherent-pulse regime being trivially analogous.

We split the measurements on all $M = \nu N$ of photons into 3 different kinds, each one constituting a step of the strategy. Each step j, for $1 \leq j \leq 3$, consumes M_j photons prepared with $m = m_j$, in such a way that $m_3 > m_2 > m_1$, where $m_j = 2q_j \pm 1$. This guarantees that every consecutive step features a higher sensitivity. Each step j renders an estimate $\overline{\theta}_j$ and an uncertainty $\Delta\theta_j$, calculated respectively through (A.24) and (A.25). Each estimate $\overline{\theta}_j$ is unambiguously defined only over an interval Ω_j of length $\mathcal{T}_j$ equal to half a period of oscillation of distributions (A.22) for $q = q_j$:

$$\mathcal{T}_j = \frac{\pi}{2m_j}. \tag{A.26}$$

In addition, the photons in each j-th step are prepared in the state $|\Psi^G(\xi_j)\rangle = \frac{1}{\sqrt{2}}(e^{i\xi_j}|1\rangle_{R,-2q} + e^{-i\xi_j}|1\rangle_{L,2q})$. The relative phase ξ_j is such that the estimate $\overline{\theta}_{j-1}$ of the previous $(j-1)$-step sits exactly at one of the points of maximal sensitivity of $|\Psi^C_G(\xi_j)\rangle$. That is, for example:

$$\xi_j = \frac{\pi}{4} - m_j\overline{\theta}_{j-1}. \tag{A.27}$$

This condition is always possible to satisfy for $j > 1$, where an estimate $\overline{\theta}_{j-1}$ is available. However, for the first step, unless one has some a-priori knowledge bout θ^*, $\overline{\theta}_1$ is not defined. In this case we simply choose $\xi_1 = 0$. The aim of adapting the phase at each step is two-fold. On the one hand, since this allows us to achieve the maximal angular resolution of each step, it speeds up the asymptotic saturation of the QCR bound. On the other hand, as we discuss below, it breaks the symmetry in distributions (A.22) between m_j and m_{j-1}. This allows us to reduce the potential ambiguities in the estimate by a factor of two per step. For this reason, as we explain next, only three concatenated steps suffice for arbitrary $\theta^* \in [0, 2\pi)$.

For the strategy with phase adaptation, the outcomes of the j-th step are governed by the distributions $p_j(x_k|\theta) = \cos^2[m_j\theta + \xi_j]$, if $x_k = H$, or $p_j(x_k|\theta) = \sin^2[m_j\theta + \xi_j]$, if $x_k = V$. In the first step we always set $m_1 = 1$ (q-plate detuned, corresponding to polarization-only strategy), $\xi_1 = 0$, and $\Omega_1 = [0, \pi/2)$. Since $p_1(x_k|\theta)$ repeat their values four times over $[0, 2\pi)$, the estimate $\overline{\theta}_1 \in \Omega_1$ of this step is four-fold degenerate. The actual value of $\theta^* \in [0, 2\pi)$ may be either $\overline{\theta}_1$, $\pi - \overline{\theta}_1$, $\overline{\theta}_1 + \pi$, or $2\pi - \overline{\theta}_1$. For the second step, apart from taking $m_2 > m_1 = 0$,

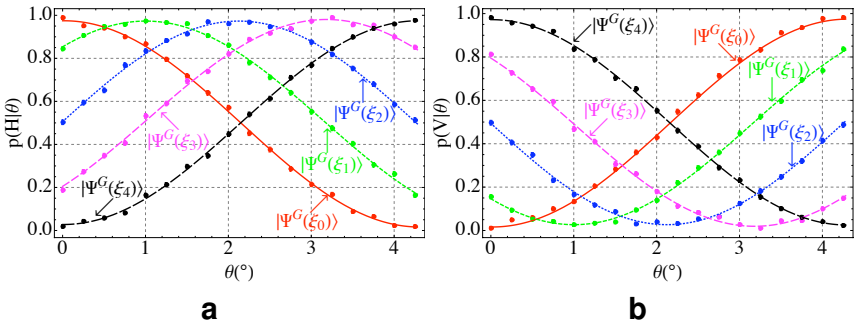

Figure A.1. Experimentally adapting the oscillation phase. In order to optimize the sensitivity for any angle it is necessary to adapt the relative phase ξ in the state $|\Psi_{\rm G}^{\rm C}(\xi)\rangle$. This can be efficiently implemented by rotating the polarization of the input state of an angle ξ by means of a half waveplate. Indeed, a rotation of the input state from $|1\rangle_H$ to $|1\rangle_V$ corresponds to an inversion in the maxima and the minima of the pattern. Here we report the oscillation patterns [(a) $p_{\rm G}^{\rm C}(H|\theta)$ and (b) $p_{\rm G}^{\rm C}(V|\theta)$] obtained with the single-photon photonic gear ($q = 10$ and $m = 2q + 1 = 21$) for different values of initial state phase ξ_i: $\{\xi_0 = 0, \xi_1 = \pi/8, \xi_2 = \pi/4, \xi_3 = 3\pi/8, \xi_4 = \pi/2\}$. Points: experimental data. Curves: corresponding best-fit curves. Error bars in the experimental data are due to the Poissonian statistics of the measured single-photon counts.

with the exact charge determined below, we set ξ_2 in terms of the estimated $\overline{\theta}_1$, as determined by Eq. (A.27), and $\Omega_2 = [\overline{\theta}_1 - \mathcal{T}_2/2, \overline{\theta}_1 + \mathcal{T}_2/2)$, with $\mathcal{T}_2 = \frac{\pi}{2m_2}$ as given by (A.26). Unless $\overline{\theta}_1$ happens to be equal to $\mathcal{T}_2/2$, so that $\xi_2 = \xi_1 = 0$, this phase choice causes two out of the four possible θ's to be consistent with one value of $p_2(x_k|\theta)$ and the other two with another value. This leads to a second estimate $\overline{\theta}_2 \in \Omega_2$ with only a two-fold ambiguity. On the other hand, if $\overline{\theta}_1 = \mathcal{T}_2/2$, the symmetry between $p_1(x_k|\theta)$ and $p_2(x_k|\theta)$ is not broken by this choice. However, one can simply choose $\xi_2 = \xi_1 + \varphi_2 = \varphi_2$, for some suitable φ_2 that is not a multiple of $\mathcal{T}_2/2$. This decreases the angular resolution per probe, but allows one in return to break the symmetry. The third step is analogous to the second one: Apart from $m_3 > m_2$, we set ξ_3 as given by (A.27) and $\Omega_3 = [\overline{\theta}_2 - \mathcal{T}_3/2, \overline{\theta}_2 + \mathcal{T}_3/2)$, with $\mathcal{T}_3 = \frac{\pi}{4m_3}$. Unless $\overline{\theta}_2$ happens to be equal to $\mathcal{T}_3/2$, this leads to a third estimate $\overline{\theta}_3 \in \Omega_3$, without any ambiguity. Thus, arbitrary $\theta^* \in [0, 2\pi)$ are unequivocally estimated by the final estimate $\overline{\theta}_3$.

We next discuss the exact charge values $m_j = 2q_j \pm 1$ used in each step. It is not possible to increase the angular resolution arbitrarily much from step to step. In particular, one must require that

$$\mathcal{T}_j \geq \Delta\theta_{j-1}, \tag{A.28}$$

for all j, so that the regions of bijectivity of $p_j(x_k|\theta)$ are not shorter than the precision of the $(j-1)$-th estimation. Also, we take $M_1 \lesssim M_2^{1/2} \lesssim M_3^{1/4}$. This choice is convenient because, in the asymptotic limit of large $M = M_1 + M_2 + M_3$, it makes M_1 negligible with respect to M_2, and the latter in turn negligible with respect to M_3. So, M_3 tends to M, and the QCR bound is still asymptotically saturated[42,43]. The first uncertainty $\Delta\theta_1$ is such that $\Delta\theta_1 \geq [2m_1\sqrt{M_1}]^{-1} = [2\sqrt{M_1}]^{-1}$. The uncertainty $\Delta\theta_2$ in the second step is such that $\Delta\theta_2 \geq [2\sqrt{m_1^2 M_1 + m_2^2 M_2}]^{-1}$, which is approximately equal to $[2m_2\sqrt{M_2}]^{-1}$ in the limit of large M_2. The latter conditions for $\Delta\theta_1$ and $\Delta\theta_2$, together with (A.28) and (A.26), lead to

$$2q_j + 1 \leq (2q_{j-1} + 1)\pi\sqrt{M_{j-1}}, \tag{A.29}$$

for all j. This relationship tells us that the more we want to increase the angular resolution

(the charge) from step $j-1$ to step j, the higher the precision of step $j-1$ must be, by increasing the number of probes M_{j-1}. Or, equivalently, given fixed numbers of probes M_1, M_2, and M_3, the relationship sets a limit to the maximal jumps in resolution we can take per step. We take the optimal choice

$$2q_j + 1 = \lfloor (2q_{j-1} + 1)\pi \sqrt{M_{j-1}} \rfloor, \tag{A.30}$$

where $\lfloor (2q_{j-1} + 1)\pi \sqrt{M_{j-1}} \rfloor$ stands for the largest integer smaller than $(2q_{j-1} + 1)\pi \sqrt{M_{j-1}}$. In the asymptotic limit of large M, the overall final uncertainty $\Delta\theta_3$ tends to the minimal uncertainty

$$[2\sqrt{m_1^2 M_1 + m_2^2 M_2 + m_3^2 M_3}]^{-1} \sim [2m_3 \sqrt{M}]^{-1}, \tag{A.31}$$

and saturates the QCR bound[42,43].

Also, even though minimal uncertainty (A.31) is in principle independent of θ, experimental imperfections make it divergent for some values of θ^*. The phase-adaptive strategy described above allows one to avoid these divergencies, so that an approximate phase-independent sensitivity is recovered. Furthermore, this adaptive approach does not introduce any modification of the setup, since it requires inserting q-plates with different values, to be switched on and off by electrical tuning, and different linear-polarization states input.

Appendix B

Mutually unbiased bases sets

In dimension $d = 2$, the eigenstates of the three Pauli operators provide a complete set of MUBs, which can be represented by the columns of the following three matrices:

$$\pi_1 = \begin{pmatrix} 1 & 0 \\ 0 & 1 \end{pmatrix},\ \pi_2 = \frac{1}{\sqrt{2}} \begin{pmatrix} 1 & 1 \\ 1 & -1 \end{pmatrix},\ \pi_3 = \frac{1}{\sqrt{2}} \begin{pmatrix} 1 & 1 \\ \mathrm{i} & -\mathrm{i} \end{pmatrix}. \tag{B.1}$$

In $d = 3$, there exist four MUBs. We represent them here as the columns of the following four matrices:

$$O_1 = \begin{pmatrix} 1 & 0 & 0 \\ 0 & 1 & 0 \\ 0 & 0 & 1 \end{pmatrix}, \quad O_2 = \frac{1}{\sqrt{3}} \begin{pmatrix} 1 & 1 & 1 \\ 1 & \omega & \omega^2 \\ 1 & \omega^2 & \omega \end{pmatrix}$$
$$O_3 = \frac{1}{\sqrt{3}} \begin{pmatrix} 1 & 1 & 1 \\ \omega & \omega^2 & 1 \\ \omega & 1 & \omega^2 \end{pmatrix}, O_4 = \frac{1}{\sqrt{3}} \begin{pmatrix} 1 & 1 & 1 \\ \omega^2 & \omega & 1 \\ \omega^2 & 1 & \omega \end{pmatrix}, \tag{B.2}$$

where $\omega = \exp(\mathrm{i}2\pi/3)$.

In $d = 6$, we may construct three MUBs by a direct product of the π_1, π_2, π_3 bases and the corresponding first three bases O_1, O_2, O_3:

$$I = \pi_1 \otimes O_1, \quad II = \pi_2 \otimes O_2, \quad III = \pi_3 \otimes O_3. \tag{B.3}$$

These three 6D bases have the following matrix representation:

$$I = \begin{pmatrix} 1 & 0 & 0 & 0 & 0 & 0 \\ 0 & 1 & 0 & 0 & 0 & 0 \\ 0 & 0 & 1 & 0 & 0 & 0 \\ 0 & 0 & 0 & 1 & 0 & 0 \\ 0 & 0 & 0 & 0 & 1 & 0 \\ 0 & 0 & 0 & 0 & 0 & 1 \end{pmatrix} \tag{B.4}$$

$$II = \frac{1}{\sqrt{6}} \begin{pmatrix} 1 & 1 & 1 & 1 & 1 & 1 \\ 1 & \omega & \omega^2 & 1 & \omega & \omega^2 \\ 1 & \omega^2 & \omega & 1 & \omega^2 & \omega \\ 1 & 1 & 1 & -1 & -1 & -1 \\ 1 & \omega & \omega^2 & -1 & -\omega & -\omega^2 \\ 1 & \omega^2 & \omega & -1 & -\omega^2 & -\omega \end{pmatrix} \tag{B.5}$$

$$III = \frac{1}{\sqrt{6}} \begin{pmatrix} 1 & 1 & 1 & 1 & 1 & 1 \\ \omega & \omega^2 & 1 & \omega & \omega^2 & 1 \\ \omega & 1 & \omega^2 & \omega & 1 & \omega^2 \\ i & i & i & -i & -i & -i \\ i\omega & i\omega^2 & i & -i\omega & -i\omega^2 & -i \\ i\omega & i & i\omega^2 & -i\omega & -i & -i\omega^2 \end{pmatrix} \tag{B.6}$$

The 18 columns of these three matrices give the coefficients of the logical basis superpositions defining the 18 OAM states shown in Fig. 6.5.

Appendix C

Published papers related to this thesis

- V. D'Ambrosio, E. Nagali, C. Monken, S. Slussarenko, L. Marrucci and F. Sciarrino, *Deterministic qubit transfer between orbital and spin angular momentum of single photons.* Optics Letters, 37 (2012)
- V. D'Ambrosio, E. Nagali, S. P. Walborn, L. Aolita, S. Slussarenko, L. Marrucci, F. Sciarrino, *Complete experimental toolbox for alignment-free quantum communication*, Nature Communications 3, 961 (2012)
- V. D'Ambrosio, N. Spagnolo, L. Del Re, S. Slussarenko, Y. Li, L. C. Kwek, L. Marrucci, S. P. Walborn, L. Aolita and F. Sciarrino, *Photonic polarization gears for ultra-sensitive angular measurements*, Nature Communications 4, 2432 (2013)
- E. Nagali, V. D'Ambrosio, F. Sciarrino, A. Cabello, *Experimental Observation of Impossible-to-Beat Quantum Advantage on a Hybrid Photonic System*, Physical Review Leters. 108, 090501 (2012)
- V. D'Ambrosio, I. Herbauts, E. Amselem, E. Nagali, M. Bourennane, F. Sciarrino, A. Cabello, *Experimental implementation of a Kochen-Specker set of quantum tests*, Physical Review X 3, 011012 (2013)
- A. Cabello, V. D'Ambrosio, E. Nagali, F. Sciarrino, *Hybrid ququart-encoded quantum cryptography protected by Kochen-Specker contextuality*, Physical Review A 84, 030302 (2011)
- R. Bowman, V. D'Ambrosio, E. Rubino, O. Jedrkiewicz, P. Di Trapani, M.J. Padgett, *Optimisation of a low cost SLM for diffraction efficiency and ghost order suppression* European Physical Journal Special Topics 199, 149 (2011)
- V. D'Ambrosio, F. Cardano, E. Karimi, E. Nagali, E. Santamato, L. Marrucci, F. Sciarrino, *Test of mutually unbiased bases for six-dimensional photonic quantum systems*, Scientific Reports 3, 2726 (2013)

Bibliography

[1] Abouraddy, A. F., Yarnall, T., Saleh, B. E. A., and Teich, M. C. Violation of bell's inequality with continuous spatial variables. Phys. Rev. A, **75** (2007), 052114.

[2] Acin, A., Brunner, N., Gisin, N., Massar, S., Pironio, S., and Scarani, V. Device-independent security of quantum cryptography against collective attacks. Physical Review Letters, **98** (2007), 230501.

[3] Afek, I., Ambar, O., and Silberberg, Y. High-noon states by mixing quantum and classical light. Science, **328** (2010), 879.

[4] Aiello, A., Oemrawsingh, S. S. R., Eliel, E. R., and Woerdman, J. P. Nonlocality of high-dimensional two-photon orbital angular momentum states. Physical Review A, **72** (2005), 052114.

[5] Allen, L., Beijersbergen, M. W., Spreeuw, R. J. C., and Woerdman, J. P. Orbital angular momentum of light and the transformation of laguerre-gaussian laser modes. Physical Review A, **45** (1992), 8185.

[6] Amselem, E., Danielsen, L. E., López-Tarrida, A. J., Portillo, J. R., Bourennane, M., and Cabello, A. Experimental fully contextual correlations. Physical Review Letters, **108** (2012), 200405.

[7] Amselem, E., Rådmark, M., Bourennane, M., and Cabello, A. State-independent quantum contextuality with single photons. Physical Review Letters, **103** (2009), 160405.

[8] Anders, J. and Browne, D. E. Computational power of correlations. Physical Review Letters, **102** (2009), 050502.

[9] Aolita, L., Gallego, R., Acin, A., Chiuri, A., Vallone, G., P., M., and Cabello, A. Fully nonlocal quantum correlations. Physical Review A, **85** (2011), 032107.

[10] Archer, C. There is no generalization of known formulas for mutually unbiased bases. arXiv:quant-ph/0312204v1, (2003).

[11] Arends, F., Ouaknine, J., and Wampler, C. W. On searching for small Kochen-Specker vector systems. Graph-Theoretic Concepts in Computer Science, (2011), 23.

[12] Arrizón, V., Ruiz, U., Carrada, R., and González, L. Pixelated phase computer holograms for the accurate encoding of scalar complex fields. JOSA A, **24** (2007), 3500.

[13] Aspect, A., Dalibard, J., and Roger, G. Experimental test of Bell's inequalities using time-varying analyzers. Physical Review Letters, **49** (1982), 1804.

[14] Aspelmeyer, M. and et al. Long-distance free-space distribution of quantum entanglement. Science, **301** (2003), 621.

[15] Bandyopadhyay, S., Boykin, P. O., Roychowdhury, V., and Vatan, F. A new proof for the existence of mutually unbiased bases. Algorithmica, **34** (2002), 512.

[16] Barnett, S. M. Optical angular-momentum flux. Journal of Optics B, **4** (2002), 7.

[17] Barnett, S. M. and Zambrini, R. Resolution in rotation measurements. Journal of Modern Optics, **53** (2006), 613.

[18] Barnum, H., Beigi, S., Boixo, S., Elliott, M., and Wehner, S. Local quantum measurement and no-signaling imply quantum correlations. Physical Review Letters, **104** (2011), 140401.

[19] Barrett, J., Hardy, L., and Kent, A. Computational power of correlations. Physical Review Letters, **95** (2005), 010503.

[20] Bartlett, S. D., Rudolph, T., and Spekkens, R. W. Reference frames, superselection rules, and quantum information. Reviews of Modern Physics, **79** (2007), 555.

[21] Bartosik, H., Klepp, J., Schmitzer, C., Sponar, S., Cabello, A., Rauch, H., and Hasegawa, Y. Experimental test of quantum contextuality in neutron interferometry. Physical Review Letters, **103** (2009), 040403.

[22] Bechmann-Pasquinucci, H. and Gisin, N. Incoherent and coherent eavesdropping in the six-state protocol of quantum cryptography. Physical Review A, **59** (1999), 4238.

[23] Beijersbergen, M., Allen, L., van der Veen, H., and Woerdman, J. Astigmatic laser mode converters and transfer of orbital angular momentum. Optics Communications, **96** (1993), 123.

[24] Beijersbergen, M., Coerwinkel, R., Kristensen, M., and Woerdman, J. Helical-wavefront laser beams produced with a spiral phaseplate. Optics Communications, **112** (1994), 321.

[25] Bell, J. et al. On the einstein-podolsky-rosen paradox. Physics, **1** (1964), 195.

[26] Bell, J. S. On the problem of hidden variables in quantum mechanics. Reviews of Modern Physics, **38** (1966), 447.

[27] Bengtsson, I. Three ways to look at mutually unbiased bases. arXiv:quant-ph/0610216v1, (2006).

[28] Bengtsson, I. and et al. Mutually unbiased bases and Hadamard matrices of order six. Journal of Mathematical Physics, **48** (2007), 052106.

[29] Bennett, C. H. and Brassard, G. Proceedings of IEEE International Conference on Computers, Systems, and Signal Processing,Bangalore, India, (1984), 175.

[30] Bernet, S., Jesacher, A., Furhapter, S., Maurer, C., and M., R.-M. Quantitative imaging of complex samples by spiral phase contrast microscopy. Optics Express, **14** (2006), 3792.

[31] Beth, R. A. Mechanical detection and measurement of the angular momentum of light. Physical Review, **50** (1936), 115.

[32] Bialynicki-Birula, I. and Bialynicka-Birula, Z. Canonical separation of angular momentum of light into its orbital and spin parts. Journal of Optics, **13** (2011), 063014.

[33] Bohr, N. Albert Einstein: Philosopher-Scientist. Discussions with Einstein on Epistemological Problems in Atomic Physics, in P. A. Schilpp, (1970).

[34] Boileau, J., Gottesman, D., Laflamme, R., Poulin, D., and Spekkens, R. Robust polarization-based quantum key distribution over a collective-noise channel. Physical Review Letters, **92(1)** (2004), 17901.

[35] Bolduc, E., Bent, N., Santamato, E., Karimi, E., and Boyd, R. W. Exact solution to simultaneous intensity and phase encryption with a single phase-only hologram. Optics Letters, **38** (2013), 3546.

[36] Bonato, C., Tomaello, A., Da Peppo, V., Naletto, G., and Villoresi, P. Feasibility of satellite quantum key distribution. New. Journal of Physics, **11** (2009), 040517.

[37] Bourennane, M., Eibl, M., Gaertner, S., Kurtsiefer, C., Cabello, A., and Weinfurter, H. Decoherence-free quantum information processing with four-photon entangled states. Physical Review Letters, **92** (2004), 107901.

[38] Bowman, R., D'Ambrosio, V., Rubino, E., Jedrkiewicz, O., Di Trapani, P., and Padgett, M. J. Optimisation of a low cost slm for diffraction efficiency and ghost order suppression. Eur. Phys. J. Special Topics, **199** (2011), 149.

[39] Brierley, S. and Weigert, S. Maximal sets of mutually unbiased quantum states in dimension 6. Physical Review A, **78** (2008), 042312.

[40] Brierley, S. and Weigert, S. Constructing mutually unbiased bases in dimension six. Physical Review A, **79** (2009), 052316.

[41] Brukner, Č., Żukowski, M., Pan, J., and Zeilinger, A. Bell's inequalities and quantum communication complexity. Physical Review Letters, **92** (2004), 127901.

[42] Brukner, i. c. v., Kim, M. S., Pan, J.-W., and Zeilinger, A. Correspondence between continuous-variable and discrete quantum systems of arbitrary dimensions. Phys. Rev. A, **68** (2003), 062105.

[43] Brunner, N., Cavalcanti, D., Pironio, S., Scarani, V., and Wehner, S. Bell nonlocality. arXiv:1303.2849.

[44] Bruss, D., DiVincenzo, D. P., Ekert, A., Fuchs, C. A., Macchiavello, C., and Smolin, J. A. Optimal universal and state-dependent quantum cloning. Physical Review A, **57** (1998), 2368.

[45] Butterley, P. and Hall, W. Numerical evidence for the maximum number of mutually unbiased bases in dimension six. Physics Letters A, **369** (2007), 5.

[46] Cabello, A. How many questions do you need to prove that unasked questions have no answers? International Journal of Quantum Information, **4** (2006), 55.

[47] Cabello, A. Experimentally testable state-independent quantum contextuality. Physical Review Letters, **101** (2008), 210401.

[48] Cabello, A. Proposal for revealing quantum nonlocality via local contextuality. Physical Review Letters, **104** (2010), 220401.

[49] Cabello, A. Simple explanation of the quantum violation of a fundamental inequality. Physical Review Letters, **110** (2013), 060402.

[50] Cabello, A., D'Ambrosio, V., Nagali, E., and Sciarrino, F. Hybrid ququart-encoded quantum cryptography protected by kochen-specker contextuality. Physical Review A, **84** (2011), 030302.

[51] Cabello, A., Danielsen, L., Lopez-Tarrida, A., and Portillo, J. Basic exclusivity graph in quantum correlations. Physical Review A, **88** (2013), 032104.

[52] Cabello, A., Danielsen, L. E., López-Tarrida, A., and Portillo, J. Optimal preparation of graph states. Physical Review A, **83** (2011), 042314.

[53] Cabello, A., Estebaranz, J. M., and García-Alcaine, G. Bell-Kochen-Specker theorem: A proof with 18 vectors. Physics Letters A, **212** (1996), 183.

[54] Cabello, A., Severini, S., and Winter, A. (non-) contextuality of physical theories as an axiom. arXiv:1010.2163, (2010).

[55] Cabello, A., Severini, S., and Winter, A. (Non-)Contextuality of physical theories as an axiom. arXiv:1010.2163, (2010).

[56] Cardano, F., Karimi, E., Slussarenko, S., Marrucci, L., de Lisio, C., and Santamato, E. Polarization pattern of vector vortex beams generated by q-plates with different topological charges. Applied Optics, **51** (2012), C1.

[57] Caruso, F., Bechmann-Pasquinucci, H., and Macchiavello, C. Robustness of a quantum key distribution with two and three mutually unbiased bases. Physical Review A, **72** (2005), 032340.

[58] Cerf, N. J., Bourennane, M., Karlsson, A., and Gisin, N. Security of quantum key distribution using d-level systems. Physical Review Letters, **88** (2002), 127902.

[59] Chigrinov, V. G., Kozenkov, V. M., and Kwok, H.-S. Photoalignment of Liquid Crystalline Materials: Physics and Applications. Wiley Publishing (2008).

[60] Chiribella, G., D'Ariano, G., and Perinotti, P. Informational derivation of quantum theory. Physical Review A, **84** (2011), 012311.

[61] Cirel'son, B. Quantum generalizations of bell's inequality. Letters in Mathematical Physics, **4** (1980), 93.100.

[62] Clauser, J., Horne, M., Shimony, A., and Holt, R. Proposed experiment to test local hidden-variable theories. Physical Review Letters, **23** (1969), 880.

[63] Collins, D., Gisin, N., Linden, N., Massar, S., and Popescu, S. Bell inequalities for arbitrarily high-dimensional systems. Physical Review Letters, **88** (2002), 040404.

[64] Cory, D. G., Fahmy, A. F., and Havel, T. F. Ensemble quantum computing by NMR spectroscopy. Proc. Nat. Acad. Sci., **94** (1997), 1634.

[65] Courtial, J., Dholakia, K., Robertson, D. A., Allen, L., and Padgett, M. J. Violation of a bell inequality in two-dimensional orbital angular momentum state-spaces. Physical Review Letters, **80** (1998), 3217.

[66] Dakić, B. and Brukner, v. Quantum theory and beyond: Is entanglement special? in *Deep Beauty. Understanding the Quantum World through Mathematical Innovation*, (2011), 365.

[67] D'Ambrosio, V., Cardano, F., Karimi, E., Nagali, E., Santamato, E., Marrucci, L., and Sciarrino, F. Test of mutually unbiased bases for six-dimensional photonic quantum systems. Scientific Reports, **3** (2013), 2726.

[68] D'Ambrosio, V., Herbauts, I., Amselem, E., Nagali, E., Bourennane, M., Sciarrino, F., and Cabello, A. Experimental implementation of a kochen-specker set of quantum tests. Physical Review X, **3** (2013), 011012.

[69] D'Ambrosio, V., Nagali, E., Monken, C., Slussarenko, S., Marrucci, L., and Sciarrino, F. Deterministic qubit transfer between orbital and spin angular momentum of single photons. Optics Letters, **37** (2012), 172.

[70] D'Ambrosio, V., Nagali, E., Walborn, S., Aolita, L., Slussarenko, S., Marrucci, L., and Sciarrino, F. Complete experimental toolbox for alignment-free quantum communication. Nature Communications, **3** (2012), 961.

[71] D'Ambrosio, V., et al. Photonic polarization gears for ultra-sensitive angular measurements. Nature Communications, **4** (2013), 2432.

[72] Darwin, C. Proc. R. Soc. Lond. A, **36** (1932).

[73] de la Torre, G., Masanes, L., Short, A., and Müller, M. Deriving quantum theory from its local structure and reversibility. arXiv:1110.5482, (2011).

[74] Demkowicz-Dobrzanski, R., Kolodynski, J., and Guta, M. The elusive heisenberg limit in quantum-enhanced metrology. Nature Communications, **3** (2012), 1063.

[75] Djordjevic, I. Deep-space and near-earth optical communications by coded orbital angular momentum (oam) modulation. Optics Express, **19** (2011), 14277.

[76] Dorner, U., Demkowicz-Dobrzanski, R., Smith, B. J., Lundeen, J. S., Wasilewski, W., Banaszek, K., and Walmsley, I. A. Optimal quantum phase estimation. Physical Review Letters, **102** (2009), 040403.

[77] Durt, T., Englert, B.-G., Bengtsson, I., and Życzkowski, K. On mutually unbiased bases. International Journal of Quantum Information, **8** (2010), 535.

[78] Eberhard, P. Physical Review A, **47** (1993), 747.

[79] Einstein, A., Podolsky, B., and Rosen, N. Can quantum-mechanical description of physical reality be considered complete? Physical Review, **47** (1935), 777.

[80] Ekert, A. K. Quantum cryptography based on Bell's theorem. Physical Review Letters, **67** (1991), 661.

[81] Englert, B. and Aharonov, Y. How to ascertain the values of σ_x, σ_y and σ_z of a spin-1/2 particle. Physics Letters A, **284** (2001), 1.

[82] Escher, B., Matos Filho, R. L., and Davidovich, L. General framework for estimating the ultimate precision limit in noisy quantum-enhanced metrology. Nature Physics, **7** (2011), 406.

[83] Fickler, R., Lapkiewicz, R., Plick, W. N., Krenn, M., Schaeff, C., Ramelow, S., and Zeilinger, A. Quantum entanglement of high angular momenta. Science, **338** (2012), 640.

[84] Fine, A. I. Joint distributions, quantum correlations, and commuting observables. Journal of Mathematical Physics, **23** (1982), 1306.

[85] Fiorentino, M. and Wong, F. N. C. Deterministic controlled-not gate for single-photon two-qubit quantum logic. Physical Review Letters, **93** (2004), 070502.

[86] Fitzi, M., Gisin, N., and Maurer, U. Quantum Solution to the Byzantine Agreement Problem. Physical Review Letters, **87** (2001), 21.

[87] Franke-Arnold, S., Allen, L., and Padgett, M. Advances in optical angular momentum. Laser & Photonics Reviews, **2** (2008), 299.

[88] Fujiwara, M., Takeoka, M., Mizuno, J., and Sasaki, M. Exceeding the classical capacity limit in a quantum optical channel. Physical Review Letters, **90** (2003), 167906.

[89] Fukuda, D., et al. Titanium-based transition-edge photon number resolving detector with 98% detection efficiency with index-matched small-gap fiber coupling. Optics Express, **19** (2011), 870.

[90] Furhapter, S., Jesacher, A., Bernet, S., and Ritsch-Marte, M. Spiral phase contrast imaging in microscopy,. Opt. Exp., **13** (2005), 689.

[91] Gabor, D. A new microscopic principle. Nature, **161** (1948), 777.

[92] Gershenfeld, N. A. and Chuang, I. L. Bulk spin-resonance quantum computation. Science, **275** (1997), 350.

[93] Giovannetti, V., Lloyd, S., and Maccone, L. Advances in quantum metrology. Nature Photonics, **5** (2011).

[94] Giovannini, D., Nagali, E., Marrucci, L., and Sciarrino. Transport of orbital- angular-momentum entanglement through a turbulent atmosphere. Physical Review A, **83** (2011), 042338.

[95] Giovannini, D., Romero, J., Leach, J., Dudley, A., Forbes, A., and Padgett, M. Characterization of high-dimensional entangled systems via mutually unbiased measurements. Physical Review Letters, **110** (2013), 143601.

[96] Gisin, N. Bell's inequality holds for all non-product states. Physics Letters A, **154** (1991), 201.

[97] Gisin, N., Ribordy, G., Tittel, W., and Zbinden, H. Quantum cryptography. Reviews of Modern Physics, **74** (2002), 145.

[98] Giustina, M., et al. Bell violation using entangled photons without the fair-sampling assumption. Nature, **497** (2013), 227.

[99] Gonzales, N., Molina-Terriza, G., and Torres, J. P. How a dove prism transforms the orbital angular momentum of a light beam. Optics Express, **14** (2006), 9093.

[100] Gottesman, D., Lo, H. K., Lütkenhaus, N., and Preskill, J. Security of quantum key distribution with imperfect devices. Quantum Information and Computation, **5** (2004), 325.

[101] Goye, D. Mutually unbiased triplets from non-affine families of complex Hadamard matrices in dimension 6. Journal of Physics A, **46** (2013), 105301.

[102] Grier, D. G. A revolution in optical manipulation. Nature, **424** (2003), 810.

[103] Gröblacher, S., Jennewein, T., Vaziri, A., Weihs, G., and Zeilinger, A. Experimental quantum cryptography with qutrits. New Journal of Physics, **8** (2006), 75.

[104] Hardy, L. Quantum theory from five reasonable axioms. quant-ph/0101012, (2001).

[105] Heckenberg, N., McDuff, R., Smith, C., and White, A. Generation of optical phase singularities by computer-generated holograms. Optics Letters, **17** (1992), 221.

[106] Higgins, B. L., Berry, D. W., Bartlett, S. D., Wiseman, H. M., and Pryde, G. J. Entanglement-free heisenberg-limited phase estimation. Nature, **450** (2007), 393.

[107] Holevo, A. S. Lect. Notes Math., **1055** (1984), 153.

[108] Horodecki, K., Horodecki, M., Horodecki, P., Horodecki, R., Pawlowski, M., and Bourennane, M. Contextuality offers device-independent security. arXiv:1006.0468, (2010).

[109] Horodecki, M., Horodecki, P., and Horodecki, R. Separability of mixed states: necessary and sufficient conditions. Physics Letters A, **223** (1996), 1.

[110] Horodecki, R., Horodecki, P., Horodecki, M., and Horodecki, K. Quantum entanglement. Reviews of Modern Physics, **81** (2009), 865.

[111] Jha, A. K., Agarwal, G. S., and Boyd, R. W. Supersensitive measurement of angular displacements using entangled photons. Physical Review A, **83** (2011), 053829.

[112] Jones, J. A., Karlen, S. D., Fitzsimons, J., Ardavan, A., Benjamin, S. C., Briggs, G. A. D., and Morton, J. J. L. Magnetic Field Sensing Beyond the Standard Quantum Limit Using 10-Spin NOON States. Science, **324** (2009), 1166.

[113] Karimi, E., Zito, G., Piccirillo, B., Marrucci, L., and Santamato, E. Hypergeometric-gaussian modes. Optics Letters, **32** (2007), 3053.

[114] Kaszlikowski, D., Gnaciński, P., Żukowski, M., Miklaszewski, W., and Zeilinger, A. Violations of local realism by two entangled *n*-dimensional systems are stronger than for two qubits. Physical Review Letters, **85** (2000), 4418.

[115] Kernaghan, M. and Peres, A. Kochen-Specker theorem for eight-dimensional space. Physics Letters A, **198** (1995), 1.

[116] Kirchmair, G., Zähringer, F., Gerritsma, R., Kleinmann, M., Gühne, O., Cabello, A., Blatt, R., and Roos, C. Experimentally testable state-independent quantum contextuality. Nature, **460** (2009), 494.

[117] Kirchmair, G., Zähringer, F., Gerritsma, R., Kleinmann, M., Gühne, O., Cabello, A., Blatt, R., and Roos, C. F. State-independent experimental test of quantum contextuality. Nature, **460** (2009), 494.

[118] Klappenecker, A. and Rotteler, M. Fully nonlocal quantum correlations. Lecture Notes in Computer Science, **2984** (2003), 137.

[119] Klappenecker, A. and Rötteler, M. Constructions of mutually unbiased bases. Finite Fields and Applications, **2948** (2004), 262.

[120] Klyachko, A., Can, M. A., Binicioglu, S., and Shumovsky, A. S. Simple test for hidden variables in spin-1 systems. Physical Review Letters, **101** (2008), 020403.

[121] Knysh, S., Smelyanskiy, V. N., and Durkin, G. A. Scaling laws for precision in quantum interferometry and bifurcation landscape of optimal state. Physical Review A, **83** (2011), 021804 (R).

[122] Kochen, S. and Specker, E. P. The problem of hidden variables in quantum mechanics. Journal of Applied Mathematics and Mechanics, **17** (1967), 59.

[123] Kolenderski, P., Sinha, U., Youning, L., Zhao, T., Volpini, M., Cabello, A., R., L., and Jennewein, T. Playing the Aharon-Vaidman quantum game with a Young type photonic qutrit. arXiv:1107.5828.

[124] Kołodyński, J. and Demkowicz-Dobrzański, R. Phase estimation without a priori phase knowledge in the presence of loss. Physical Review A, **82** (2010), 053804.

[125] Kwiat, P. G., Mattle, K., Weinfurter, H., Zeilinger, A., Sergienko, A. V., and Shih, Y. New high-intensity source of polarization-entangled photon pairs. Physical Review Letters, **75** (1995), 4337.

[126] Lanyon, B. P., et al. Simplifying quantum logic using higher-dimensional hilbert spaces. Nature Physics, (2009), 134.

[127] Łapkiewicz, R., Li, P., Schaeff, C., Langford, N., Ramelow, S., Wiesniak, M., and Zeilinger, A. Experiments towards falsification of noncontextual hidden variable theories. Nature, **474** (2011), 490.

[128] Lavery, M., Robertson, D., Berkhout, G., Love, G., Padgett, M., and Courtial, J. Refractive elements for the measurement of the orbital angular momentum of a single photon. Optics Express, **20** (2012), 2110.

[129] Leach, J., Dennis, M. R., Courtial, J., and Padgett, M. Vortex knots in light. New Journal of Physics, **7** (2005), 55.

[130] Leach, J., Jack, B., Romero, J., Ritsch-Marte, M., Boyd, R. W., Jha, A. K., Barnett, S. M., Franke-Arnold, S., and Padgett, M. J. Violation of a bell inequality in two-dimensional orbital angular momentum state-spaces. Optics Express, **338** (2012), 640.

[131] Leach, J., Padgett, M. J., Barnett, S. M., Franke-Arnold, S., and Courtial, J. Measuring the orbital angular momentum of a single photon. Physical Review Letters, **88** (2002), 257901.

[132] Lee, H., Kolk, P., and Dowling, J. P. A quantum rosetta stone for interferometry. Journal of Modern Optics, **49** (2002), 2325.

[133] Leibfried, D., et al. Creation of a six-atom 'schrödinger cat' state. Physical Review Letters, **88** (2002), 257901.

[134] Li, S., Yang, C., Zhang, E., and Jin, G. Compact optical roll-angle sensor with large measurement range and high sensitivity. Optics Letters, **30** (2005), 242.

[135] Lidar, D., Chuang, I., and Whaley, K. Decoherence-free subspaces for quantum computation. Physical Review Letters, **81** (1998), 2594.

[136] Lima, G. and et al. Experimental quantum tomography of photonic qudits via mutually unbiased basis. Optics Express, **19** (2011), 3452.

[137] Lita, A. E., Calkins, B., Pellouchoud, L. A., Miller, A. J., and Nam, S. Superconducting transition-edge sensors optimized for high-efficiency photon-number resolving detectors. Proc. SPIE Int. Soc. Opt. Eng., **7681** (2010), 76810D.

[138] Liu, Z., Lin, D., Jiang, H., and Yin, C. Polarization pattern of vector vortex beams generated by q-plates with different topological charges. Sensor Actuat. A, **104** (2003), 127.

[139] Mair, A., Vaziri, A., Weihs, G., and Zeilinger, A. Entanglement of the orbital angular momentum states of photons. Nature, **412** (2001), 313.

[140] Marrucci, L., Manzo, C., and Paparo, D. Optical spin-to-orbital angular momentum conversion in inhomogeneous anisotropic media. Physical Review Letters, **96** (2006), 163905.

[141] MartŠnez-Herrero, R. and MejŠas, P. Angular momentum decomposition of non-paraxial light beams. Optics Express, **18** (2010), 7965.

[142] Masanes, L. and Müller, M. P. A derivation of quantum theory from physical requirements. New Journal of Physics, **13** (2011), 063001.

[143] McNulty, D. and Weigert, S. On the impossibility to extend triples of mutually unbiased product bases in dimension six. International Journal of Quantum Information, **10** (2012), 1250056.

[144] McNulty, D. and Weigert, S. The limited role of mutually unbiased product bases in dimension 6. Journal of Physics A, **45** (2012), 102001.

[145] Michler, M., Weinfurter, H., and Zukowski, M. Experiments towards falsification of noncontextual hidden variable theories. Physical Review Letters, **84** (2000), 5457.

[146] Mitchell, M., Lundeen, J. S., and Steinberg, A. M. Super-resolving phase measurements with a multiphoton entangled state. Nature, **429** (2004).

[147] Molina-Terriza, G., Torres, J., and Torner, L. Twisted photons. Nature Physics, **3** (2007), 305.

[148] Moussa, O., Ryan, C. A., Cory, D. G., and Laflamme, R. Testing contextuality on quantum ensembles with one clean qubit. Physical Review Letters, **104** (2010), 160501.

[149] Nagali, E., D'Ambrosio, V., Sciarrino, F., and Cabello, A. Experimental observation of impossible-to-beat quantum advantage on a hybrid photonic system. Physical Review Letters, **108** (2012), 090501.

[150] Nagali, E., Sansoni, L., Marrucci, L., Santamato, E., and Sciarrino, F. Experimental generation and characterization of single-photon hybrid ququarts based on polarization and orbital angular momentum encoding. Physical Review A, **81** (2010), 052317.

[151] Nagali, E., Sciarrino, F., De Martini, F., Marrucci, L., Piccirillo, B., Karimi, E., and Santamato, E. Quantum information transfer from spin to orbital angular momentum of photons. Physical Review Letters, **103** (2009), 013601.

[152] Nagali, E., Sciarrino, F., Martini, F. D., Piccirillo, B., Karimi, E., Marrucci, L., and Santamato, E. Polarization control of single photon quantum orbital angular momentum states. Optics Express, **17** (2009), 18745.

[153] Nagata, T., Okamoto, R., O'Brien, J. L., Sasaki, K., and Takeuchi, S. Beating the standard quantum limit with four-entangled photons. Science, **316** (2007), 726.

[154] Neves, L., Lima, G., Aguirre Gómez, J. G., Monken, C. H., Saavedra, C., and Pádua, S. Generation of entangled states of qudits using twin photons. Phys. Rev. Lett., **94** (2005), 100501.

[155] Nielsen, M. A. and Chuang, I. L. Quantum Information and Quantum Computation. Cambridge University Press (2000).

[156] Ollivier, H. and Zurek, W. H. Quantum discord: a measure of the quantumness of correlations. Physical Review Letters, **88** (2001), 017901.

[157] Oppenheim, J. and Wehner, S. The Uncertainty Principle Determines the Nonlocality of Quantum Mechanics. Science, **330** (2010), 1072.

[158] Ornigotti, M. and Aiello, A. Incompleteness of spin and orbital angular momentum separation for light beams. arXiv:1304.5018, (2013).

[159] O'Sullivan-Hale, M. N., Ali Khan, I., Boyd, R. W., and Howell, J. C. Pixel entanglement: Experimental realization of optically entangled $d = 3$ and $d = 6$ qudits. Phys. Rev. Lett., **94** (2005), 220501.

[160] Padget, M. J. and Bowman, R. Tweezers with a twist. Nature Photonics, **5** (2011), 343.

[161] Palma, G., Suominen, K., and Ekert, A. Quantum computers and dissipation. Proc. R. Soc. London, Ser. A, **452** (1996), 567.

[162] Paterson, C. Atmospheric turbulence and orbital angular momentum of single photons for optical communication. Physical Review Letters, **94** (2005), 153901.

[163] Pavičić, M., Merlet, J.-P., McKay, B. D., and Megill, N. D. Kochen-Specker vectors. Journal of Physics A, **38** (2005), 1577.

[164] Pawłowski, M., Paterek, T., Kaszlikowski, D., Scarani, V., Winter, A., and Żukowski, M. Information causality as a physical principle. Nature, **461** (2009), 1101.

[165] Peres, A. Quantum Theory: Concepts and Methods. Kluwer (1995).

[166] Peres, A. What's wrong with these observables? Foundations of Physics, **33** (2003), 1543.

[167] Peres, A. and Scudo, P. Entangled quantum states as direction indicators. Physical Review A, **86** (2001), 4160.

[168] Peruzzo, A., et al. Quantum walks of correlated photons. Science, **329** (2010), 1500.

[169] Piccirillo, B., D'Ambrosio, V., Slussarenko, S., Marrucci, L., and Santamato, E. Photon spin-to-orbital angular momentum conversion via an electrically tunable q-plate. Applied Physics Letters, **97** (2010), 241104.

[170] Pironio, S., et al. Experimental violation of a Bell's inequality with efficient detection. Nature, **464** (2010), 1021.

[171] Planat, M. and Baboin, A. Qudits of composite dimension, mutually unbiased bases and projective ring geometry. Journal of Physics A: Mathematical and Theoretical, **40** (2007), F1005.

[172] Planat, M., Rosu, H., and Perrine, S. A survey of finite algebraic geometrical structures underlying mutually unbiased quantum measurements. Foundations of Physics, **36** (2006), 1662.

[173] Politi, A., Cryan, M. J., Rarity, J. G., Yu, S., and O'Brien, J. L. Silica-on-silicon waveguide quantum circuits. Science, **320** (2008), 646.

[174] Pors, B., Monken, C. H., Eliel, E. R., and Woerdman, J. P. Transport of orbital-angular-momentum entanglement through a turbulent atmosphere. Optics Express, **19** (2011), 6671.

[175] Poynting, J. H. The wave motion of a revolving shaft, and a suggestion as to the angular momentum in a beam of circularly polarized light. Proc. R. Soc. London, **82** (1909), 560.

[176] Rarity, J. G., Tapster, P. R., Gorman, P. M., and Knight, P. Ground to satellite secure key exchange using quantum cryptography. New Journal of Physics, **4** (2002), 82.

[177] Raynal, P., Lu, X., and Englert, B. Mutually unbiased bases in six dimensions: The four most distant bases. Physical Review A, **83** (2011), 062303.

[178] Reich, E. Photons test quantum paradox. Nature, **496** (2013), 282.

[179] Roos, C. F., Chwalla, M., Kim, K., Riebe, M., and Blatt, R. 'Designer atoms' for quantum metrology. Nature, **443** (2006), 316.

[180] Rosenfeld, V. and et al. Towards a loophole-free test of bell's inequality with entangled pairs of neutral atoms. Advanced Science Letters, **2** (2009), 469.

[181] Rowe, M. A., Kielpinski, D., Meyer, V., Sackett, C. A., Itano, W. M., Monroe, C., and Wineland, D. J. Experimental violation of a Bell's inequality with efficient detection. Nature, **409** (2001), 791.

[182] Sadiq, M., Badziag, P., Bourennane, M., and Cabello, A. Bell inequalities for the simplest exclusivity graph. Physical Review A, **87** (2013), 012128.

[183] Saleh, B. E. A. and Teich, M. C. Fundamentals of Photonics. Wiley Interscience (1991).

[184] Sansoni, L., Sciarrino, F., Vallone, G., Mataloni, P., Crespi, A., Ramponi, R., and Osellame, R. Polarization entangled state measurement on a chip. Physical Review Letters, **105** (2010), 200503.

[185] Sansoni, L., Sciarrino, F., Vallone, G., Mataloni, P., Crespi, A., Ramponi, R., and Osellame, R. Two-particle bosonic-fermionic quantum walk via integrated photonics. Physical Review Letters, **108** (2012), 010502.

[186] Scarani, V., Bechmann-Pasquinucci, H., Cerf, J. F., Dusek, M., Lutkenhaus, N., and Peev, M. The security of practical quantum key distribution. Reviews of Modern Physics, **81** (2009), 1301.

[187] Shor, P. and Preskill, J. Simple proof of security of the bb84 quantum key distribution protocol. Physical Review Letters, **85** (2000), 441.

[188] Slussarenko, S., D'Ambrosio, V., Piccirillo, B., Marrucci, L., and Santamato, E. The polarizing sagnac interferometer: a tool for light orbital angular momentum sorting and spin-orbit photon processing. Optics Express, **18** (2010), 27205.

[189] Slussarenko, S., Murauski, A., Du, T., Chigrinov, V., Marrucci, L., and Santamato, E. Tunable liquid crystal q-plates with arbitrary topological charge. Optics Express, **19** (2011), 4085.

[190] Smith, D. H., et al. Conclusive quantum steering with superconducting transition-edge sensors. Nature Commun., **3** (2012), 625.

[191] Spagnolo, N., Vitelli, C., Lucivero, G., Giovannetti, V., Maccone, L., and Sciarrino, F. Phase estimation via quantum interferometry for noisy detectors. Physical Review Letters, **108** (2012), 233602.

[192] Specht, H. P., Nolleke, C., Reiserer, A., Uphoff, M., Figueroa, E., Ritter, S., and Rempe, G. A single-atom quantum memory. Nature, **473** (2011), 190.

[193] Specker, E. P. Die Logik nicht gleichzeitig entscheidbarer Aussagen. Dialectica, **14** (1960), 239.

[194] Spengler, C., Huber, M., Brierley, S., and Adaktylos, T. Entanglement detection via mutually unbiased bases. Physical Review A, **86** (2012), 022311.

[195] Svozil, K. Staging quantum cryptography with chocolate balls. American Journal of Physics, **74** (2006), 800.

[196] Svozil, K. Bertlmann's chocolate balls and quantum type cryptography. in Physics and Computation, (2009), pag 235 .

[197] Tamburini, F., Thide, B., Molina-Terriza, G., and Anzolin, G. Twisting of light around rotating black holes. Nat. Phys., **7** (2011), 195.

[198] Tittel, W., Brendel, J., Zbinden, H., and Gisin, N. Violation of Bell inequalities by photons more than 10 km apart. Physical Review Letters, **81** (1998), 3563.

[199] Torner, L., Torres, J., and Carrasco, S. Digital spiral imaging. Optics Express, **13** (2005), 873.

[200] Ursin, R. e. a. Entanglement-based quantum communication over 144 km. Nature Physics, **3** (2007), 481.

[201] Vaidman, L., Aharonov, Y., and Albert, D. How to ascertain the values of σ_x, σ_y and σ_z of a spin-1/2 particle. Physical Review Letters, **58** (1987), 1385.

[202] Vértesi, T., Pironio, S., and Brunner, N. Closing the detection loophole in bell experiments using qudits. Physical Review Letters, **104** (2010), 060401.

[203] Villoresi, P. and et al. Experimental verification of the feasibility of a quantum channel between space and earth. New Journal of Physics, **10** (2008), 033038.

[204] Walter, P., Pan, J. W., Aspelmeyer, M., Ursin, R., Gasparoni, S., and Zeilinger, A. De broglie wavelength of a non-local four-photon state. Nature, **429** (2004), 158.

[205] Walton, Z., Abouraddy, A., Sergienko, A., Saleh, B., and Teich, M. Decoherence-free subspaces in quantum key distribution. Physical Review Letters, **91(8)** (2003), 87901.

[206] Wei, H., Xue, X., Leach, J., Padgett, M. J., Barnett, S. M., Franke-Arnold, S., Yao, E., and Courtial, J. Simplified measurement of the orbital angular momentum of single photons. Optics Communications, (2003), 117.

[207] Weihs, G., Jennewein, T., Simon, C., Weinfurter, H., and A., Z. Violation of Bell's inequality under strict Einstein locality conditions. Physical Review Letters, **81** (1998), 5039.

[208] Werner, R. F. Quantum states with einstein-podolsky-rosen correlations admitting a hidden-variable model. Physical Review A, **40** (1989), 4277.

[209] Wittmann, B., Ramelow, S., Steinlechner, F., Langford, N. K., Brunner, N., Wiseman, H., Ursin, R., and Zeilinger, A. Loophole-free einstein-podolsky-rosen experiment via quantum steering. New Journal of Physics, **14** (2012), 053030.

[210] Wootters, W. and Zurek, W. A single quantum cannot be cloned. (1982).

[211] Wootters, W. K. and Fields, B. Albert Einstein: Philosopher-Scientist. Annals of Physics, **191** (1989), 363.

[212] Yan, B. Quantum correlations are tightly bounded by the exclusivity principle. Physical Review Letters, **110** (2013), 260406.

[213] Yao, A. M. and Padgett, M. Orbital angular momentum: origins, behavior and applications. Advances in optics and photonics, **3** (2011), 161.

[214] Zanardi, P. and Rasetti, M. Noisless quantum codes. Physical Review Letters, **79** (1997), 3306.

[215] Zhang, J., Bao, X.-H., Chen, T.-Y., Yang, T., Cabello, A., and Pan, J.-W. Experimental demonstration of the quantum "Guess my Number" protocol using multiphoton entanglement. Physical Review A, **75** (2007), 022302.

[216] Zhao, S. M., Leach, J., Gong, L. Y., Ding, J., and Zheng, B. Y. Aberration corrections for free-space optical communications in atmosphere turbulence using orbital angular momentum states. Optics Express, **20** (2012), 452.